The Dissertation Committee for Nicole Elise Pollok Certifies that this is the approved version of the following Dissertation:

The Development of a Metalloimmunoassay for the Detection of NT-proBNP

Committee:

_____
Richard M. Crooks, Supervisor

_____
Ian Richards

_____
Livia Schiavinato Eberlin

_____
Eric V. Anslyn

_____
David Hoffman

The Development of a Metalloimmunoassay for the Detection of NT-proBNP

by

Nicole Elise Pollok

Dissertation

Presented to the Faculty of the Graduate School of

The University of Texas at Austin

in Partial Fulfillment

of the Requirements

for the Degree of

Doctor of Philosophy

The University of Texas at Austin

May 2021

Dedication

To my parents, sisters, and grandparents,

Michael and Natalie,

Brittany and Kristen, and

Lillian and Archie Pollok

Acknowledgements

I would like to thank my research advisor, Prof. Richard M. Crooks, who made this journey possible and pleasant. His patience, guidance, and support in all these years led me to grow as a young scientist and as a young professional.

I would like to thank my committee members at The University of Texas at Austin: Prof. Livia Eberlin, Prof. Eric Anslyn, and Prof. David Hoffman. Additionally, I would like to thank Dr. Ian Richards who has been an external consultant during my time here at UT Austin. I thank all these individuals for helping me finish my graduate study.

My gratitude goes to my fellow Crooks group members for their assistance in and out of the laboratory, especially my collaborators: Dr. Charlie Rabin and Dr. Jamie Trindell. Special thanks go to Angie Missildine and Betsy Hamblen, who have been incredibly helpful and let me focus on my research.

Finally, I want to thank my family and specifically a fellow chemistry graduate student, my roommate and sister, Brittany Pollok for all the laughs on and off campus.

You’re next, Bip.

Abstract

The Development of a Metalloimmunoassay for the Detection of NT-proBNP

Nicole Elise Pollok, Ph. D.

The University of Texas at Austin, 2021

Supervisor: Richard M. Crooks

The purpose of this doctoral research is to develop a biosensor for the monitoring of heart failure (HF) in humans. Currently, there is no quantitative patient-facilitated method to monitor HF, and the physical symptoms that result are a poor representation of the acute state of the disease. The biomarker of interest is N-terminal prohormone brain natriuretic peptide (NT-proBNP) which is secreted from the cardiac muscle tissue when the heart is experiencing decompensation. The concentration of NT-proBNP has a direct correlation to the severity of HF, and it is used as the antigen in a metalloimmunoassay, where two monoclonal antibodies are used to sandwich NT-proBNP. One is conjugated to a magnetic microbead via a streptavidin-biotin interaction, and the other is conjugated to a 20 nm-

diameter silver nanoparticle (AgNP) using a heterobifunctional cross-linker. The fully formed metalloimmunoassay is placed on a carbon screen-printed and Au electrodeposited sensing electrode to detect AgNP labels electrochemically. Ag charge collected from the assay is representative of the concentration of NT-proBNP in the sample. A phenomenon known as galvanic exchange (GE) is utilized in the detection of Ag. GE is a process that occurs when a zerovalent metal is immersed in a solution containing the oxidized form of a more noble metal. In this specific case, the exchange occurs between AgNP in the metalloimmunoassay and Au^{3+} generated on the sensing electrode. GE occurs because the standard reduction potential of Ag^{+} is slightly lower than Au^{3+}. Significant findings of this project reveal that GE between AgNP and Au^{3+} is a process that results in only a partial exchange of AgNP with the Au^{3+} under physiologic conditions. It has also been found that, implementing two subsequent Au^{3+} electrogeneration steps improve the Ag collection efficiency and the reproducibility. Additionally, using heterobifunctional cross-linkers to covalently attach antibodies to AgNP and silver nanocubes (AgNCs) results in a lower limit of detection. These findings have led to the detection of NT-proBNP in buffer within clinically relevant ranges of 0.06-3.49 nM.

Table of Contents

List of Tables

List of Figures

List of Illustrations

Chapter 1: Introduction

1.1 Electrochemical biosensors

A biosensor is a tool that takes a biological sample, pinpoints a specific biomarker via a capture assay or a labeled probe, and provides the user with either qualitative or quantitative analytical information about the concentration of the biomarker of interest.[1] Some biosensors fall into a category known as point-of-care (POC) diagnostic devices in which rapid results are given to the user at the point of care. These devices can be constructed from glass,[2,3] plastic,[4,5] or paper[4,6,7] and are often fabricated in the form of microfluidic or lateral-flow constructs.[8,9] There are also hybrid designs which combine several different materials.[10] Typically, the signal or response that is generated from the sensor is either in the form of a change in spectroscopic absorption,[11] fluorescence emission,[12,13] or electrochemical current.[14–17] The readout from the device is then usually correlated to a calibration curve so that the specific response can be measured. From there, the user, whether that is the patient, physician, or clinician, makes a decision about treatment based on the results provided.

The unique, nearly equipment-free design of POC and point-of-need devices enables them to be used in a variety of settings

such as at home,[18,19] in clinics,[20–22] and in hospitals.[23,24] The matrix in which the analyte is naturally present and stable in is a key element to consider when designing POC devices. Biomarkers and metabolites are found in an assortment of different matrixes such as urine,[25] saliva,[26–28] sweat,[29,30] and whole blood.[31,32] In some cases, these matrixes can be beneficial[33,34] to detection, while in others can be detrimental.[35,36]

An example of a POC electrochemical biosensor which became a pivotal tool in health care and in the disease management of diabetes was the blood glucose meter. In 1987, Matthews et al. constructed a pen-shaped sensor which used a paper test strip to electrochemically detect glucose levels in whole blood.[37,38] This device eventually evolved into the more familiar and commercially available personal glucose meter, which was developed by Csöregi and coworkers.[39] Another example of a momentous POC biosensor is the paper-based lateral flow device which detected the pregnancy hormone, human chorionic gonadotropin, in an enzymatic immunoassay.[37] This laid the groundwork for the modern at-home pregnancy test.

To construct a successful and useful POC device, several characteristics must be kept in mind. Specifically, these characteristics include: affordability, sensitivity,

specificity, user-friendliness, and the tools also need to be rapid, robust, equipment free, and deliverable to the end-user according to the World Health Organization.[40] To achieve all of these features in one POC test, a great deal of ingenuity needs to go into bioassay design.

1.2 Designs of bioassays

Designing a bioassay ultimately requires four parts: (1) recognition elements such as antibodies (Abs), nucleic acids, or aptamers to capture the biomarker or analyte of interest; (2) a signal amplification mechanism such as enzymes or nanoparticles (NPs) so that detection can be performed within clinically relevant concentration ranges; (3) a bioconjugation technique to immobilize the recognition element to the signal amplifier; and (4) a detection mechanism. All these pieces combine to create the everyday biosensors that are familiar to us today. In Illustration 1.1, the clinically relevant concentration ranges for different biomolecules, specifically small molecules, nucleic acids, and proteins are shown. This illustration illuminates the vast and wide concentration ranges that biosensors need to target to be clinically useful.

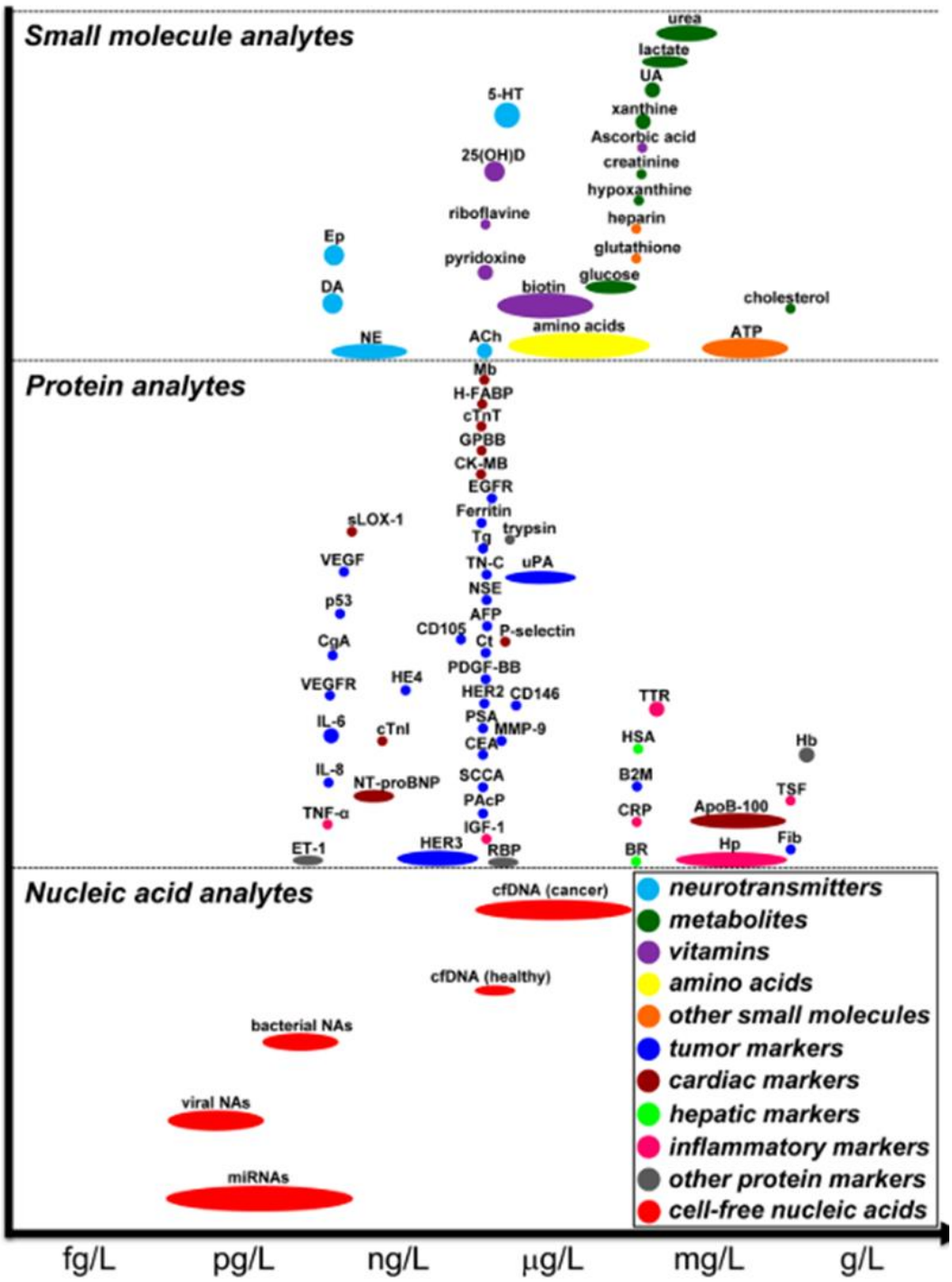

Illustration 1.1 Diagram showing the reference concentration ranges for the detection of different clinically relevant small molecules, nucleic acids, and proteins sorted by mass.[41] Image sourced from Reference 41.

1.2.1 Recognition elements

Depending on the target biomolecule, several different recognition elements can be used in the bioassay. In this context, a recognition element refers to a material or process that can selectively extract the target molecule from its matrix. These elements can include Abs, nucleic acids, or aptamers.

Monoclonal Abs are commonly the tool of choice when Abs are used as recognition elements. The primary characteristic that sets monoclonal Abs apart from polyclonal Abs is the presence of only one epitope on the Abs antigen-binding region. This feature plays a key role in the sensitivity and selectivity of the bioassay to the antigen. Polyclonal Abs have more than one epitope on the antigen-binding regions of the Ab, and depending on the purpose of the assay, this can be detrimental to the selectivity of the sensor because biomolecules other than the biomarker of interest can potentially bind to those regions. Typically, Abs are used in the form of a sandwich assay in which a capture Ab is immobilized on a surface, and a labeled reporter, or detection Ab binds to the analyte and provides a signal.[42]

Nucleic acid recognition elements involve a noncovalent interaction between bases of complimentary nucleic acid strands and is manifested by hybridization between an immobilized capture probe and a complementary sequence.[43,44] This bioassay can be constructed as either a stem-loop or linear probe depending on the structure and length of the nucleic acid sequence.[45] This mechanism can generate signal-ON[46] and signal-OFF[47] electrochemical sensors when the target biomolecule is captured.

Aptamers are nucleic acid ligands that are another commonly used recognition element used in biosensors. These work similarly to nucleic acid strands, except for that in contrast to the base paring exhibited by nucleic acid, aptamers can fold to form highly specific three-dimensional structures due to their self-annealing properties.[48,49] This results in a selectivity and binding affinity similar to Abs, and these features can be tailored during the aptamer selection process. Aptamers also have the advantage of being highly robust in that they can survive numerous rounds of denaturation and renaturation on the sensor surface during the detection process.[50–52]

1.2.2 Signal amplification

Signal amplification is another key part of a successful bioassay. The idea behind this feature is that for every target

biomolecule that is captured, an ideal sensor should generate more than just one unit of signal. This aspect of bioassay construction is usually accomplished by using fluorescent probes,[53] NPs,[54] or enzymatic labels;[55] for example, in enzyme-linked immunosorbent assays (ELISA). Enzymes such as horseradish peroxidase and alkaline phosphate are traditionally used in immunoassays and result in an obvious color change when the target biomolecule is captured and is exposed to oxidizing reagents. The use of metallic or semiconduction NPs for signal amplification is becoming increasingly more common. This is due to their generally higher stability, lower cost, and faster read-out times.[41,56] Note that an immunoassay that uses an NP as a recognition element is referred to as a metalloimmunoassay.

In Illustration 1.2, a general detection process involving noble metal NPs is shown. Due to the different electrochemical, optical, and piezoelectric properties of NPs, a variety of transduction methods have been reported. The Crooks group in particular has been pioneering the use of NPs as detection labels over the last 10 years. Specifically, the use of silver NPs (AgNPs) for detection of an assortment of biomolecules.[57–59] The idea here is that for every one target biomolecule that is captured and forms a sandwich assay, there are hundreds of thousands of metal ions that can be detected electrochemically

within that one formed immuno-sandwich. For example, there are ~250,000 Ag atoms in a 20 nm-diameter AgNP (Illustration 1.3). This means that for one sandwich assay, a signal amplification of up to 250,000-fold is possible.

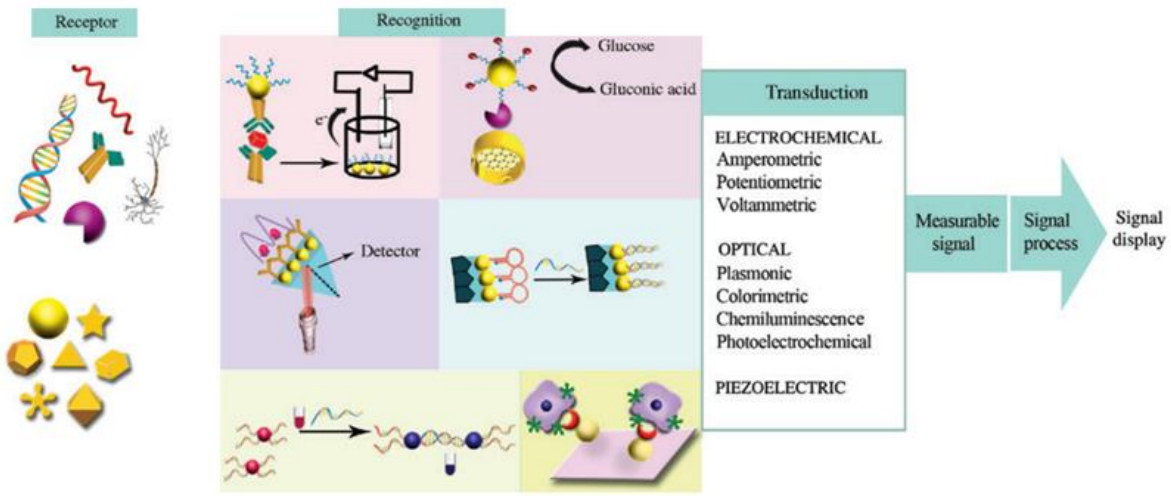

Illustration 1.2. Scheme showing the role of noble metal NPs in various types of biosensors.[60] Image sourced from Reference 60.

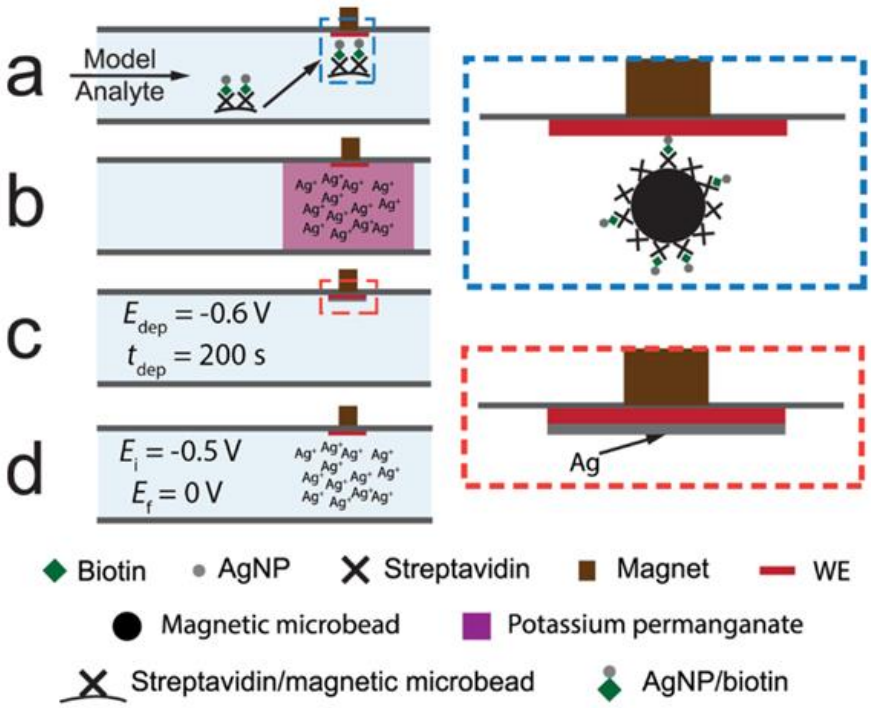

Illustration 1.3 Schematic of a detection method involving the use of a model composite containing streptavidin-coated magnetic microbead (MμBs) to immobilize AgNP-biotin conjugates to the bead surface. (a) Pre-concentration of formed model conjugate at the working electrode surface. (b) Chemical oxidate of the AgNP with $KMnO_4$. (c) Electrodeposition of the Ag^+. (d) Anodic stripping of the electrodeposited Ag^0 from the electrode surface for quantification. Image sourced from Reference 61.[61]

1.2.2 Bioconjugation techniques

After the appropriate recognition elements have been selected for the bioassay, those elements usually require some type of attachment to a signal amplification mechanism. In the context of monoclonal Abs and metal NPs, there are two common methods: chemisorption (physisorption) and covalent linkage. Physisorption relies primarily on interactions between the NP surface and amine or thiol residues present on the Abs. This

approach is widely used due to it being fast and easy, however a main limitation to this approach is the fact that Abs are not well-oriented on the NP surface. This results in the antigen-binding regions of the Abs having limited access to target molecules in a sample which reduces the activity of the Abs.

Covalent linkage of Abs to NP can be done in a controlled manner depending on the regions of the Ab that are targeted. There are two main regions of an Ab, the antigen-binding region and the fragment crystallizable (Fc) region. Ideally, conjugation techniques should avoid the antigen-binding region as much as possible to ensure that it is undamaged during modifications. Some examples of covalent-linking techniques include 1-ethyl-3-(3-dimethylaminopropyl) carbodiimide (EDC) and N-hydroxysuccinimide (NHS) mediated cross-linker conjugation.[62] These methods, however, also target the primary amines on the Ab which can be located in the antigen-binding region.

1.3 Electrochemical detection

When the bioassay is finally fully formed, the next step is detection. Electrochemical detection techniques can be classified into four main types including voltammetric/amperometric, impedimetric, conductometric, and potentiometric.[63,64] Voltammetric and amperometric biosensors apply a potential to a working electrode versus a reference

electrode and measure the current. The current arises from electrolysis by means of an electrochemical oxidation or reduction at the working electrode and is limited by the mass transport rate of the reactant molecules from the bulk solution to the electrode interface. Amperometric biosensors offer additional selectivity because their oxidation or reduction potential used in analysis is typically characteristic of the analyte species.[63]

Electrochemical impedance spectroscopy is a technique that uses an AC source to perturbate a system and measure the response. The frequency is changed over a wide range to obtain an impedance spectrum. The in-phase and out-of-phase current responses are then measured to determine the resistive and capacitive components of the circuit.[41,65] In the context of biosensors, a rate limiting component at high frequency is the migration rate of the redox species to the electrode surface. Due to this, analyte can block the electrode and this generates a frequency-dependent phase lag between the AC voltage and the current.[63]

Conductometric biosensors measure changes in the electrical conductivity of a sample solution as the composition of the solution changes during a chemical reaction. These biosensors often include enzymes whose charged products cause changes in

the ionic strength of the sample solution.[64] Enzymes are also typically involved in potentiometric biosensors in which an ion-selective membrane reacts with the charged ion of interest. Enzymes can catalyze the reaction that forms the ion, which can be detected by the underlying electrode. The selection of all of these techniques, however, can be different for each biosensor detection system.

1.4 Research summary and accomplishments

This dissertation focuses on a combination of the core concepts discussed in Section 1.2 and 1.3. These concepts were involved in the design of an electrochemical biosensor for the heart failure biomarker, N-terminal prohormone brain natriuretic peptide (NT-proBNP). In particular, the formation of metalloimmunoassay which includes the use of monoclonal Abs conjugated to AgNPs and MμBs, followed by electrochemical detection via galvanic exchange/anodic stripping voltammetry (GE/ASV).

Specifically, Chapter 2 presents an in-depth investigation of the GE/ASV detection method using a model bioassay. The model assay is prepared with 110 nm AgNPs conjugated to a MμB surface via a streptavidin-biotin interaction. The morphology of the AgNPs are observed by scanning electron microscopy (SEM) after each electrochemical step. As a result, we discovered that after

two GE cycles, a Au shell was formed on the surface of the AgNPs, which essentially prevent further GE in the system.

Chapter 3 discusses the use of a heterobifunctional cross-linker to properly orient monoclonal Abs on the surface of AgNPs in a controlled manner. The goal of this work is to preserve the activity of the Abs during their immobilization onto the AgNP surface. This involved the synthesis of two slightly different cross-linkers, each of which included a thiolated-end for the covalent linkage to the AgNP surface, and a hydrazide-end which attached to the Fc region of the Ab. This resulted in the conjugate of ~5 active Abs per AgNP, and these conjugates were stable for at least 2 weeks.

Chapter 4 integrates the use of the heterobifunctional cross-linker (HBCL) into the metalloimmunoassay for NT-proBNP. This work compared the performance of the assay when a AgNP-Ab conjugate was formed via physisorption instead of the HBCL. A 27-fold increase in Ag signal was found when the HBCL was used, and we determined that the NT-proBNP assay could be formed in undiluted serum with no detectable interferences from the serum components. The linear dynamic range for this bioassay was 0.58-2.33 nM, which is only about 5-fold higher than the risk stratification concentration used by physicians (~0.116 nM).

Chapter 5 investigates the effects of serum on assay formation, washing steps, and electrochemical detection methods. Specifically, the GE/ASV technique was targeted and, both a model and antigen-specific bioassay were used. This work revealed that serum has no detectable effect on the formation of these assays, however when no washing is performed after assay formation even 0.50% serum remaining in the sample renders the detection inaccurate. Additionally, chelation of Au^{3+} and surface absorption to AgNP by serum components significantly inhibit GE.

Chapter 6 aims to further lower the limit of detection for the NT-proBNP metalloimmunoassay, which contains spherical silver nanoparticles (sAgNPs), by incorporating the use of silver nanocubes (AgNCs) into the assay. This work revealed that by using an optimal volumetric ratio of both NPs in a single assay that the total collected Ag charge could be increased by 20%. The addition of the AgNCs in the assay also led to a threefold decrease in the limit of detection for a model assay, as well as a decrease of one order of magnitude in the antigen-specific assay for NT-proBNP. This improvement allowed for the linear dynamic range of the NT-proBNP assay to overlap with the clinically relevance concentration range used by physicians to determine patient treatment.

Chapter 2: Detection of Silver Nanoparticles by Electrochemically Activated Galvanic Exchange

2.1 Synopsis

This chapter presents on the seemingly simple process of galvanic exchange (GE) between electrogenerated $AuCl_4^-$ and silver nanoparticles (AgNPs). The results were obtained in the specific context of using AgNPs as labels for bioassays in paper fluidic devices. Results obtained from a combined electrochemistry and microscopy study indicate that the GE process results in recovery of only ~5% of the total equivalents of Ag present in the system. This low value is a consequence of two factors. First, after an initial fraction of each AgNP undergoes GE, a Au shell forms around the remaining AgNP core preventing further exchange. Second, to simulate a true biological fluid, the experiments were carried out in a Cl^- -containing buffer. Consequently, some Ag^+ formed during GE precipitates as AgCl, and it also serves to block additional GE. Following optimization of the GE process, it was possible to detect AgNP label concentrations as low as 2.6 fM despite these limitations.*

* Chapter 2 is based on previous publication: M. R. Kogan, N. E. Pollok, Crooks, R. M. Detection of Silver Nanoparticles by Electrochemically Activated Galvanic Exchange. *Langmuir*. 2018, 34, 15719–15726. MRK and NEP contributed equally to the work. RMC was the research advisor. MRK and NEP designed and performed the experiments. MKR, NEP, and RMC wrote the manuscript.

2.2 Introduction

We recently reported the use of silver nanoparticle (AgNP) labels for electrochemical detection of biomolecules[58,59,61,66] in paper microfluidic sensing devices.[6,67–70] In this approach (Illustration 2.1), multiple AgNPs are linked to a single magnetic microbead (MμB) in the presence of a target. This MμB-AgNP conjugate is then drawn to an electrode surface by a magnetic force, and the number of AgNPs is analyzed electrochemically. Because there is a one-to-one correspondence between the number of target molecules and the number of AgNPs, the presence of the target is amplified in proportion to the charge stored in each AgNP.[57–59]

We have used two closely related electrochemical methods to detect the presence of the AgNP labels. In both cases the AgNPs are chemically oxidized, the resulting Ag^+ is electrodeposited onto the surface of an electrode, and then the amount of deposited Ag is determined by anodic stripping voltammetry. The two methods vary only in the method of initial oxidation of the AgNPs. In one case they are chemically oxidized using a chemical reagent such as permanganate (MnO_4^-),[57,61] bromine,[54,71] or hypochlorite (bleach),[58] and in the other the oxidation is accomplished by a process known as galvanic exchange (GE).[59,67,74–77] Note that because the AgNPs are not in physical contact with

the electrode surface, it is not possible to oxidize them directly.[61]

GE, which is sometimes called galvanic replacement, has been used for decades to efficiently replace one metal with another.[73,74,76] GE occurs when a zerovalent metal is immersed in a solution containing the oxidized form of a more noble metal (e.g., a higher standard potential). The two metals undergo a spontaneous exchange of electrons, leading to oxidation of the less noble metal (e.g., Ag, E^0 = 0.79 V) and reduction of the more noble metal (e.g., Au, E^0 = 1.52 V).[65] There have been a number of interesting fundamental and practical reports relating to GE. For instance, Adzic and coworkers studied the electrocatalytic oxygen reduction reaction using nanoparticles (NPs) having Pt shells deposited onto different types of metal cores by GE.[77,78] In another report, Xia and coworkers used AgNPs and Ag nanowires as templates to study the morphology of the materials resulting after addition of metal salts having higher reduction potentials.[73,79–81]

Because AgNPs are available commercially in different sizes and shapes, and because Ag has a relatively low reduction potential, AgNPs are often used as templates for GE.[73,74,82,83] For example, a number of groups have studied how the optical properties, composition, and morphology of AgNPs change upon

addition of $HAuCl_4$.[79,84–88] An important outcome of these studies is that, depending upon conditions, both AgCl and Ag^+ can result, as shown in eqs 2.1 and 2.2.[81,82,89–91]

$$4Ag + AuCl_4^- = 4AgCl + Au \qquad (2.1)$$

$$Ag + AuCl_4^- = Ag^+ + Au + 4Cl^- \qquad (2.2)$$

Importantly, eq 2.1 can lead to deposition of both a Au shell and/or an insoluble AgCl shell on the surface of the AgNPs, thereby blocking penetration of $AuCl_4^-$ to the underlying AgNP that remains and preventing complete GE.[91] As we will discuss later, this is an important consideration in our study.

In the present chapter, we focus on the details of the GE processes represented by eqs 2.1 and 2.2. The experiments are carried out using the approach displayed in Illustration 2.1, which, with one exception, is directly relevant to the detection scheme we have used in previous publications focused on chemical sensing.[59,66] The one exception is that here we have used 110 nm AgNPs and in our prior studies the size was 20 nm. We found it necessary to use the larger particles so that they could be easily imaged by electron microscopy (vide infra).

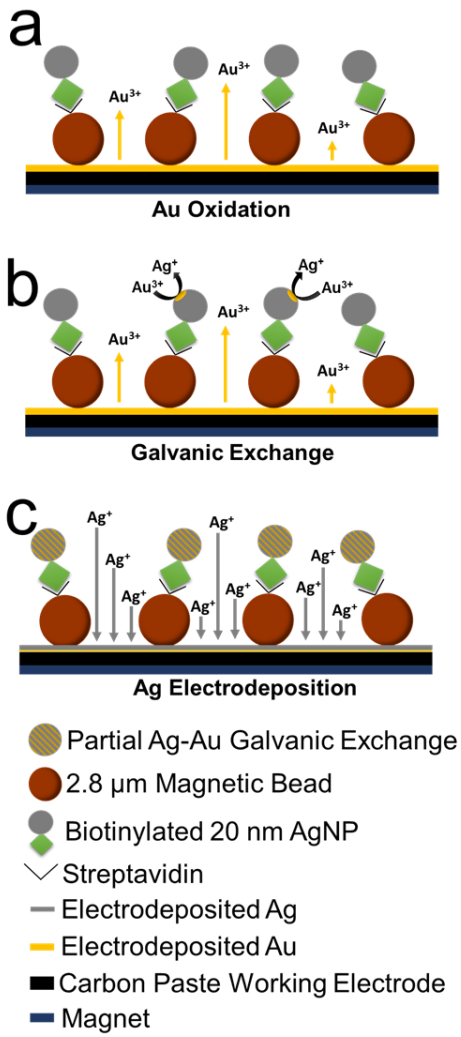

Illustration 2.1 Galvanic exchange detection method.

As shown in Illustration 2.1a, GE is implemented as follows. First, a small amount of Au is electrodeposited onto a carbon paste working electrode. Next, the MµB-AgNP conjugates are drawn to the electrode surface by a magnetic force. At this point, a fraction of the Au is electrochemically oxidized to initiate GE with the AgNPs. During GE, eqs 2.1 and 2.2 proceed

from left to right. This results in formation of Ag^+ (Illustration 2.1b), which is subsequently electrodeposited onto the electrode surface as zero-valent Ag (Illustration 2.1c). A final anodic stripping voltammetry step makes it possible to determine the total Ag charge recovered from the GE reaction. Note, however, that Illustration 2.1 is a highly simplified representation of the GE process. For example, it ignores the possibility of AgCl formation, incomplete GE, and mass transfer considerations. The objective of the present study is to better define the complex nature of this seemingly simple process so that it can be used for electrochemical sensing applications.

2.3 Experimental

2.3.1 Chemicals and Materials

All solutions were made using deionized (DI) water (>18.0 MΩ-cm, Milli-Q Gradient System, Millipore, Bedford, MA). NaCl, NaOH, HCl, $HAuCl_4$, KNO_3, citric acid monohydrate, 4-(2-hydroxymethyl)-1-piperazineethanesulfonic acid (HEPES), Whatman Grade 1 chromatography paper (180 µm thick, 20 cm x 20 cm sheets, linear flow rate of water = 0.43 cm/min), and siliconized low-retention microcentrifuge tubes were purchased from Fisher Scientific (Pittsburgh, PA). Boric acid was purchased from EM Science (Gibbstown, NJ). Citrate-capped AgNPs (nominal 110 nm diameter)

were purchased from Ted Pella (Redding, CA). A solution containing 0.10 M borate and 0.10 M NaCl (referred to henceforth as BCl) was prepared by dissolving appropriate amounts of boric acid and NaCl in DI water, and then adjusting the pH to 7.5 with NaOH.[66]

Conductive carbon paste (Cl-2042) was purchased from Engineered Conductive Materials (Delaware, OH). Cylindrical neodymium magnets (1/16 in x ½ in, N48) were purchased from Apex Magnets (Petersburg, WV). Streptavidin-coated MμBs (Dynabeads, M-270, 2.8 μm diameter) were obtained from Invitrogen (Grand Island, NY). Lyophilized thiol-DNA-biotin (5'd thiol C6 SS-ACATTAAAATTC-biotin 3') was purchased from Biosearch Technologies (Petaluma, CA). Before use, the DNA-biotin was hydrated with the appropriate amount of DI water to make a final concentration of 1.0 mM.

2.3.2 Electrochemistry

All electrochemical measurements were performed using a CH Instruments model 760B Electrochemical Workstation (Austin, TX). For all electrochemical procedures, the working electrode was stencil-printed carbon paste partially covered with electrodeposited Au (vide infra). The counter and reference electrodes were a Pt wire and a saturated Hg/Hg_2SO_4 electrode respectively, both purchased from CH Instruments (Austin, TX).

The working electrodes were fabricated by patterning sheets of chromatography paper with wax using a Xerox ColorQube 8570DN printer. After printing, the wax was melted through the thickness of the paper by placing it in an oven at 120 ^{0}C for 25.0 s. Next, the paper was cut into 12 rectangles (5.0 cm. x 6.5 cm.). A stencil for defining the 2.0 mm-diameter, disk-shaped electrodes was created using CorelDRAW (Ottawa, ON), and then it was cut into a thin plastic sheet of transparency film using an Epilog laser engraving system (Zing 16). Finally, the stencil was placed over the paper (wax side up), the electrodes were printed through the stencil using conductive carbon paste, and then the carbon paste was left to dry in air for 14 h.

Au was electrochemically deposited onto the carbon paste electrodes using a polytetrafluoroethylene electrochemical cell.[59,66] Au electrodeposition was carried out using a solution containing 300.0 µL of 6.0 mM $HAuCl_4$ and 0.10 M KNO_3.[59,67,94] Au electrodeposition onto the carbon paste working electrode was initiated by stepping its potential from 0 V to -0.20 V vs. Hg/Hg_2SO_4 for 2.0 s. This potential was chosen based on the $AuCl_4^-$ reduction wave.[59,66] During reduction, Au nucleated on the carbon paste electrode resulting in dispersed gold nanoparticles (AuNPs).[67,95] This modified electrode will be referred to hereafter as the "carbon/Au working electrode". After Au

electrodeposition, the electrode was rinsed twice with DI water and dried with a Kimwipe.[66]

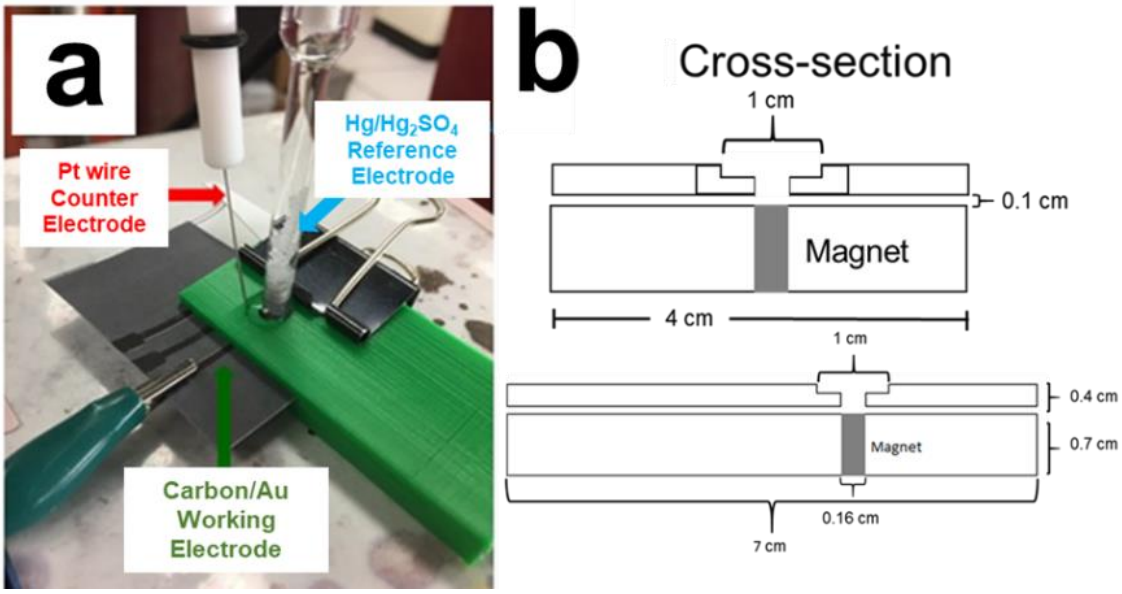

Illustration 2.2 Description of the polylactic acid (PLA) electrochemical cell used for all Au oxidation, Ag electrodeposition, and anodic stripping voltammetry measurements. (a) Photograph of the cell showing the three electrodes connected. (b) Cross-sectional view with dimensions. This cell was printed using a Modified MakerBot Replicator 2s 3D printer using PLA. A magnet was glued into the opening on the back side of the PLA cell, which held the MµB-AgNP conjugates on the electrode surface during galvanic exchange (GE). A layer of clear nail polish was painted on the interior of the PLA cell to prevent the BCl supporting electrolyte from leaking during electrochemical measurements. The PLA cell employs three electrodes: a carbon/Au working electrode, a saturated Hg/Hg_2SO_4 reference electrode, and a Pt wire counter electrode. MµB-AgNP conjugates were dropcast onto the working electrode, dried, slid into the 0.10 cm opening of the cell, and aligned in the center of the top opening of the PLA cell. In this position, the magnet in the bottom opening of the cell is directly behind the working electrode. To keep the working electrode in place, a binder clip was used to clamp the PLA cell and the chromatography paper together. After all three electrodes were in place, 150.0 µL of BCl was pipetted into the opening of the PLA cell.

The GE reactions and Ag anodic stripping voltammetry were carried out using an electrochemical cell printed with polylactic acid (PLA) using a Modified MakerBot Replicator 2s 3D printer. This cell is referred to hereafter as the "PLA cell" (Illustration 2.2). After the PLA cell was printed, a single coat of clear nail polish, obtained from Electron Microscopy Sciences (Hartfield, PA), was applied to the interior of the cell to seal it and prevent leakage of BCl electrolyte solution. The charge corresponding to AgNP concentration was calculated by integrating the anodic stripping voltammetry peaks using Origin Pro8 SR4 v. 8.0951 (Northampton, MA).

2.3.3 Preparation of the MµB-AgNP conjugate

Biotinylated DNA was immobilized on 110 nm AgNPs using a previously reported fast, pH-assisted method.[67,96,97] The biotinylated DNA immobilized on the AgNPs will henceforth be referred to as "AgNP-biotin". Next, 400 µL of the AgNP-biotin (2.4 x 10^9 AgNPs/mL) was mixed with 16 µL streptavidin-coated MµBs (6-7 x 10^8 MµBs/mL), and the solution was shaken (1400 rpm) for 30 min at 23 ^{0}C.[61,67,98] Following conjugation, the MµB-AgNP conjugates were washed three times by holding the microcentrifuge tube up to a magnet, removing the supernatant, and resuspending in 16 µL BCl.[61,67]

2.3.4 Transmission electron microscopy (TEM)

Size analysis of the AgNPs before and after biotin modification was carried out using a JEOL 2010F TEM having a point-to-point resolution of 0.19 nm. Samples were prepared by pipetting 2.0 µL of unmodified or modified AgNPs onto a carbon-coated Cu grid obtained from Electron Microscopy Sciences (Hartfield, PA). The size distributions were determined using ImageJ software and 200 randomly selected particles (Figure 2.1).

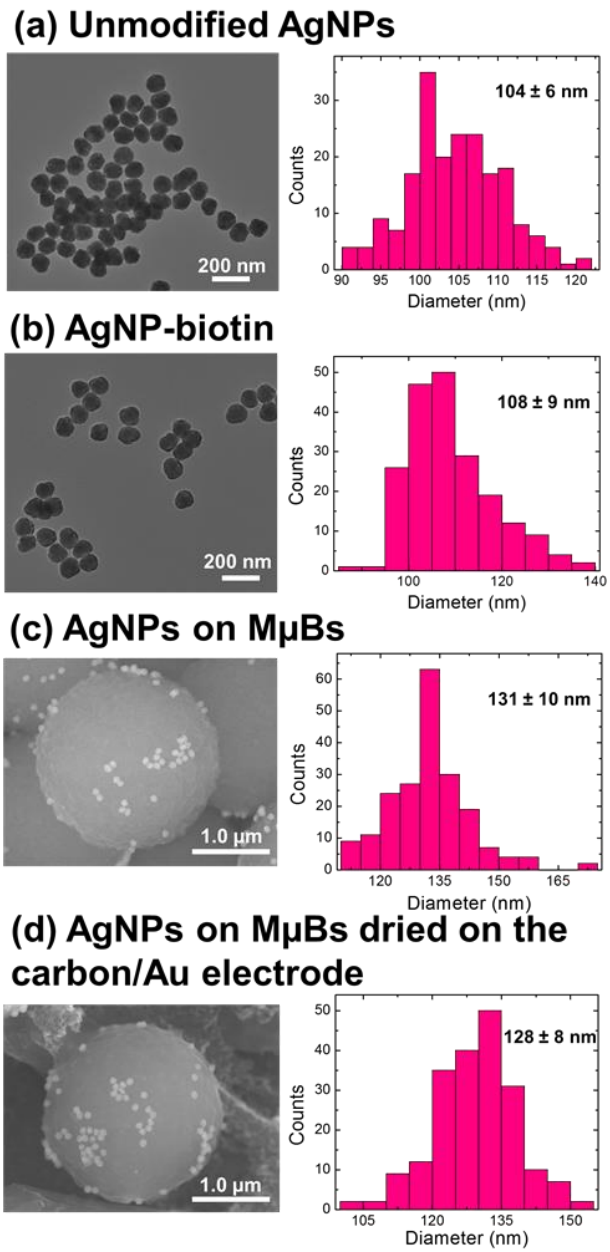

Figure 2.1 TEM micrographs and size-distribution histograms of AgNPs before and after immobilization on MμBs. AgNPs (a) before and (b) after binding to DNA-biotin. A carbon-coated Cu grid was used for the TEM micrographs. SEM micrographs and size-distribution histograms for AgNPs present as (c) the MμB-AgNP conjugate on a carbon-coated Ni grid and (d) the MμB-AgNP conjugate on a carbon/Au working electrode. Each of the histograms are based on 200 randomly selected particles.

Energy-dispersive X-ray (EDX) analysis of the MµB-AgNP conjugates was performed using a JEOL 2010F TEM. The samples for this analysis were prepared by removing the MµB-AgNP conjugates from the carbon/Au working electrode (after electrochemical analysis) using a micropippette. The MµB-AgNP conjugates were then added to 100.0 µL of isopropylalcohol in a microcentrifuge tube, and sonicated for 10.0 min. Next, the sample was pipetted onto a Si_3N_4 TEM grid (Ted Pella, Redding, CA) and dried for 15.0 min under a heat lamp. Finally, a 200 mesh carbon-coated Cu grid obtained from Electron Microscopy Sciences (Hartfield, PA) was laid on top of the sample to prevent the MµBs from adhering to the magnetic portions of the TEM instrument.

2.3.5 Scanning electron microscopy (SEM)

SEM micrographs were obtained using a Hitachi S5500 SEM instrument having an accelerating voltage of 30 kV, and a point-to-point resolution of 0.4 nm. Samples of the MµB-AgNP conjugates were prepared by drop casting 2.0 µL of the MµB-AgNP conjugates on a carbon-coated Ni grid (Electron Microscopy Sciences, Hartfield, PA) and then dried in air for ~12 h. The size distribution of the AgNPs on the MµBs were also analyzed by randomly selecting 200 particles in ImageJ (Figure 2.1). The AgNP coverage on the MµBs was determined by counting the number

of AgNPs present on the surface of the MµBs using ten different SEM micrographs (Figure 2.2).

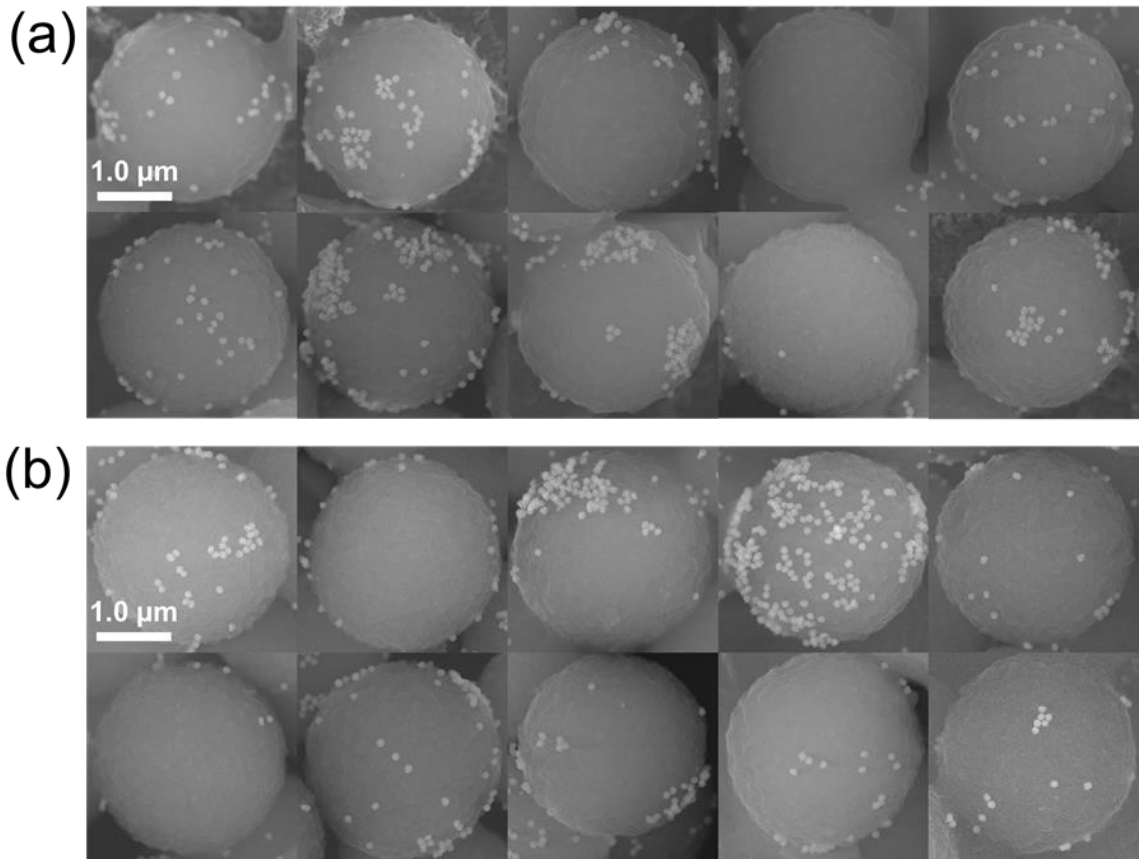

Figure 2.2 SEM micrographs showing representative AgNP distributions on the MµBs used in this study. Ten MµBs imaged on (a) a carbon-coated Ni grid and (b) a carbon/Au working electrode. The samples were prepared as follows. 16 µL of the MµB-AgNP conjugates were formed following the procedure provided in the Experimental Section of Chapter 2, and then 2.50 µL of this solution were pipetted onto a carbon-coated Ni grid or 0.50 µL were pipetted onto a carbon/Au working electrode. Both types of samples were air dried for 14.0 h. The number of AgNPs/MµB, averaged over all 20 MµB, was 106 ± 100 AgNPs. Due to the large standard deviation of the experimentally determined value, the number of AgNPs/MµB used to prepare the MµB-AgNP conjugates (94 AgNPs per MµB) was used for collection efficiency calculations.

SEM micrographs of the carbon/Au working electrode before and after immobilization of the MμB-AgNP conjugates were obtained by removing the electrode from the PLA cell, cutting out a section of the electrode (3.0 x 5.0 mm), drying in air for 12.0 h, and then attaching the electrode section to the stage of a Hitachi SEM Standard Holder with conductive carbon tape. The AgNP size distrubtion (Figure 2.1) and coverage of the AgNPs on the MμBs (Figure 2.2) were both quantified as previously described. EDX was carried out using Bruker ESPRIT imaging software (Billerica, MA). The EDX detector was a Bruker XFlash 4010 with a detector area of 10 mm^2 and an energy resolution of 129 eV at the Mn K_{α} peak.

2.4 Results and Discussion

2.4.1 Electron microscopy of the MμB-AgNP conjugates

The primary goal of this project is development of a better understanding of the complex nature of the seemingly simple GE process between $AuCl_4^-$ and AgNPs.[73,74,82,97] As mentioned earlier, Illustration 2.1 neglects numerous potential subtleties that are important when using this labeling approach for biosensing applications. Accordingly, to better understand this process, we first examined the MμB-AgNP conjugates by electron microscopy.

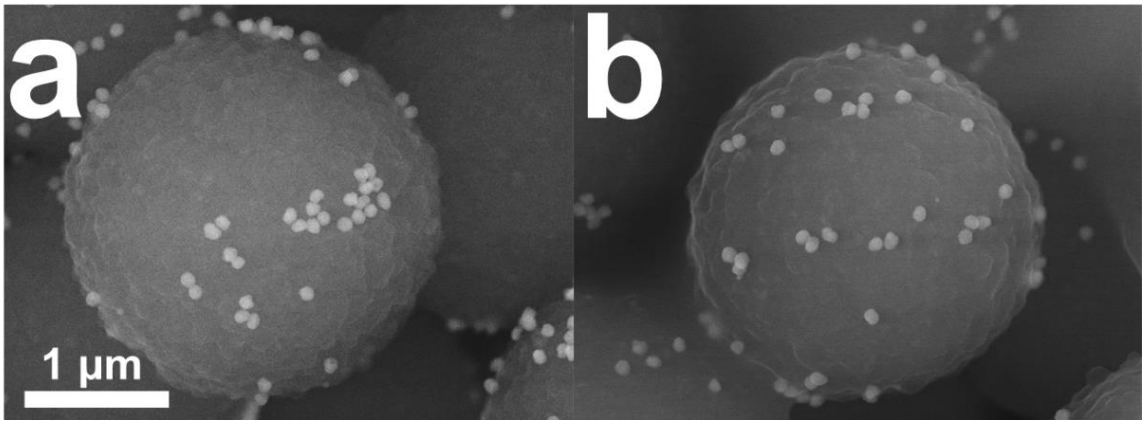

Figure 2.3 SEM micrograph of the MµB-AgNP conjugate on (a) a TEM grid and (b) dried onto a carbon/Au working electrode prior to electrochemical activation.

Figure 2.3a is a representative SEM micrograph of a MµB-AgNP conjugate dried onto a carbon-coated Ni grid prior to GE. EDX data (Figure 2.4) confirms that the NPs present on the MµBs are composed of Ag. Qualitatively, it is clear that AgNPs sparsely cover the MµBs, and quantitative analysis of 20 MµBs (Figure 2.2) indicates the presence of 106 ± 100 AgNPs/MµB. On the basis of the AgNP:MµB ratio used to prepare the conjugates, the maximum coverage should be 94 AgNPs per MµB. We conclude, therefore, that essentially 100% of the AgNPs introduced to the MµBs are immobilized thereon. Due to the variability in the number of MµB-AgNP conjugates measured experimentally, we adopt the calculated average number of 94 AgNPs/MµB for subsequent analysis.

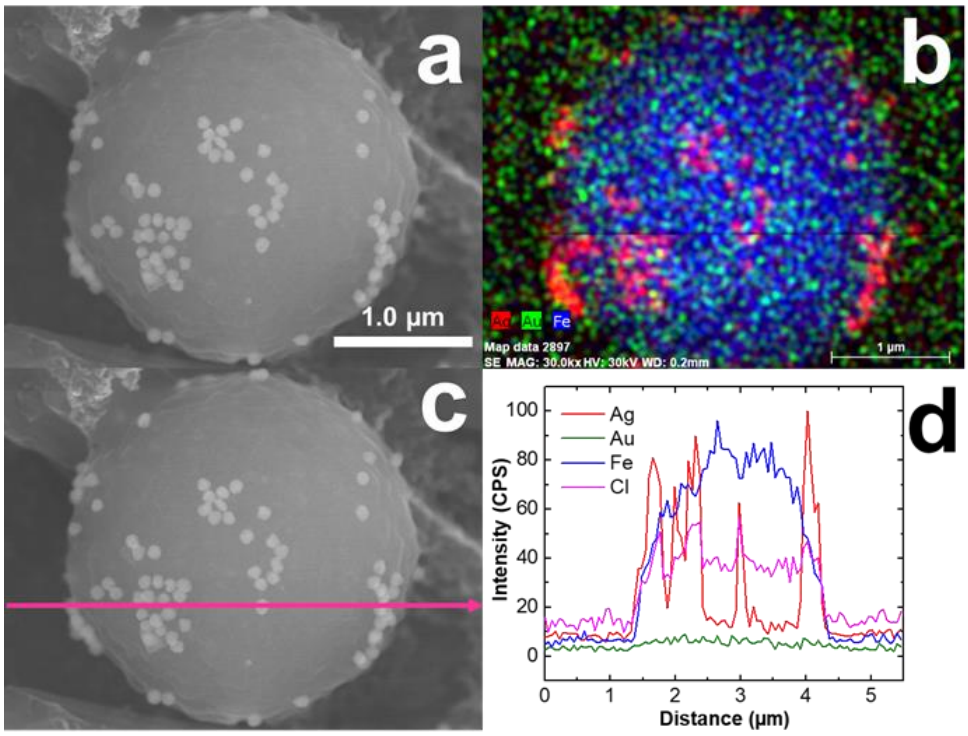

Figure 2.4 Microscopy and EDX analysis of the MµB-AgNP conjugates before electrochemistry. The MµB-AgNP conjugate was immobilized on the carbon/Au working electrode. (a) SEM micrograph of the MµB-AgNP conjugate and (b) EDX element map showing Fe (blue), Ag (red), and Au (green). (c) The micrograph in (a) with a pink line indicating the position of the line scan shown in (d). Fe is coincident with the magnetic core of the MµB and Ag is present on the periphery. Au is only present at the background level. Cl is also present.

The size of the MµB-bound AgNPs is 131 ± 10 nm, which is larger than the size of AgNP conjugates prior to immobilization on the MµBs (106 ± 10 nm, Figure 2.1). It is unlikely that this discrepancy is real, but rather it probably arises from the difficulty of accurately measuring the AgNP size after immobilization on the MµBs.

Figure 2.3b is a representative SEM micrograph of the MµB-AgNP conjugates dried on the carbon/Au working electrode. The shape (spherical) and size of the AgNPs before and after immobilization of the MµBs on the electrode (131 ± 10 nm vs. 128 ± 8 nm, respectively) are the same. Additional SEM micrographs of the MµB-AgNP conjugates following immobilization onto the working electrode are provided in Figure 2.2b. The main point of this initial assessment is that immobilization of the MµB-AgNP conjugates onto the carbon/Au working electrode does not result in any significant alteration of their physical properties.

One final point: the micrographs shown in Figures 2.1-2.4 suggest that a small number of AgNPs may be in direct contact with the electrode surface. However, control experiments (Figure 2.5) indicate that if this is the case, they are not electrochemically detectable.

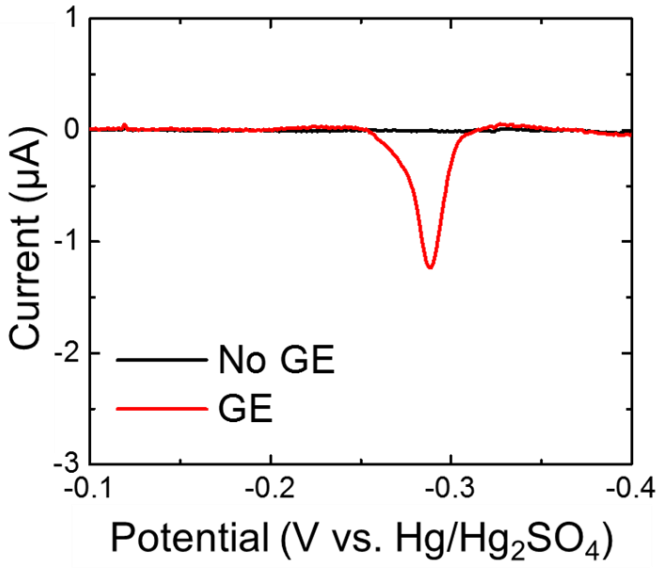

Figure 2.5 Linear sweep voltammograms (LSVs) demonstrating that direct oxidation of AgNPs is below the electrochemical detection limit. The black trace shows the LSV associated with direct electrochemical detection of AgNPs, and the red trace results from galvanic exchange. The black trace was obtained as follows. First, 0.50 μL of the MμB-AgNP conjugate, having a AgNP concentration of 25.0 fM, was dried at the carbon/Au working electrode. Second, the electrode was placed into the PLA cell and 150.0 μL of BCl was added. Third, the electrode potential was swept from -0.70 V to 0.20 V. No AgNP oxidation was detected, and therefore we conclude that few AgNPs are in direct contact with the electrode surface. The red trace was obtained following galvanic exchange, as described in the caption for Figure 2.17. In this case a substantial stripping current obtains. In summary, current is only observed when the AgNPs are oxidized by galvanic exchange. Note that the scan rate for both traces 50 mV/s and sloping baselines in the original data were corrected.

2.4.2 Galvanic exchange

After ensuring the fidelity of the MμB-AgNP conjugates after adsorption onto the working electrode, we sought to understand how they change following GE. These experiments were carried out as shown in Illustration 2.1. First, 0.50 μL of the MμB-

AgNP conjugates were pipetted onto the carbon/Au working electrode, and then the electrode was dried in air for 20.0 min. Given the number of MµBs in this volume of solution, the surface area of the electrode, and assuming the MµBs are in a hexagonal close-packed lattice, this would correspond to a coverage of about 1.5 monolayers of MµBs on the electrode. Because the MµBs are not close-packed, however, this represents a lower limit on the thickness of the MµB layer. An optical micrograph of the MµBs on the electrode is provided in Figure 2.6.

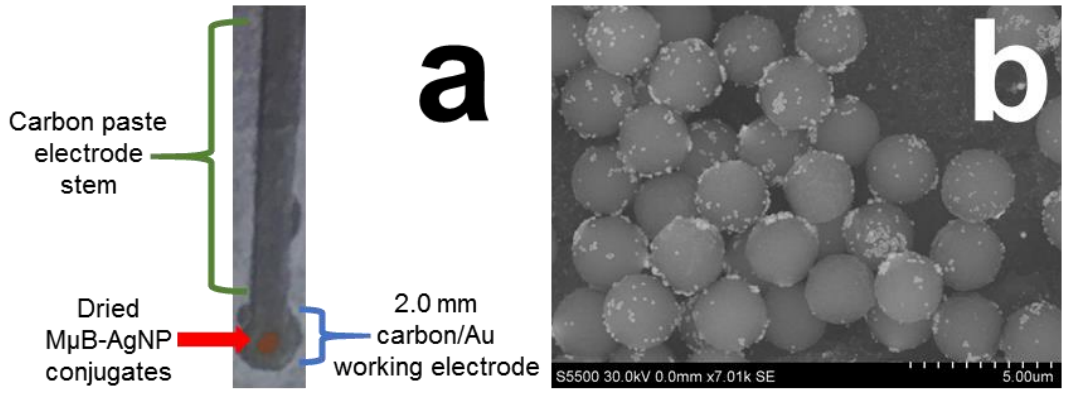

Figure 2.6 Micrographs of the MµB-AgNP conjugates dried on a carbon/Au working electrode. (a) An optical micrograph of the MµB-AgNP conjugates dried on the carbon/Au working electrode. (b) An expanded view (SEM micrograph) of the MµB-AgNP conjugates in (a). The micrographs were obtained by pipetting 0.50 µL of a 337 fM MµB-AgNP conjugate solution onto a carbon/Au working electrode and then drying in air for 20.0 min. The results indicate that the distribution of conjugates is rather uniform, but that there are patches on the electrode surface where no MµBs are present.

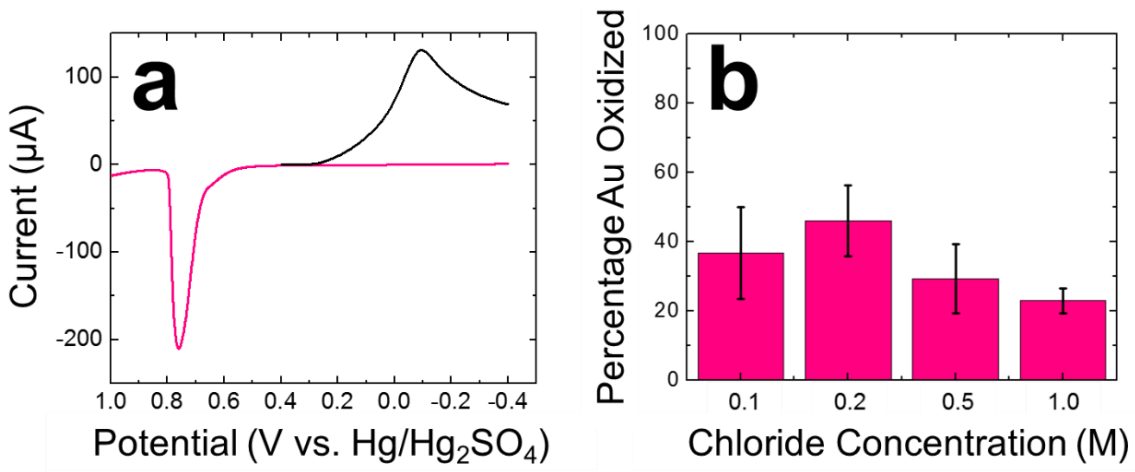

Figure 2.7 Experiment showing the relationship between the percentage of Au oxidized from the carbon/Au electrode as a function of chloride concentration. (a) Reduction of $AuCl_4^-$ (black trace) and oxidation of Au (pink trace) from a carbon paste electrode. (b) The percentage of Au oxidized from the carbon paste working electrode at different Cl^- concentrations. The experiment was carried out as follows. First, a carbon paste electrode was placed into a polytetrafluoroethylene electrochemical cell filled with 300.0 μL of 6.0 mM $HAuCl_4$ and 0.10 M KNO_3.[59,66] Next the electrode potential was swept from 0.40 V to -0.40 V vs. Hg/Hg_2SO_4, resulting in reduction of $AuCl_4^-$ as shown by the black trace in (a). Second, the electrode was removed at the open-circuit potential and rinsed twice with DI water. Third, the electrode was placed into the PLA cell with BCl electrolyte solutions having the NaCl concentrations indicated in (b). Finally, the potential was swept from -0.40 V to 1.0 V to oxidize Au. The areas under the peaks (charges) resulting from these experiments (e.g., Frame (a)) were obtained, and the percentage of Au oxidized as a function of the amount of deposited Au is displayed in (b). Each histogram corresponds to give independent replicates. The results indicate that, within error, the percentage of Au oxidized is independent of the chloride concentration.

Second, the MμB-AgNP conjugate-covered electrode was placed into the PLA cell, and then 150.0 μL of BCl electrolyte solution was added. The BCl electrolyte solution contained 0.10 M NaCl, which is sufficient to oxidize excess Au from the carbon/Au

working electrode (Figure 2.7). Next, the working electrode potential was stepped from 0 to 0.60 V for 25.0 s. This potential results in oxidation of a fraction of the previously electrodeposited Au thereby initiating GE.[59,66] Moreover, on the basis of the diffusion coefficient calculated for $AuCl_4^-$ (Figure 2.8), 25.0 s is sufficient time for $AuCl_4^-$ to reach all of AgNPs present in the vicinity of the electrode.[65] Following GE, the electrode potential was immediately stepped from 0 V to -0.70 V for 100.0 s to electrodeposit Ag. The combination of electrochemical oxidation of Au and subsequent deposition of Ag is referred to hereafter as "one GE cycle". Finally, the electrode was removed from the PLA cell at the open-circuit potential, dried, and analyzed by SEM (Figure 2.9).

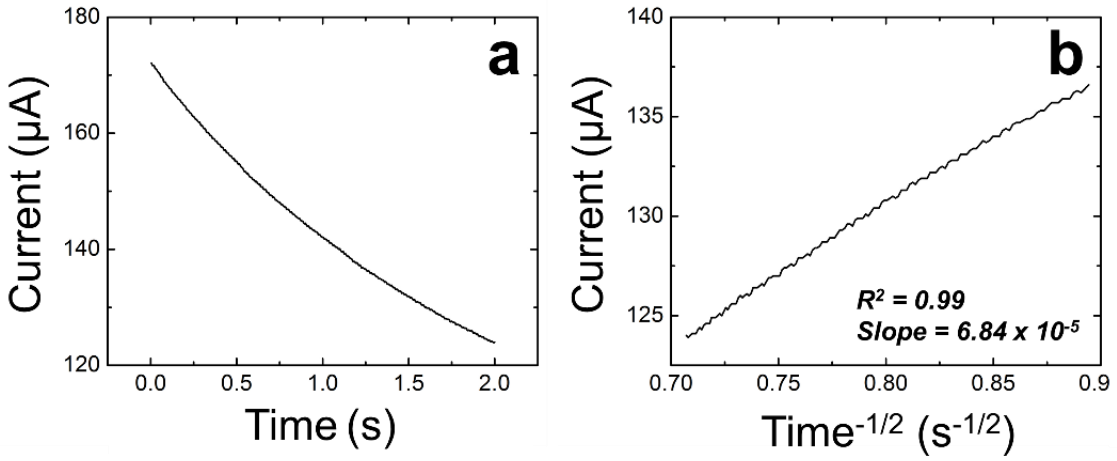

Figure 2.8 Electrochemical data used to calculate the diffusion coefficient of $AuCl_4^-$. The $AuCl_4^-$ diffusion coefficient was determined using the current-time trace for $AuCl_4^-$ reduction shown in Frame (a). The Cottrell plot in Frame (b) was obtained using the current from 1.25 s to 2.00 s. The values required to calculate the diffusion coefficient of $AuCl_4^-$ are the $AuCl_4^-$ concentration (6.0×10^{-6} mol/cm^3), the area of the carbon paste working electrode (0.03 cm^2), the number of electrons transferred (n=3.0), the Faraday constant (96,485 C/mol), and the slope of the Cottrell line in (b) (6.84×10^{-5} A $s^{1/2}$).[65] The calculated diffusion coefficient of $AuCl_4^-$ is 4.9×10^{-5} cm^2/s. As discussed in the Results and Discussion section of Chapter 2, galvanic exchange is initiated by oxidation of Au present on the carbon electrode for 25.0 s. Using the calculated $AuCl_4^-$ diffusion coefficient, we determined that $AuCl_4^-$ can diffuse ~500 μm from the surface of the carbon/Au working electrode. This distance is sufficient to reach the AgNPs on all MμBs concentrated at the working electrode. These experiments were performed in the polytetrafluoroethylene electrochemical cell discussed in the Experimental Section of Chapter 2.[66]

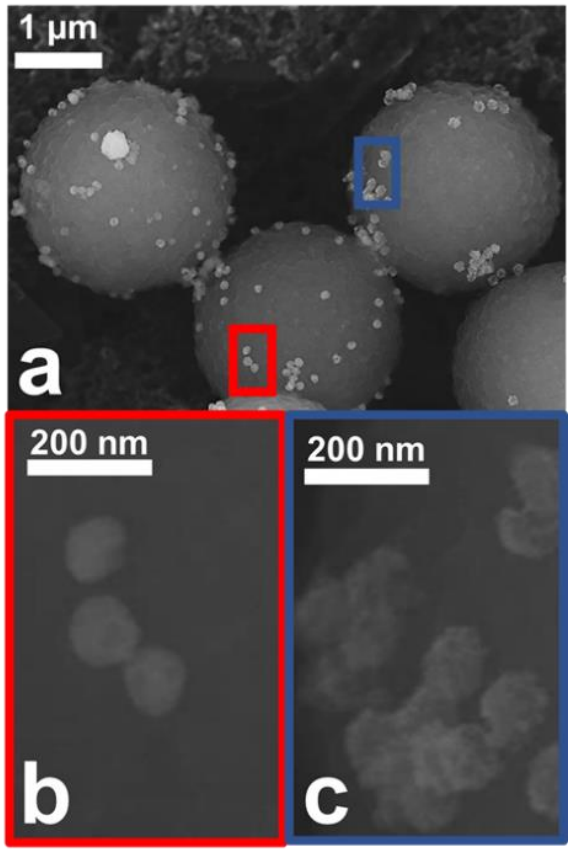

Figure 2.9 SEM micrographs of MµB-AgNP conjugates imaged on the carbon/Au working electrode after one GE cycle. (a) A low-resolution view. (b,c) Expanded views of the regions highlighted by the red and blue boxes, respectively, in (a).

The micrograph in Figure 2.9a shows the MµB-AgNP conjugates dried on the carbon/Au working electrode immediately following GE. At the resolution of this micrograph, there are no significant changes in morphology of the AgNPs compared to the images obtained prior to GE shown in Figure 2.3. Higher resolution images of the AgNPs (Figures 2.9b and 2.9c) are somewhat more illuminating, however. For example, Figure 2.9b

shows that some of the NPs maintain their size, smooth texture, and generally spherical shape even after GE (Figure 2.3). In contrast, the AgNPs shown in Figure 2.9c exhibit a morphology change, probably resulting from GE.

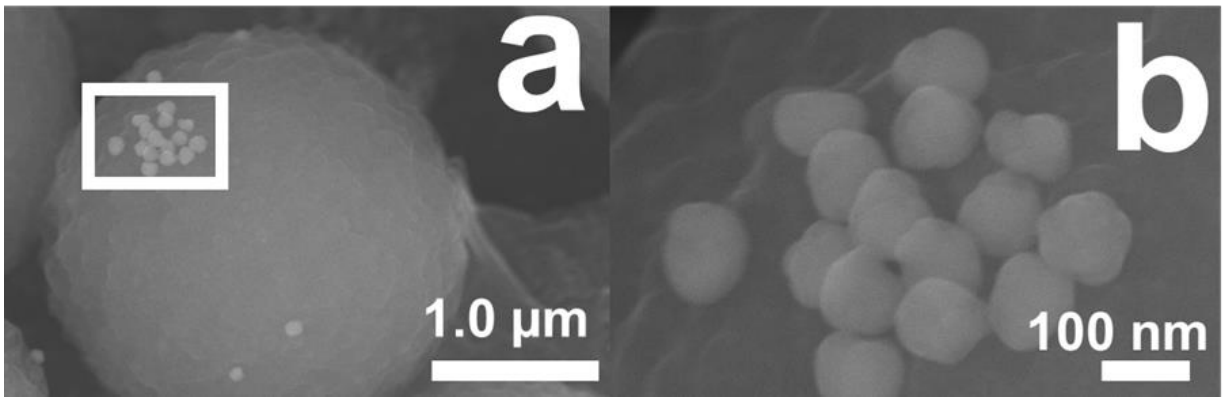

Figure 2.10 SEM micrographs of the MµB-AgNP conjugates after one GE cycle, but in the absence of Au. (a) MµB-AgNP conjugates after one GE cycle. (b) Expanded view of the boxed area in (a). The AgNPs appear identical before and after electrochemistry. We conclude that in the absence of GE, there is no change in morphology of the AgNPs.

Note that when the same electrochemical program is applied, but in the absence of Au (Figure 2.10) the spherical shape and smooth texture of the imaged AgNPs are conserved. This control experiment further implicates the GE process as being responsible for the morphological changes observed in Figure 2.9c. Indeed, it has been shown previously that GE between AgNPs and $AuCl_4^-$ leads to changes in the shape of the parent AgNPs. Specifically, AuAg alloys form with shapes that include nanocages[79,90,98,99] and core@shell structures.[86,100,101]

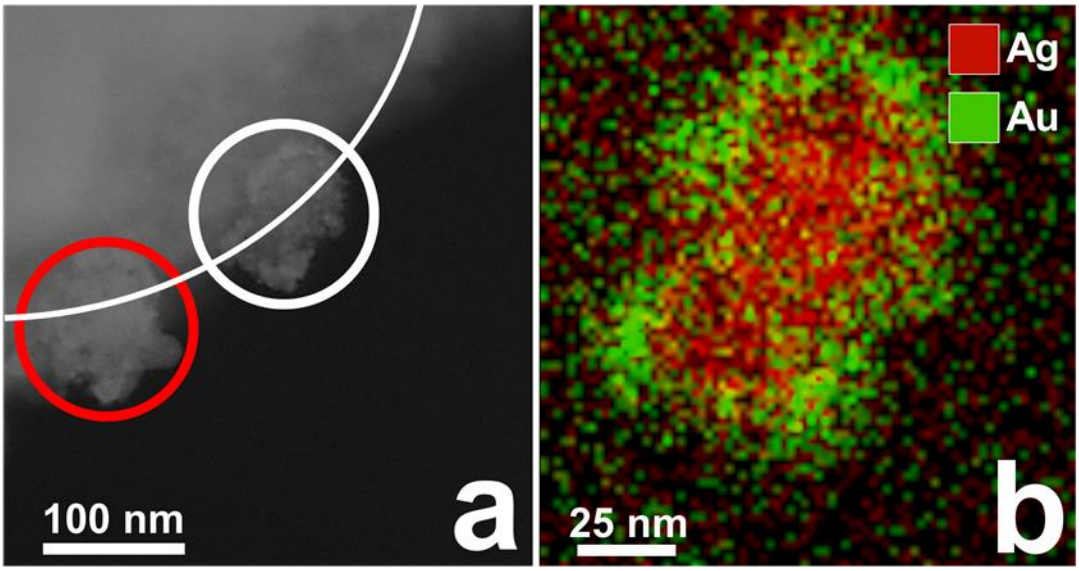

Figure 2.11 (a) TEM micrograph of a portion of a MμB-AgNP conjugate after one GE cycle. The white arc approximates the edge of the MμB, the red circle highlights one associated NP, and the white circle highlights a pair of closely spaced NPs. (b) An EDX element map of the NPs in the white circle in (a). It reveals a Ag core (red) surrounded by a Au shell (green).

To further confirm that GE is responsible for the changes shown in Figure 2.9, the MμB-AgNP conjugates were analyzed by TEM and EDX following GE (Figure 2.11). For this experiment, the MμB-AgNP conjugates were dried onto a freshly prepared carbon/Au working electrode. Following one GE cycle, the MμB-AgNP conjugates were removed from the electrode and prepared for TEM analysis as discussed in the Experimental Section. Figure 2.11a is a TEM micrograph of a portion of a MμB-AgNP conjugate after GE. The edge of the MμB is outlined by the curved white line and three NPs are also shown. One of these is highlighted

with a red circle, and a pair of overlapping NPs is highlighted with a white circle. The rough surface morphology of all three NPs resembles those shown in Figure 2.9c, and therefore we conclude that they have undergone GE.

EDX analysis of the two NPs highlighted by the white circle are shown in Figure 2.11b. Here, the green-colored shell corresponds to Au and the red-colored core corresponds to Ag. The width of the Au shell is ~10 nm and the two Ag cores are 25 and 50 nm in diameter.

a

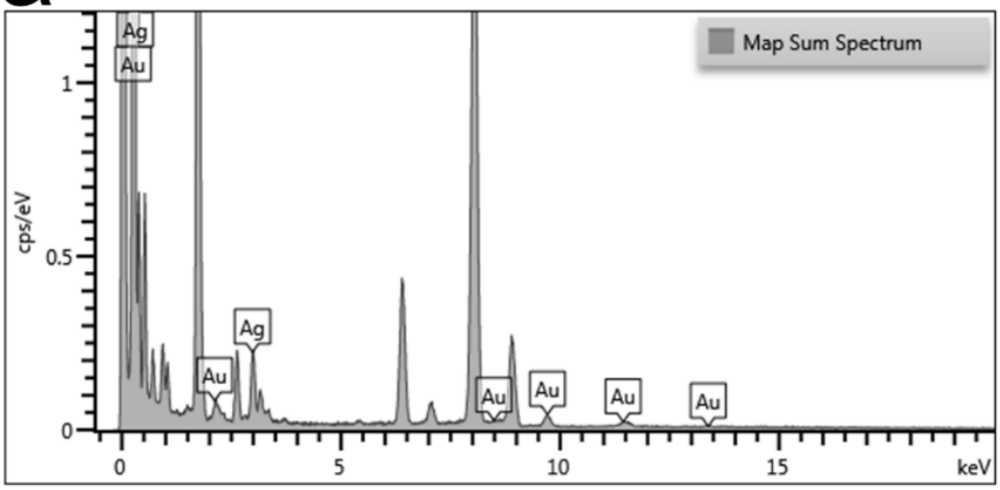

b

Element	Atomic %
Ag	79
Au	21
Total:	100

Figure 2.12 EDX analysis of NPs after one GE cycle. The data were obtained for the NPs circled in white in Figure 2.11. (a) EDX spectrum. (b) The atomic percentages of Ag and Au determined from the spectrum in (a).

Figure 2.12 provides quantitative EDX data for the two NPs circled in white, and it shows that the Au shell comprises ~21 atom% of the NPs. Two conclusions can be drawn from Figure 2.11b. First, electrochemically initiated GE results in only partial exchange of Au for Ag for these ~110 nm-diameter AgNPs. Second, the Au shell that encapsulates the Ag core is probably responsible for the observed incomplete GE.

Clearly, it is only possible to obtain TEM and EDX data for a few NPs following GE, but the foregoing results confirm that there is a correlation between the morphology of the NPs and whether they have undergone GE: rough morphologies correlate to GE, while smooth morphologies correlate to no GE. This finding has allowed us to image many NPs using SEM, which has sufficient resolution to distinguish morphology, and hence determine a statistically meaningful value for the percentage of AgNPs that undergo GE. A detailed explanation for how this analysis was carried out is provided in Figure 2.13.

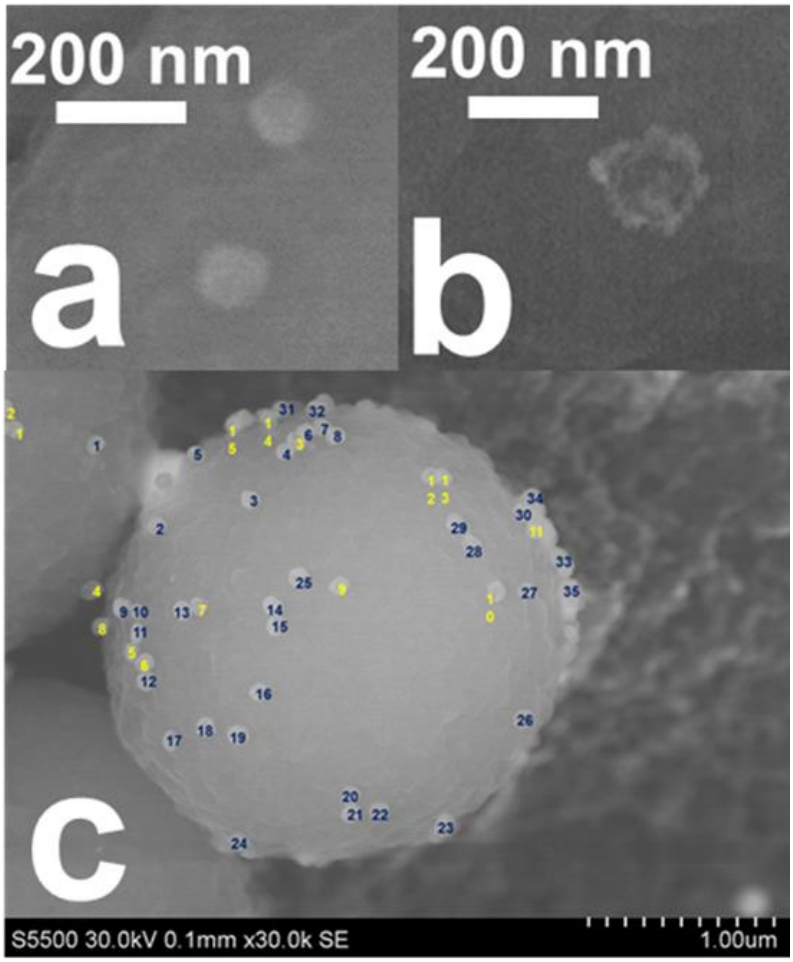

Figure 2.13 Morphology of AgNPs after one GE cycle. The smooth morphology of the two AgNPs in (a) was unchanged after the GE cycle, indicating that they did not undergo GE. The morphology of the AgNP in (b) is much rougher than those in (a), indicating that it did undergo GE with $AuCl_4^-$. (c) The relative numbers of smooth (no GE) and rough (GE) NPs were marked as indicated in this image. The blue numbers represent NPs that remained smooth, and the yellow numbers represent NPs that became roughened.

Briefly, we examined 547 NPs on 25 different MµBs and of these 52% exhibited a morphological change correlated to at least partial GE. We now turn our attention to understanding why the GE reaction does not go to completion.

2.4.3 The MµB-AgNP conjugates after oxidation by $AuCl_4^-$

As discussed earlier, the time allotted for GE (i.e., the duration of the Au oxidation step shown in Illustration 2.1a) is sufficient for $AuCl_4^-$ to diffuse well-beyond the layer of MµBs present on the electrode surface. Hence, it is surprising that a higher percentage of the AgNPs do not undergo GE. In this part of the study, we sought to address this issue by identifying phenomena that could limit GE. This was accomplished using EDX analysis of the MµB-AgNP conjugates following just the first half of the GE cycle (described next).

This experiment was carried out exactly as described in the previous section, except that it was halted immediately after oxidation of Au (e.g., only the steps shown in Frames a and b of Illustration 2.1 were carried out: no redeposition of Ag as in Frame c). Specifically, the working electrode potential was stepped from 0 to 0.60 V for 25.0 s to initiate GE. The electrode was then removed from the PLA cell at open circuit potential, dried, and analyzed by SEM (Figure 2.14).

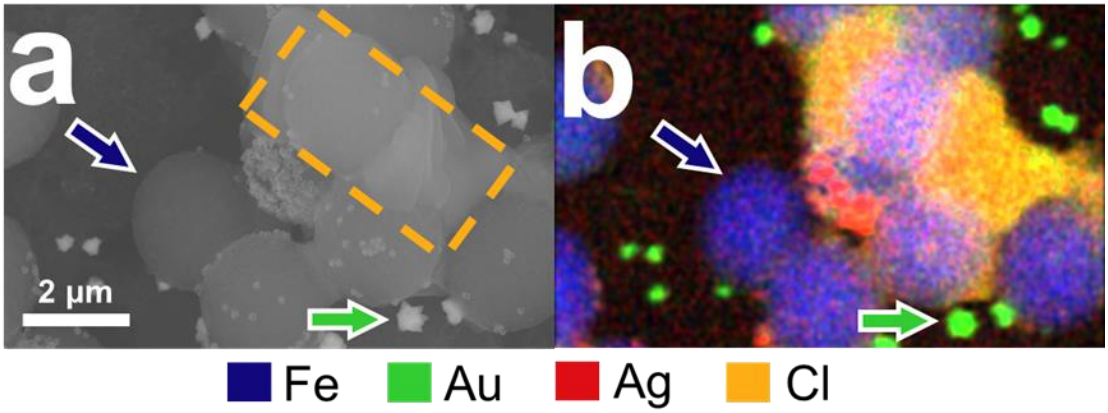

Figure 2.14 (a) SEM micrograph of MµB-AgNP conjugates on the carbon/Au working electrode after oxidation of Au. The orange rectangle highlights salt around the MµB. (b) An element map of the MµB-AgNP conjugates in (a). The blue and green arrows point to the same MµB and Au nodule, respectively, in (a).

Figure 2.14a is an SEM micrograph of the MµB-AgNP conjugates present on the electrode following oxidation of Au. The blue arrow points to a MµB and the green arrow points to a NP structure present on the electrode surface. The area outlined by the orange box contains an unknown material that overlays multiple MµBs. EDX analysis was performed to identify the composition of this material and to determine the identity of the NP indicated by the green arrow.

Figure 2.14b is an EDX color map corresponding to the micrograph in Figure 2.14a. The element map is focused on Fe, Au, Ag, and Cl because of the roles they play during GE. Specifically, Fe is present in the core of the MµBs (blue arrow in Figure 2.14a) and Cl^- is present in the electrolyte. The object highlighted by the green arrow in Figure 2.14a is now

clearly identified as a nodule of Au that was electrodeposited during the fabrication of the electrode (green arrow in Figure 2.14b). The presence of this feature indicates that only a fraction of the Au originally deposited onto the carbon electrode is converted to soluble $AuCl_4^-$ during the positive potential step (Figure 2.7). It also indicates that Au electrodeposited onto the carbon electrode during device fabrication is randomly distributed as NPs on the carbon surface rather than being present as a conformal coating.[66,93] Finally, the structure outlined with an orange box in Figure 2.14a is composed of Ag and Cl, suggesting that it is primarily AgCl.

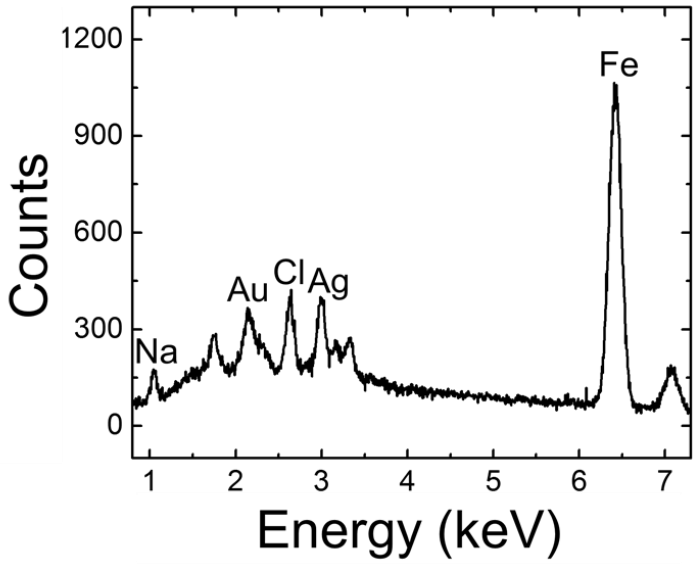

Figure 2.15 EDX spectrum obtained from the region shown in Figure 2.14. The MμB-AgNP conjugates were prepared and processed as discussed in the Experimental section of Chapter 2. This spectrum compares the intensity of the Na, Au, Cl, Ag, and Fe signals resulting from the EDX map in Figure 2.14b.

Figure 2.15 indicates that a small fraction of NaCl is present as well. These findings indicate that AgCl (K_{sp} = 1.8 x 10^{-10})[102] is a product of GE (eq 2.1) under the conditions used in our experiment.[81,82,89,91,103] Indeed, AgCl is a known byproduct of this GE reaction, and can lead to inefficient GE.[82,89-91,99]

The results shown in Figure 2.14 suggest that AgCl encapsulates a significant fraction of the MµB-AgNP conjugates. This most likely reduces access of $AuCl_4^-$ to the underlying AgNPs and hence reduces the GE efficiency.[81,82,90,91,99,103] Importantly, and as shown in Figure 2.9, the mass of AgCl present in Figure 2.14 (orange box in Figure 2.14a) is not visible after a complete GE cycle (all three steps shown in Illustration 2.1). Apparently, some or all of the AgCl is in direct contact with the electrode surface and is reduced to Ag^0 during the second half of the GE cycle (Ag electrodeposition).[59,66]

To summarize, there are two factors that prevent complete oxidation of the AgNPs. First, the presence of a Au shell that prevents access of $AuCl_4^-$ to underlying Ag (Figure 2.11). Second, precipitated AgCl, which also blocks access of $AuCl_4^-$ to some AgNPs.

2.4.4 GE of remaining AgNPs

As just discussed, AgCl is a byproduct of the GE reaction between $AuCl_4^-$ and Ag^0, when it is carried out in Cl^--containing media, that prevents oxidation of about half the AgNPs immobilized on the MμBs. For sensing purposes, we wish to oxidize all the AgNP labels and, in this section, we show that a second GE cycle results in at least partial GE of all the AgNPs present. For these experiments, the potential of the working electrode was stepped from 0 to 0.60 V for 25.0 s and then to -0.70 V for 100.0 s. This program was then repeated. At this point the electrode was removed from the PLA cell at open circuit potential, dried, and analyzed by SEM (Figure 2.16).

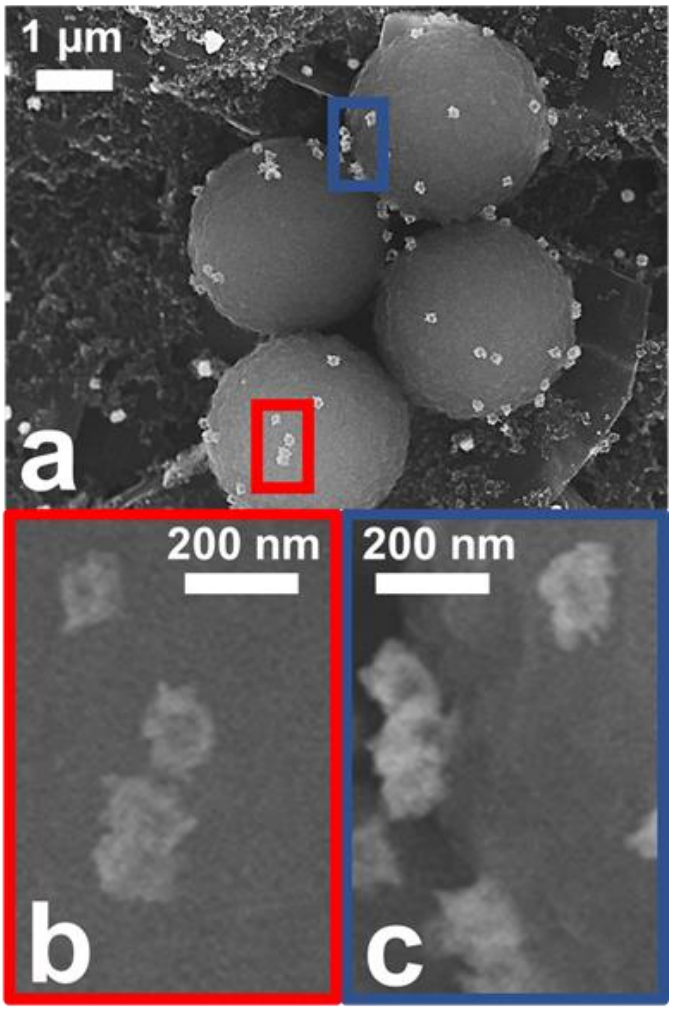

Figure 2.16 SEM micrographs of MµB-AgNP conjugates after two GE cycles imaged on the carbon/Au working electrode. (a) A low-resolution view. (b,c) Expanded views of the regions highlighted by the red and blue boxes, respectively, in (a).

The micrograph in Figure 2.16a shows four MµB-AgNP conjugates present on a carbon/Au working electrode after two GE cycles. The expanded views in Figures 2.16b and 2.16c correspond to the red and blue boxes in Figure 2.16a, respectively. As discussed previously, the distorted surface morphology of these NPs indicates that they have undergone GE.

A total of 547 NPs were examined following two GE cycles, and all of them resembled those in Figures 2.16b and 2.16c. Accordingly, we conclude that two potential cycles result in GE (or, more precisely, at least partial GE) of essentially all the AgNPs present on the electrode surface.

2.4.5 Electrochemical detection of AgNPs after GE cycles

Thus far we have shown that 52% and ~100% of AgNPs exhibit morphological changes after one and two GE cycles, respectively. We correlate these changes to full or partial GE between $AuCl_4^-$ and Ag^0. In this section, we compare these findings to quantitative electrochemical results obtained by Ag anodic stripping voltammetry.

These experiments were carried out exactly as described in the previous sections for one, two, and three GE cycles, except rather than halting the experiment after Ag electrodeposition the potential was swept twice from -0.70 V to 0.20 V at 50 mV/s to oxidize Ag after the final GE cycle. The charge under the second voltammogram for each experiment was then determined by integration.[57–59,61,66]

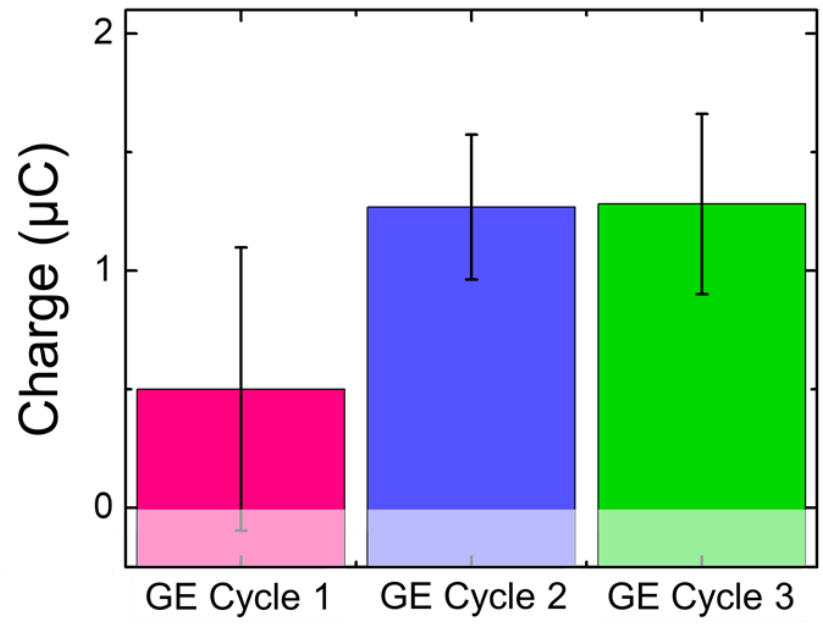

Figure 2.17 Histogram of the average Ag charge measured at 12 different working electrodes after one, two, and three GE cycles. The MµB-AgNP conjugates were dried on the carbon/Au working electrode and rehydrated in 150 µL BCl to give a final AgNP concentration of 45 fM.

Figure 2.17 presents histograms of the charge recovered for 12 independently prepared electrodes for the indicated number of GE cycles. The average Ag charge after one GE cycle was 0.5 ± 0.6 µC. After two and three GE cycles, the charge more than doubled to 1.3 ± 0.3 µC and 1.3 ± 0.4 µC. On the basis of these results, we conclude that only two GE cycles are required to capture all of the accessible Ag charge.

It is now possible to correlate the results obtained by microscopy to the electrochemical data in Figure 2.17. Recall that the microscopy data indicated that the number of AgNPs

exhibiting morphological changes doubled after a second GE cycle. Now we find that the electrochemical data in Figure 2.17 are in near-quantitative accord with this finding, and therefore electrochemistry provides a good measure of the number of AgNPs present.

On the basis of the AgNP concentration used in these experiments, detection of 100% of the Ag present in the AgNPs would correspond to 26.7 μC. However, the experimental results indicate that just 5% of this charge is recovered after two GE cycles. This low collection efficiency must, therefore, be attributed to the Au shell (Figure 2.11) that forms during the initial stages of GE. A rough calculation based on data like that shown in Figure 2.11 suggests that ~85% of the total Ag present in the system is within the core of the Ag@Au NPs that form during GE. The remainder of uncollected Ag (~15%) is likely present as AgCl that is not in direct contact with the electrode surface.

2.4.6 Electrochemical detection of different AgNP concentrations

Up to this point, we have only reported results for a single, average number density of AgNPs on the MμB-AgNP conjugates. Because we wish to use AgNPs as labels in bioassays, we now turn our attention to correlating the electrochemical charge recovery to the concentration of AgNPs used to prepare the conjugates.

This provides a good model for understanding the dynamic range of this detection method. These experiments were carried out as described for the two-cycle histogram shown in Figure 2.17, except for one minor change: Ag-oxidation voltammograms were obtained only after both GE cycles were complete, whereas voltammograms were obtained after each of the three cycles in Figure 2.17.

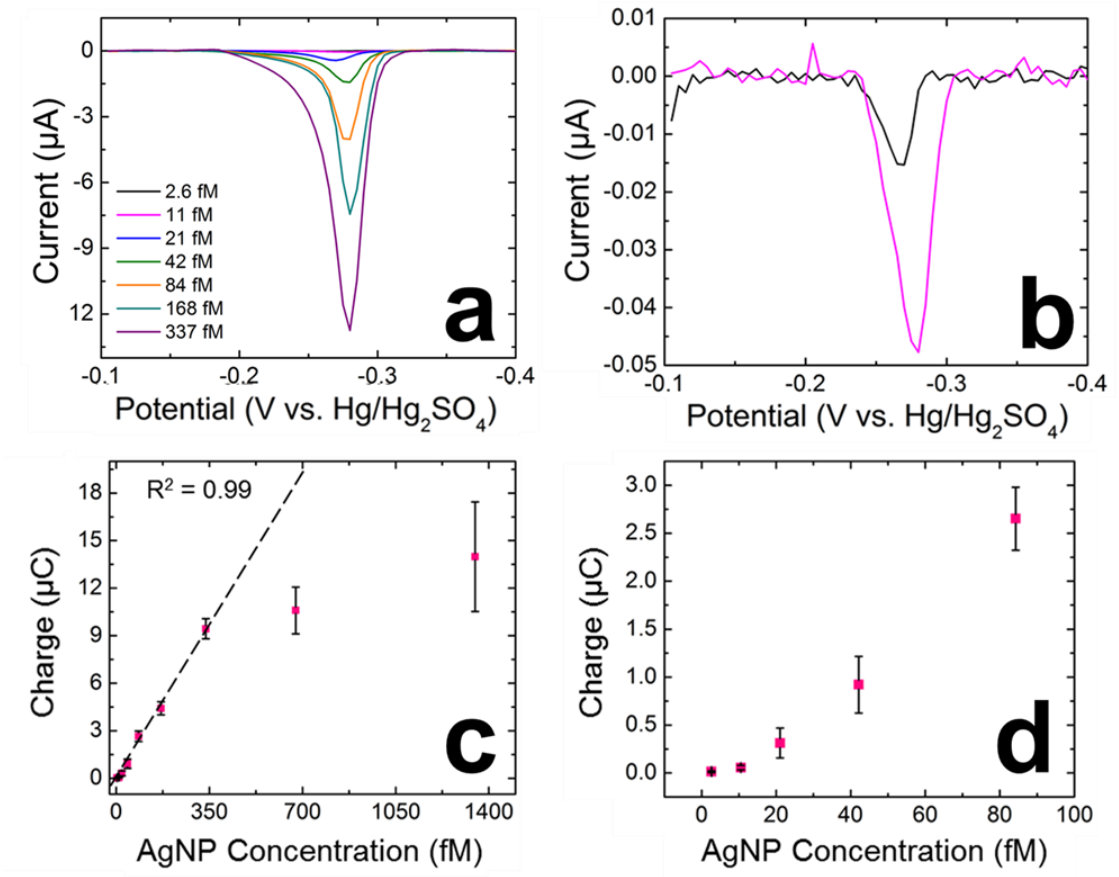

Figure 2.18 (a) Anodic stripping voltammograms (ASVs) obtained by drying the MμB-AgNP conjugates onto the carbon/Au working electrode, rehydrating in 150 μL BCl, and then carrying out the ASV protocol described in the text. The concentrations listed in the legend represent the total concentration of AgNPs in the 150 μL volume. The scan rate was 50 mV/s. (b) Expanded view of the ASVs for the lowest two AgNP concentrations in (a). (c) Plot of charge, determined by integrating the ASVs in (a), as a function of AgNP concentration. Each data point represents five replicate measurements obtained using independently prepared electrodes. Outliers were eliminated using the Grubb's Test with a 95% confidence level.[102] (d) Expanded view of the linear range in (c). The lowest detectable concentration is 2.6 fM AgNPs.

The voltammograms in Figure 2.18a indicate that the Ag stripping current increases as a function of the concentration of the AgNPs. The concentrations listed in the legend of Figure 2.18a represent the moles of AgNPs dried at the working electrode and rehydrated in 150 µL BCl. The voltammograms for the two lowest concentrations are expanded in Figure 2.18b. Note that concentrations below 2.6 fM could not be differentiated from the baseline. The charges under voltammograms like that shown in Figure 2.18a were obtained by integration, and the results for five independent experiments per concentration are plotted in Figure 2.18c. These data show that the charge increases linearly from 2.6 fM to 337.0 fM AgNPs, and then it begins to saturate. The lower end of the linear range is shown on an expanded scale in Figure 2.18d. The point is that by understanding and optimizing this detection system, it has been possible to obtain a very low detection limit and a respectable linear range (two orders of magnitude).

2.5 Summary and Conclusion

To summarize, we have investigated the seemingly simple process of GE between $AuCl_4^-$ and AgNPs conjugated to MµBs in Cl^--containing buffer. The study was carried out to develop a better understanding of (and hence improve) an electrochemical

detection modality that we recently reported.[59,66] The simplistic view of the detection system is summarized in Illustration 2.1, but after analysis of both SEM and TEM micrographs, we found that the reality of the situation is quite a bit more complicated. For example, each AgNP label undergoes only partial GE due to formation of a ~10 nm Au shell that shields the remaining Ag that ends up in the core of the NP. The formation of this core@shell structure is a consequence of the rather large AgNPs (110 nm) that were used in this study (to facilitate structure determination). Because the Au shell is 10 nm thick, however, it is likely that 20 nm AgNPs will undergo complete GE. Therefore, in forthcoming biosensing applications, we plan to use AgNP labels in the 20 nm size range.

We also discovered that only about half the AgNPs undergo any detectable level of GE after one cycle, but that two GE cycles results in partial GE of essentially all AgNPs originally present. This, we believe, is a consequence of precipitation of AgCl, which prevents cross-reaction between $AuCl_4^-$ and AgNPs.

Finally, we established that this basic GE-based detection of AgNPs is both quantitative and sensitive. The relevant metrics for biosensing detections are a 2.6 fM AgNP detection limit, and a linear range that spans two orders of magnitude. We are presently working on a metalloimmunoassay using this

detection strategy and a paper fluidic platform.[6,67,69] The results of those experiments will be reported in due course.

Chapter 3: Orientation-Controlled Bioconjugate of Antibodies to Silver Nanoparticles

3.1 Synopsis

Here we report on the use of heterobifunctional cross-linkers (HBCLs) to control the number, orientation, and activity of immunoglobulin G antibodies (Abs) conjugated to silver nanoparticles (AgNPs). A hydrazone conjugation method resulted in exclusive modification of the polysaccharide chains present on the fragment crystallizable region of the Abs, leaving the antigen-binding region accessible. Two HBCLs, each having a hydrazide terminal group, were synthesized and tested for effectiveness. The two HBCLs differed in two respects, however: (1) either a thiol or a dithiolane group was used for attachment to the AgNP; and (2) the spacer arm was either a PEG chain or an alkyl chain. Both cross-linkers immobilized 5 ± 1 Abs on the surface of each 20 nm-diameter AgNP. Electrochemical results, obtained using a half-metalloimmunoassay, proved that Abs conjugated to AgNPs *via* either of the two HBCLs were 4 times more active than those conjugated by the more common physisorption technique. This finding confirmed that the HBCLs exerted orientational control over the Abs. We also demonstrated that the AgNP-HBCL-Ab conjugates were stable and active for at least two weeks. Finally, we found that the stability of the

HBCLs themselves was related to the nature of their spacer arms. Specifically, the results showed that the HBCL having the alkyl chain is chemically stable for at least 90 days, making it the preferred cross-linker for bioassays.*

*Chapter 3 is based on a previous publication: N. E. Pollok, C. Rabin, L. Smith, R. M. Crooks, Orientation-Controlled Bioconjugation of Antibodies to Silver Nanoparticles. *Bioconjugate Chem*. 2019, 30, 3078-3086. NEP and CR contributed equally to the work. LS collected experimental data. RMC was the research advisor. NEP and CR designed and performed the experiments. NEP, CR, and RMC wrote the manuscript.

3.2 Introduction

In this chapter we demonstrate the use of heterobifunctional cross-linkers (HBCLs) to control the number and orientation of immunoglobulin G antibodies (Abs) conjugated to silver nanoparticles (AgNPs). Specifically, two HBCLs were synthesized, each bearing: (1) a hydrazide group for the specific targeting of the fragment crystallizable (Fc) region of Abs,[104–107] (2) a thiol group for anchoring the HBCL to the AgNP,[106,108–111] and (3) a tunable spacer arm to enhance the biocompatibility[104] of the NP-Ab conjugates. The key finding is that HBCLs improve the activity of the Abs on AgNPs by controlling their orientation compared to the more common physisorption method in which Abs are randomly arranged electrostatically in multi-layers.[104,112] Because AgNPs have become increasingly important as labels for bioassays[113,114] in recent years, and because there are few prior reports relating to controlled-Ab immobilization on AgNPs,[9,13] the present study is timely and relevant.

While Au and Ag are both noble metals, Au has a significantly higher standard potential (E^0 = 1.52 V) than Ag (E^0 = 0.79 V).[65] The increased stability of AuNPs relative to AgNPs makes them a prime candidate for bioconjugation applications. Indeed, there are numerous reports of Ab immobilization on AuNPs.[11,106,115,117] In recent years, however, AgNPs have been shown

to have optical[113,114,118,119] and biological[118,120,121] properties that can be beneficial to the development of a new category of molecular probes. For example, our group has used AgNPs as a signal amplifying label for detecting Abs in metalloimmunoassays,[57,58,61] including for electrochemical detection of the heart-failure biomarker, N-terminal prohormone brain natriuretic peptide (NT-proBNP).[59] In this specific metalloimmunoassay, simple physisorption was used to conjugate the detection Abs to the AgNP labels. The detection limit and reproducibility of this approach were not satisfactory, however, and therefore we sought an alternative immobilization method.

Physisorption of Abs to metal NPs relies primarily on interactions between the NP surface and amine or thiol residues present on the Abs.[104,122] While this approach for bioconjugation is fast and easy, it has four important limitations: (1) it requires a large excess of Abs;[104,105,121] (2) the Ab coverage on the NP surface is not well-controlled;[104] (3) the stability of the conjugate is poor due to weak electrostatic interactions;[115,123,124] and (4) the lack of control over the orientation of the Abs reduces access of the target to the antigen-binding sites (Fab).[104,115] For AuNPs, these points have been addressed by using HBCLs comprised of a thiol group at one end and a Fc region-conjugated Ab on the other. Like Au,[107,125,126]

Ag can also form dative bonds with thiol functional groups,[67,111-114,131-134] which provides a means for forming a stable bond between the Ag surface and the Fc region of the Abs.

As mentioned earlier, the majority of reports pertaining to Ab immobilization on AgNPs does not rely on a controlled immobilization method. For example, in 2007 Huang et al. used the affinity of thiols for AgNPs to link Abs to AgNPs *via* HBCLs.[129] Specifically, they attached thiolated HBCLs to the surface of AgNPs, and then activated the carboxylic acid group at the distal end of the HBCLs using 1-ethyl-3-(3-dimethylaminopropyl)carbodiimide. Exposure of these functionalized AgNPs to Abs resulted in a reaction between the activated acids and primary amines present on the latter. A related approach has also been reported in which activated carboxylic acids present on the Abs were reacted with thiol/amine HBCLs pre-attached to AgNPs.[105]

Both of the foregoing approaches rely on the position of accessible amine or carboxylic acid groups within the Ab structure, which is strongly dependent of the Ab sequence. The main drawback of targeting amine and carboxylic acid groups is, therefore, the lack of control over the distribution of the functional groups on the Ab. Indeed, charged residues (NH_3^+ and COO^-) are randomly distributed in the Ab amino acid sequence.

Moreover, targeting amine groups has an even more deleterious effect upon binding activity of Abs because the N-terminus is located within the Fab region.[104,112,130,131] This potentially puts the active site of the Ab in danger of being damaged or misoriented on the surface of the NPs. In these cases, like in the physisorption method, control over the orientation is not achieved.

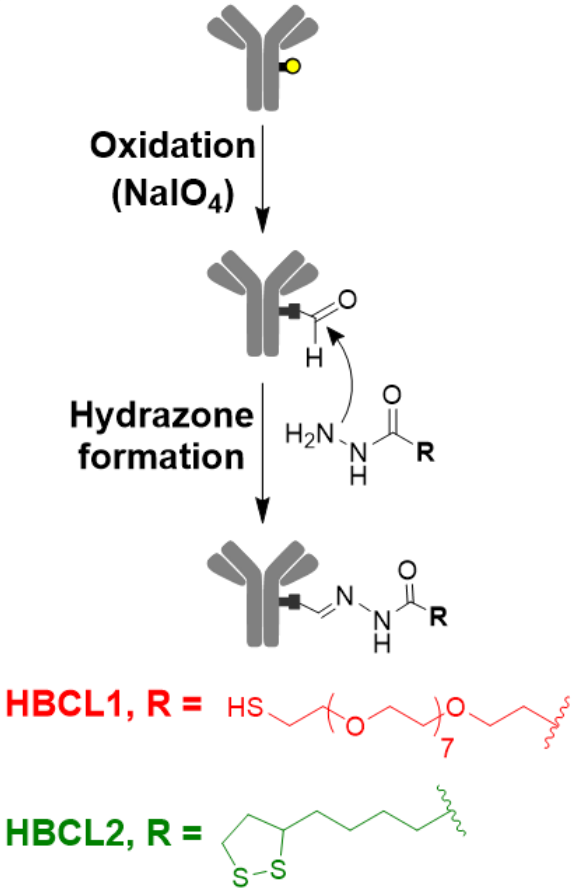

Illustration 3.1 Scheme of the hydrazide chemistry.

To overcome some of the deficiencies of these earlier approaches, we focused on controlling the orientation of the Abs to allow the Fab regions to be more accessible to antigens in solution while still maintaining a robust AgNP-Ab interaction. This can be done by targeting either the C-terminus of the Ab or the polysaccharide chains sequestered in the Fc region.[104,105,132] The C-terminus is generally recognized by specific protein/protein interactions with protein G[112,116] or protein A,[115] but in both cases this is a reversible binding event.[112,133] In contrast, the polysaccharide chains can either be targeted directly with boronic acid residues,[105,134,135] or by following a mild oxidation step coupled with a hydrazide addition.[104,131] Because the boronic-polysaccharide complex is known to be unstable at physiological pH,[135] we elected to use the hydrazone chemistry. Illustration 3.1 depicts the hydrazone method, in which the polysaccharide chains of the Ab are first converted to aldehyde groups with a mild oxidant, and then coupled to hydrazide-functionalized HBCLs. Note that a similar approach was reported by Kumar *et al.* in 2008 for AuNPs, and as we will show later AgNPs are as biocompatible as AuNPs using this approach.[106]

In the present chapter, two HBCLs differing in spacer arm composition (PEG or alkyl chains) and sulfur group (thiol or dithiolane) were synthesized and used to conjugate Abs to 20 nm

AgNPs (Illustration 3.1). The same chemistry was carried out using AuNPs as a benchmark for comparison. The present study shows that: (1) a HBCL-mediated bioconjugation method can be used to efficiently functionalize AgNPs; (2) NPs can be functionalized with reproducible numbers of Abs; (3) HBCLs lead to Ab orientation on NP surfaces that results in improved binding of targets compared to physisorption; and (4) the binding efficiency to the target is constant over at least a two-week period for AgNP-HBCL-Ab conjugates, which is not the case for physisorbed conjugates.

3.3 Experimental

3.3.1 Chemicals and Materials

All solutions were prepared using deionized (DI) water (>18.0 MΩ-cm, Milli-Q Gradient System, Millipore, Burlington, MA). Tetrahydrofuran (THF) anhydrous, hydrazine monohydrate, hydrazine solution 1 M in THF, (±)-α-lipoic acid, methanol, dimethyl sulfoxide (DMSO) and DMSO-d_6 were purchased from Sigma-Aldrich (Milwaukee, WI). 4-Amino-3-hydrazino-5-mercapto-1,2,4-triazole (Purpald), H_2SO_4, $KMnO_4$, toluene, phosphate buffered saline (PBS) pH 7.4 (P3813), casein, superblock blocking buffer (SBB) (37515), siliconized low-retention microcentrifuge tubes, Whatman grade 1 chromatography paper (180 μm thick, 20 cm × 20 cm

sheets, linear flow rate of water = 0.43 cm/min), and Costar 3590 high-binding microtiter plates were purchased from Fisher Scientific (Pittsburgh, PA).

All PBS used was 1x concentration PBS. SH-PEG_7-COOH was obtained from Polypure (Oslo, Norway). mPEG-SH 5 kDa was obtained from Nanocs (New York, NY). 1-Step Ultra TMB-ELISA Substrate Solution (34028) and sodium meta-periodate ($NaIO_4$) were obtained from Thermo Scientific (Grand Island, NY). Citrate-capped AgNPs and AuNPs (nominal 20 nm diameter) were purchased from nanoComposix (San Diego, CA). N-terminal prohormone brain natriuretic peptide (NT-proBNP) and monoclonal immunoglobulin G anti-NT-proBNP 13G12 (Ab) were obtained from HyTest (Turku, Finland). Polyclonal anti-mouse immunoglobulin G horseradish peroxidase-labeled secondary antibody (SAb) was obtained from Abcam (Cambridge, UK). Amicon ultra 0.5 mL centrifugal filters (10 K) were purchased from Millipore Sigma (Tauton, MA). Conductive carbon paste (Cl-2042) was purchased from Engineered Conductive Materials (Delaware, OH). All chemicals and reagents were used without further purification unless otherwise specified.

3.3.2 Instrumentation

^{1}H and ^{13}C NMR spectra were recorded with a Varian MR 400 MHz spectrometer while 2D NMR spectra (COSY $^{1}H/^{1}H$ and HSQC $^{1}H/^{13}C$)

were recorded with an Agilent MR 400 MHz spectrometer. All spectra were measured using $DMSO_{d6}$ as the solvent. Multiplicities are reported as follows: s=singlet, t=triplet, m=multiplet. Chemical shifts are reported in δ units to 0.01 ppm precision for ^{1}H and 0.1 ppm for ^{13}C by using residual solvent as an internal reference.

Absorbance measurements were obtained and pathlength corrected using a Synergy H4 Hybrid Multi-Mode Microplate Reader from BioTek (Winooshi, VT). A Sorvall Legend Micro 21R Centrifuge from Thermo Scientific was used for washing and separation steps during bioconjugation. A Mini Vortexer 945300 from VWR International (Radnor, PA) was used to briefly mix solutions while a BioShake iQ from Quantifoil Instruments GmbH (Jena, Germany) was used for incubation steps during bioconjugation. Before analysis with the microplate reader, a centrifuge 5810 R from Eppendorf (Hamburg, Germany) was used to remove bubbles from the wells.

3.3.3 Electrochemistry

All electrochemical measurements were performed using a CH Instruments model 760B electrochemical workstation (Austin, TX), and a slightly modified, previously published protocol.[127] Specifically, all electrochemical materials, the working, counter, and quasi-reference electrodes were fabricated by

stencil-printing carbon paste onto wax-patterned sheets of chromatography paper that had been printed using a Xerox ColorQube 8570DN printer. Following printing, the wax was melted through the thickness of the paper by placing it in an oven at 120 °C for 25.0 s. Photopaper was glued to the back of the wax printed chromatography paper for rigidity, and then it was cut into 12 rectangles (2.0 cm × 5.0 cm). A stencil for defining the 3.0 mm-diameter disk-shaped working electrode, hook-shaped carbon quasi-reference electrode, and counter electrode was created using CorelDRAW (Ottawa, ON). The stencil was cut into a thin plastic sheet of transparency film using an Epilog laser engraving system (Zing 16). Finally, the stencil was placed over the paper (wax side up), the electrodes were printed through the stencil using conductive carbon paste, and then the carbon paste was left to dry in air for 14 h (Illustration 3.2).

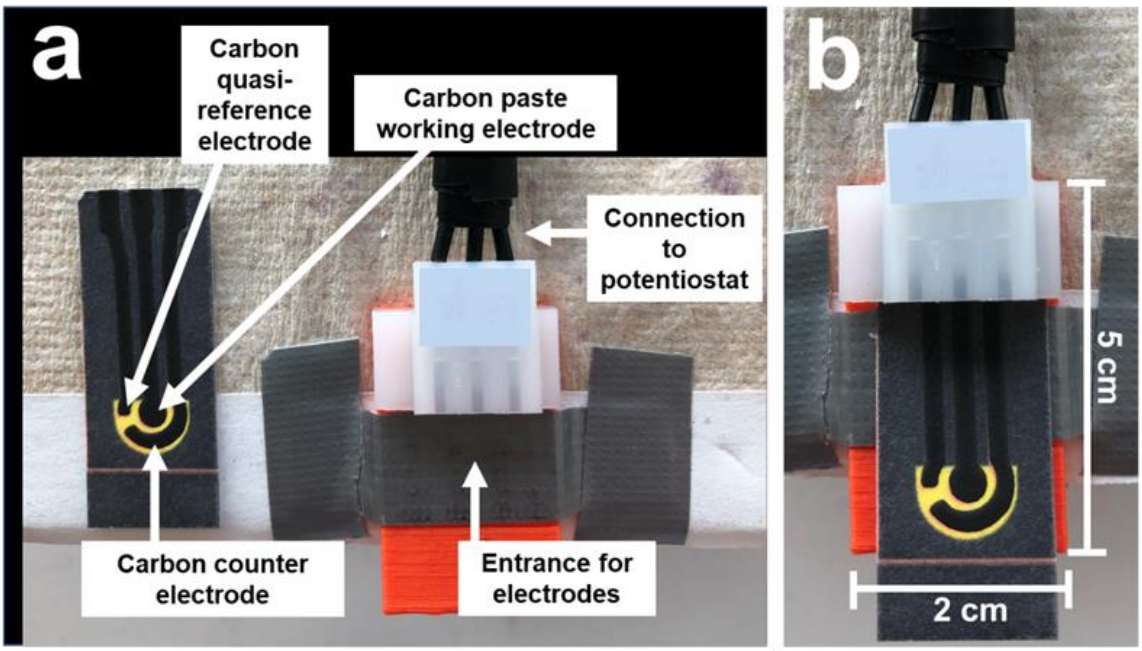

Illustration 3.2 Description of the electrochemical cell used for determining the activity of the Abs on the conjugates. Ag electrodeposition and anodic stripping voltammetry (ASV) were performed with this device. (a) Photograph of the electrodes and the electrochemical cell. (b) Photograph of the assembled cell. The white portion of the electrochemical cell incorporates metal prongs within the enclosure to provide ohmic contact between the carbon paste electrodes and the potentiostat. Duct tape is placed across the orange platform of the cell to keep it stable during analysis. The electrodes were stencil printed with conductive carbon paste, as mentioned in the Experimental Section of Chapter 3. The regions printed in yellow wax are slightly more hydrophilic compared to the black wax regions, allowing for the sample solution to span all three carbon electrodes. The yellow region can hold an aqueous volume of 50-80 µL. In the present chapter, 76 µL of sample solution were added to the electrode region.

3.3.4 Synthesis of HBCL1

To a solution of SH-PEG_7-COOH (108 mg, 0.24 mmol) in methanol (2.00 mL) was slowly added a solution of hydrazine hydrate (1.40 mL) in methanol (1.00 mL). The reaction medium was stirred for 24 h at room temperature (RT) (22 ± 3 °C). The solvent was then co-evaporated with toluene under reduced pressure to yield HBCL1 as a yellowish oil (113 mg, 100%). ^{1}H NMR (400 MHz, $DMSO_{d6}$), δ (ppm): 3.64 (t, *J* = 6.5 Hz, 2H, **Hb**), 3.57 (t, *J* = 6.7 Hz, 2H, **Hd**), 3.51 (s, 28H, **Hc**), 2.89 (t, *J* = 6.4 Hz, 2H, **Ha**), 2.34 (t, *J* = 6.7 Hz, 2H, **He**). ^{13}C NMR (400 MHz, $DMSO_{d6}$), δ (ppm): 173.7 (C_q, **Ch**), 69.8 (CH_2, **Cd**), 69.6 (CH_2, **Ce**), 69.5 (CH_2, **Cc**), 68.6 (CH_2, **Cb**), 67.3 (CH_2, **Cf**), 37.9 (CH_2, **Ca**), 36.3 (CH_2, **Cg**). 2D NMR: COSY (^{1}H/^{1}H), HSQC (^{1}H/^{13}C). NMR spectra can be found in Figures 3.1 and 3.2.

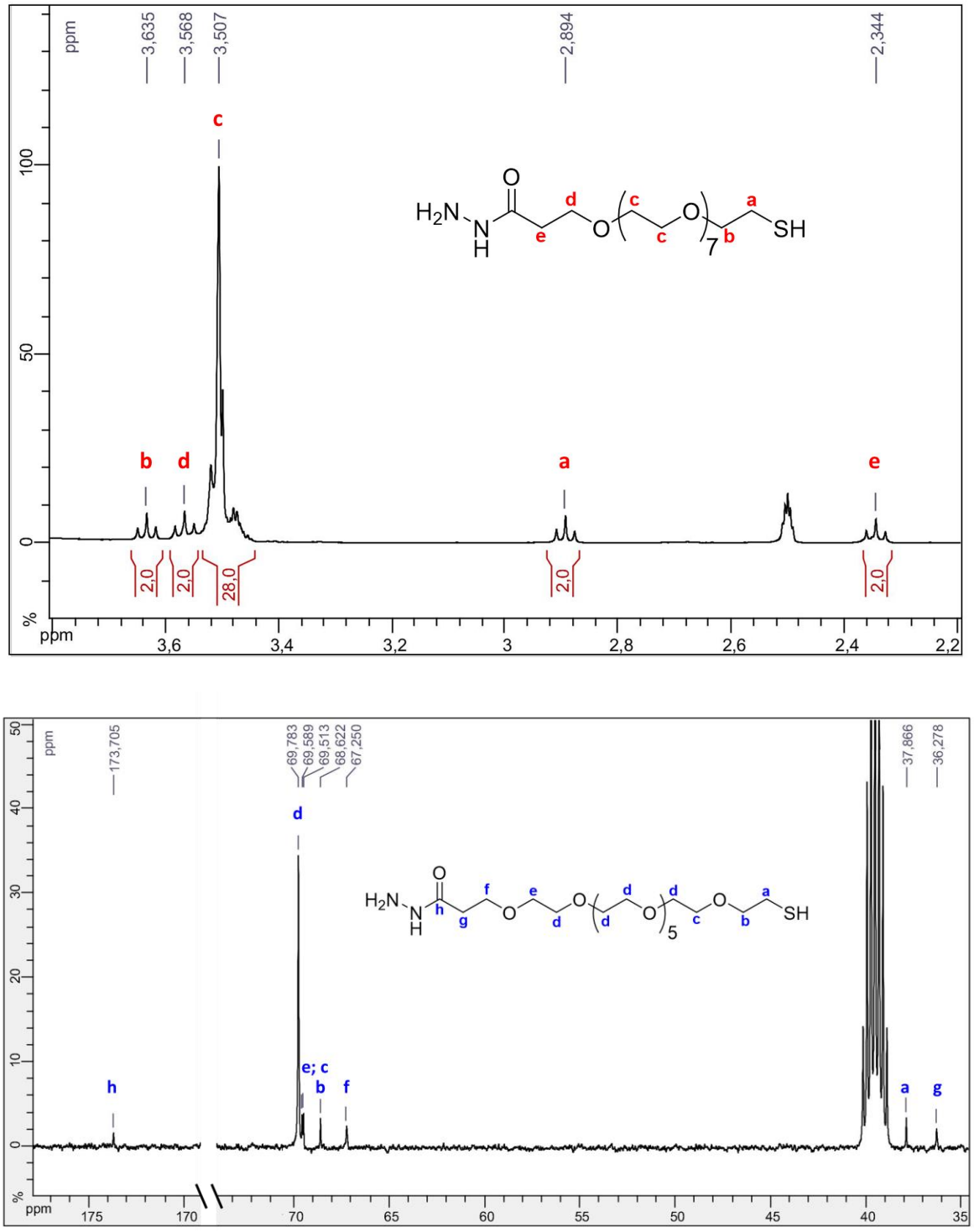

Figure 3.1 (top) ^{1}H NMR (400 MHz, $DMSO_{d6}$) and (bottom) ^{13}C NMR (400 MHz, $DMSO_{d6}$) spectra of heterobifunctional cross-linker 1 (HBCL1).

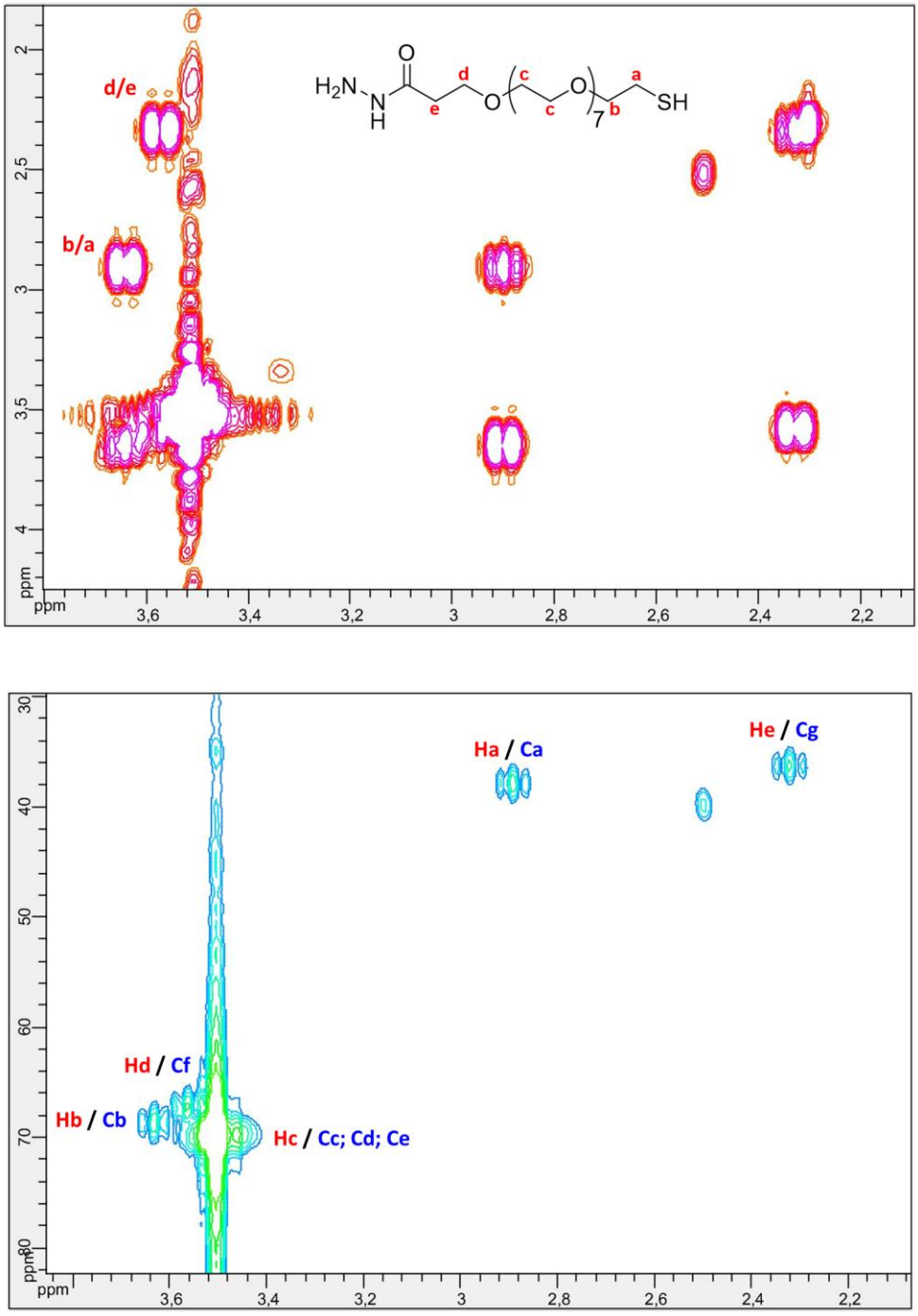

Figure 3.2 (top) COSY ($^{1}H/^{1}H$) 2D NMR (400 MHz, $DMSO_{d6}$) and (bottom) HSQC ($^{1}H/^{13}C$) 2D NMR (400 MHz, $DMSO_{d6}$) correlations for HBCL1.

3.3.5 Synthesis of HBCL2

To a solution of (±)-α-lipoic acid (50 mg, 0.24 mmol) in anhydrous THF (3.00 mL) at 0 °C was slowly added a solution of hydrazine hydrate in THF (0.34 mL, 1 M). The reaction medium was stirred for 90 min at 0 °C. The solvent was then evaporated under reduced pressure below 30 °C to yield HBCL2 as a white solid (40 mg, 76%). ^{1}H NMR (400 MHz, $DMSO_{d6}$), δ (ppm): 3.59 (hidden, determined by 2D NMR) (m, 2H, **Hc**), 3.12 (m, 2H, **Ha**), 2.40 (m, 1H, **Hb**), 2.10 (t, *J* = 7.1 Hz, 2H, **Hg**), 1.86 (m, 1H, **Hb'**), 1.65 (m, 1H, **Hd**), 1.52 (m, 1H, **Hd'**), 1.48 (m, 2H, **Hf**), 1.35 (m, 2H, **He**). ^{13}C NMR (400 MHz, $DMSO_{d6}$), δ (ppm): 175.2 (C_q, **Ch**), 56.5 (CH, **Cc**), 40.1 (hidden, determined by 2D NMR) (CH_2, **Cb**), 38.5 (CH_2, **Ca**), 34.4 (CH_2, **Cg**), 34.1 (CH_2, **Cd**), 28.6 (CH_2, **Ce**), 24.7 (CH_2, **Cf**). 2D NMR: COSY (^{1}H/^{1}H), HSQC (^{1}H/^{13}C). NMR spectra can be found in Figures 3.3 and 3.4.

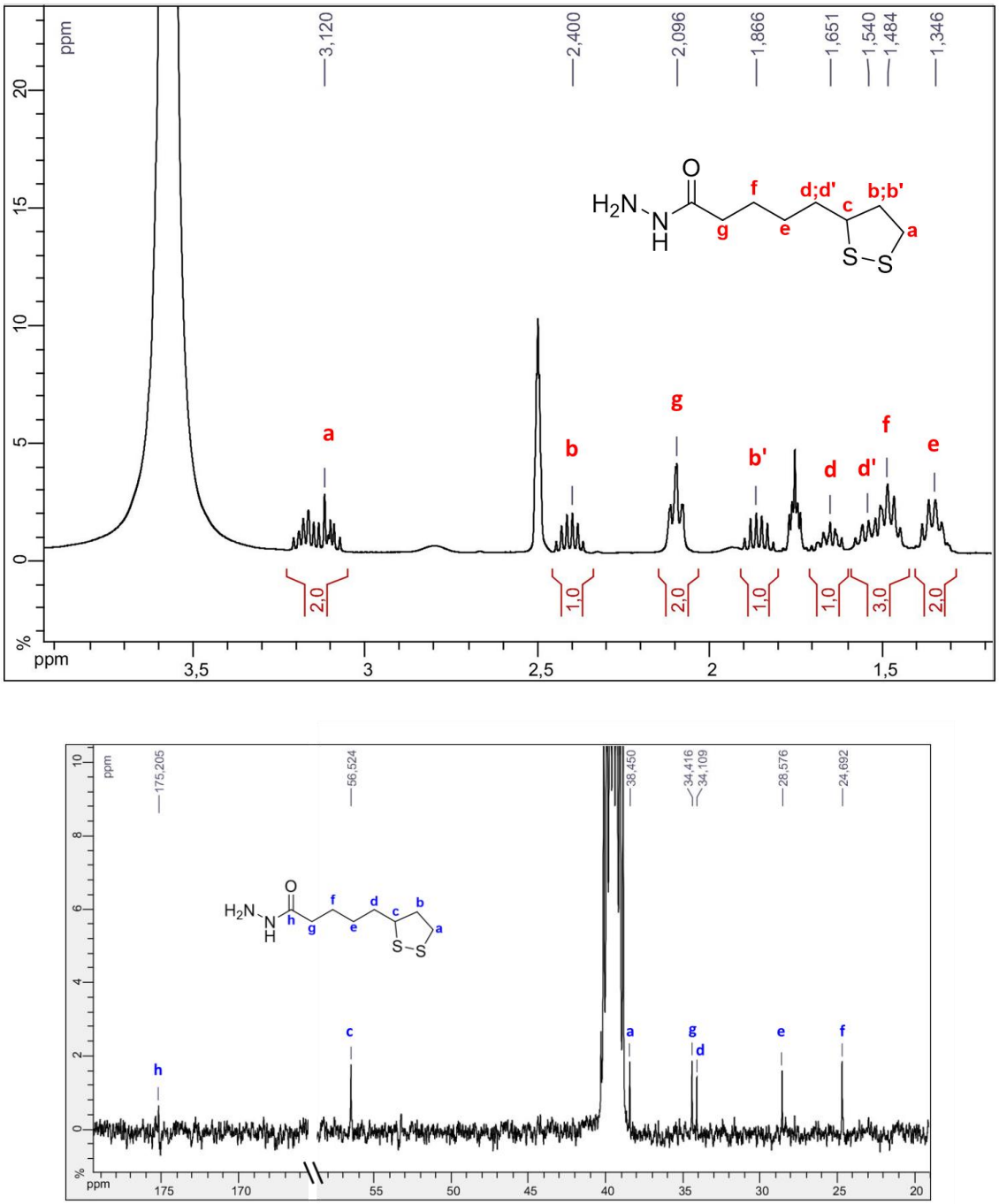

Figure 3.3 (top) ^{1}H NMR (400 MHz, $DMSO_{d6}$) and (bottom) ^{13}C NMR (400 MHz, $DMSO_{d6}$) spectra of HBCL2. Note, the spectra of HBCL2 for day 90 are identical and therefore not shown.

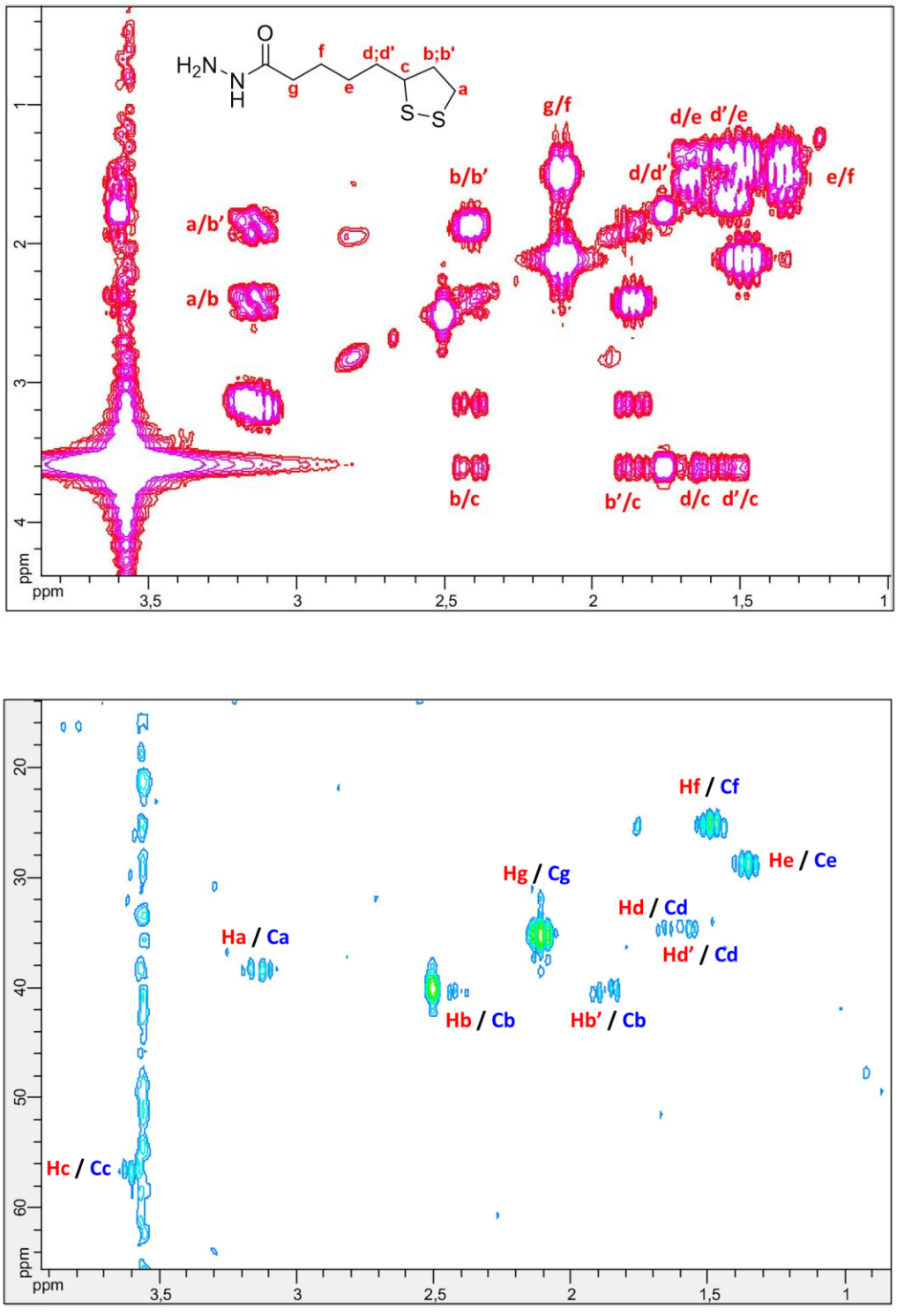

Figure 3.4 (top) COSY ($^{1}H/^{1}H$) 2D NMR (400 MHz, $DMSO_{d6}$) and (bottom) HSQC ($^{1}H/^{13}C$) 2D NMR (400 MHz, $DMSO_{d6}$) correlations of HBCL2.

3.3.6 Conjugating Abs to NPs

Unless stated otherwise, all incubation steps were performed at RT at 600 rpm. To start, 5.0 µL of 6.7 µM Ab were incubated with 5.0 µL of 50 mM $NaIO_4$ for 30 min in the dark to oxidize the polysaccharide chains on the Fc region of the Ab (Figure 3.5).

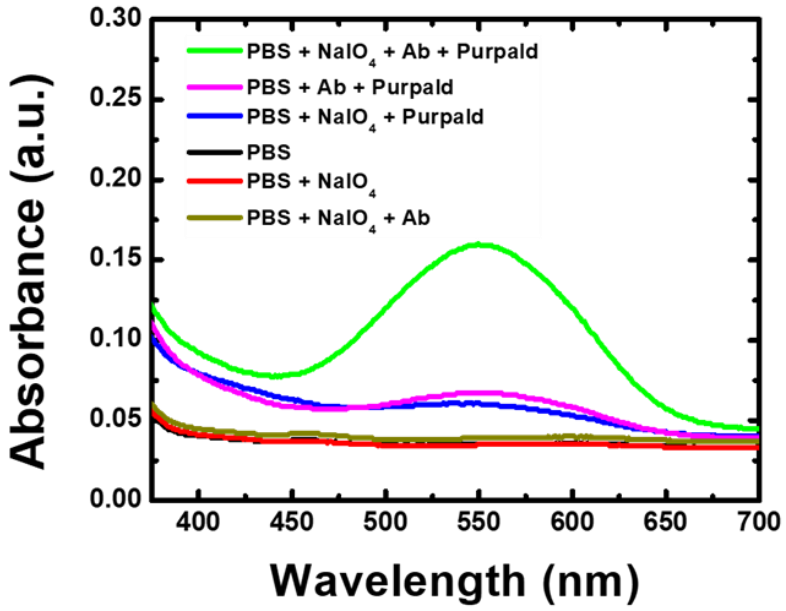

Figure 3.5 Colorimetric determination of polysaccharide chain content of 13G12 anti-N-terminal prohormone brain natriuretic peptide antibody (Ab) by UV-vis spectroscopy using 4-amino-3-hydrazino-5-mercapto-1,2,4-triazole (Purpald). This experiment was carried out by adding 4 µL of 5.4 µM Ab to 4 µL of 50 mM $NaIO_4$, incubating the mixture in the dark for 30 min at 22 ± 3 °C, and agitating at 600 rpm to oxidize the polysaccharide chains of the Ab. Oxidation was quenched by adding 100 µL of 1xPBS. 75 µL of a freshly prepared 68.4 mM solution of Purpald in 1 M NaOH were then added to the wells of a microtiter plate immediately prior to spectrophotometric analysis. The solution was monitored at 550 nm, which is characteristic of the Purpald hydrazone product resulting from the reaction between the oxidized polysaccharide chains of the Ab and Purpald. The spectrum corresponding to this experiment was recorded, and an absorbance intensity of ~0.15 a.u. was obtained (green spectrum), confirming the presence of the polysaccharide chains on the Ab. Several controls were also performed to ensure that the absorbance intensity at 550 nm was only due to the hydrazone formation. The black, red, and brown spectra were recorded without Purpald, and as expected there is no elevation in the baseline. The pink spectrum corresponds to Purpald in the presence of non-oxidized Ab, and it shows a slight increase in the baseline at 550 nm due to the background of Purpald degradation.[106] The blue spectrum corresponds to Purpald in presence of $NaIO_4$ and here again only the background signal of the degradation of Purpald is observed.

The oxidation reaction was quenched with 125 µL of PBS. The oxidized Abs were then incubated with 5.0 µL of 5.0 mM of the desired HBCL solution for 2 h. HBCL1 was directly dissolved in DI water to give the desired concentration, while HBCL2 was first dissolved in DMSO and then diluted in DI water. The solution was transferred to an Amicon ultra 0.5 mL centrifugal filter (10 K) and was centrifuged for 25 min at 4 °C at 14,000 g.

The HBCL-modified Abs were then incubated with 500 µL of the desired NP solution (4.9×10^{11} AgNPs/mL or 7.4×10^{11} AuNPs/mL) for 1 h. In this step, the microcentrifuge tubes were pre-blocked with SBB to prevent non-specific binding of Abs and NPs on the walls of the tubes. These tubes were covered with aluminum foil to protect the NPs from light. Following incubation, 50 µL of 10.0 µM mPEG-SH were added and incubated for another 20 min. Finally, three centrifugation (25 min, 4 °C, 16,600 g) steps were performed to remove unbound material, followed by resuspension into 500 µL SBB. The percentage yields of NPs after functionalization can be found in Figure 3.6.

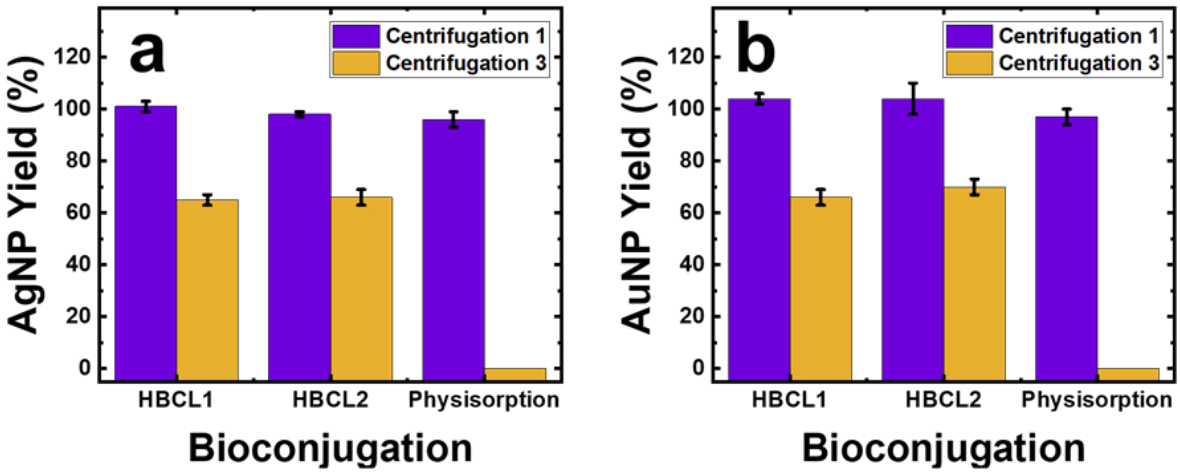

Figure 3.6 Histograms showing the percentage yield of (a) the AgNPs and (b) the AuNPs, after functionalization with Ab-HBCL1, Ab-HBCL2 and unmodified Abs. This experiment was carried out as follows. First, the absorbance intensity at λ_{max} was measured for each conjugate (*i.e.* NP-HBCL1-Ab, NP-HBCL2-Ab and physisorbed conjugates). Second, the absorbance value was converted to a NP concentration (NPs/mL) using the calibration curve shown in Figure 3.8. Third, this concentration was divided by the concentration of NPs before bioconjugation and was multiplied by 100. For all conjugates, the yields reflect those after the first (blue) and second (orange) centrifugation (conditions: 25 min, 4 ˚C, 16,600 g). The absorbance at λ_{max} is directly correlated to the number of NPs in solution, and a decrease is usually representative of NP aggregation.[136] Therefore, this analysis provides a means for determining the extent of NP aggregation that results after Ab conjugation. The data indicates that almost no aggregation of the conjugates occurs after the first centrifugation. In contrast, the NP-Ab conjugates aggregate significantly after the third centrifugation. Note that, the physisorbed conjugates aggregate completely under the same conditions.

Henceforth, the product of bioconjugation will be referred to as NP-HBCL-Ab conjugates (AgNP-HBCL-Ab when referring to Ag and AuNP-HBCL-Ab when referring to Au). The protocol for making the samples with physisorbed Abs can be found in the Appendix (A2).

3.3.7 Quantifying the total number of Abs per NP

The number of Abs per NP was determined using an indirect enzyme-linked immunosorbent assay (ELISA) with a SAb. Unless stated otherwise, all incubation steps were performed for 30 min at RT at 600 rpm and were followed by three washing steps with PBS. Briefly, 100 µL of 58.2 nM NT-proBNP in PBS were incubated for 14 h at 4 °C without shaking in a high-binding microtiter plate. Then, 400 µL of 2% (w/v) casein solution in PBS were added to block the wells for 30 min without shaking. Wells used for the calibration curve (Figure 3.7) were incubated with various known concentrations of unmodified Abs, while test wells were incubated with the supernatant obtained after the first centrifugation (containing unbound Abs).

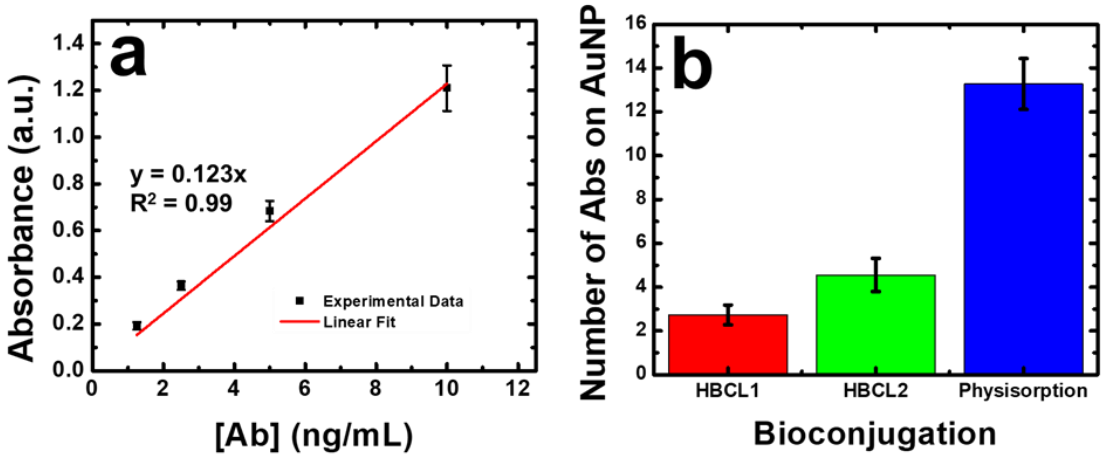

Figure 3.7 UV-Vis spectrophotometric data collected at 450 nm in triplicate using an indirect enzyme-linked immunosorbent assay (ELISA) to determine the number of Abs per AuNP. (a) Calibration curve obtained via indirect ELISA of unmodified Abs. (b) Histogram showing the number of Abs bound per AuNP, which was determined by performing an indirect ELISA with the supernatant of the first washing step (first centrifugation) following bioconjugation of Abs to AgNPs. The complete procedure for this experiment is described in the Experimental Section.

Next, 100 µL of 6.7 µM SAb were added to each well and incubated. Finally, 100 µL of the 1-Step Ultra TMB solution were added and 50.0 µL of 2 M H_2SO_4 were used to quench the reaction after it reached the desired color intensity (~3 min). The number of Abs in the conjugates was obtained by subtracting the Ab content remaining in the supernatant after bioconjugation from the initial Ab solution. This value was divided by the number of NPs, which was determined with a calibration curve that can be found in Figure 3.8.

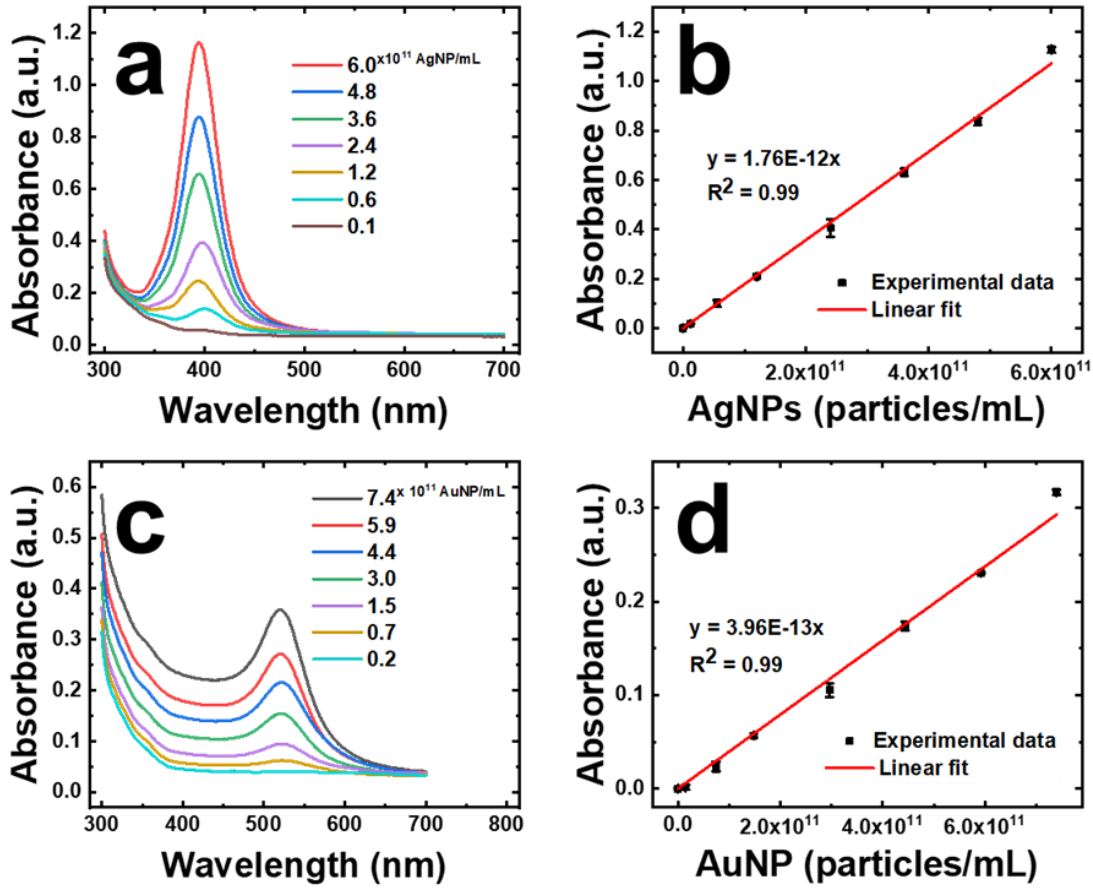

Figure 3.8 UV-Vis calibration data for quantification of Ag and Au NPs. (a) UV-Vis spectra of decreasing concentrations of AgNP. (b) AgNP calibration curve generated from the absorbance values at 395 nm. (c) UV-Vis spectra of decreasing concentrations of AuNP. (d) AuNP calibration curve generated from the absorbance values at 520 nm. These experiments were performed by diluting the stock solution of 20 nm-diameter, citrate-capped AgNPs and AuNPs with deionized water. 100 µL of each solution were added to the wells of a microtiter plate and the absorbance spectra were recorded. The error bars represent the standard deviation from the mean for three independent experiments.

3.3.8 Monitoring the Ab activity of the conjugates

The activity of the Abs on the AgNPs was determined electrochemically by forming a half-metalloimmunoassay, wherein the AgNPs were used as the detection label and the target was bound to a well. Unless stated otherwise, all steps were performed at RT at 600 rpm. Briefly, 100 µL of 0.60 µM of NT-proBNP were bound to the wells of a high-binding microtiter plate for 14 h at 4 °C. After coating the wells, the plate was washed three times with PBS and blocked with SBB for 30 min without shaking. Next, 100 µL of the conjugates were added to each well, incubated for 30 min, and washed with PBS.

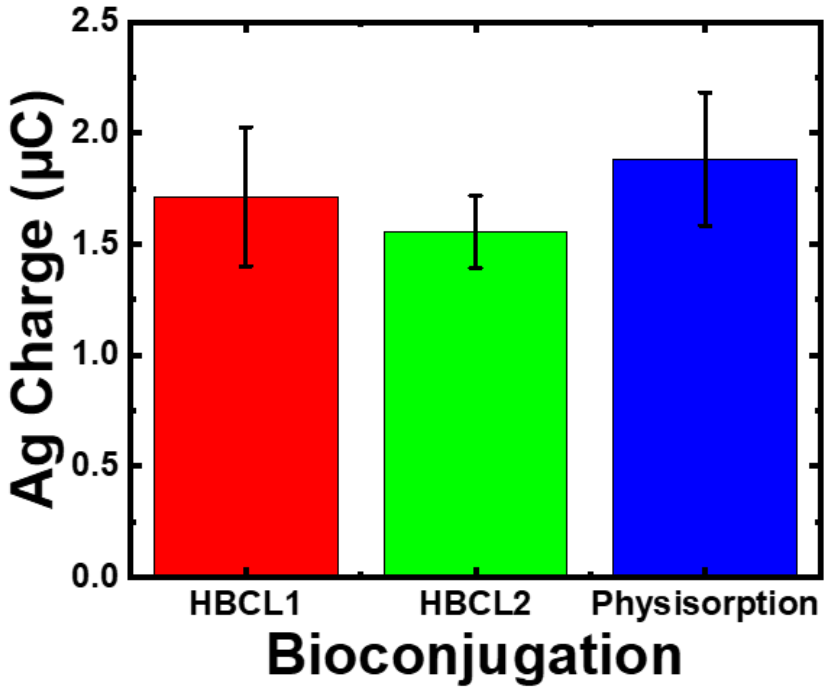

Figure 3.9 Ag charge obtained for the conjugates in solution following electrochemical analysis. This experiment was performed by freshly preparing the conjugates, diluting them all to the same 0.23 µM AgNP concentration, incubating with 30 µL of 0.20 mM $KMnO_4$ for 15 min, and then carrying out the electrochemical protocol described in the Experimental Section. The Ag charges obtained for each conjugate for the same concentration of AgNP are, within error, equivalent. This shows that the three AgNP functionalization protocols do not affect the electrochemical analysis. The error bars represent the standard deviation from the mean for three independent experiments.

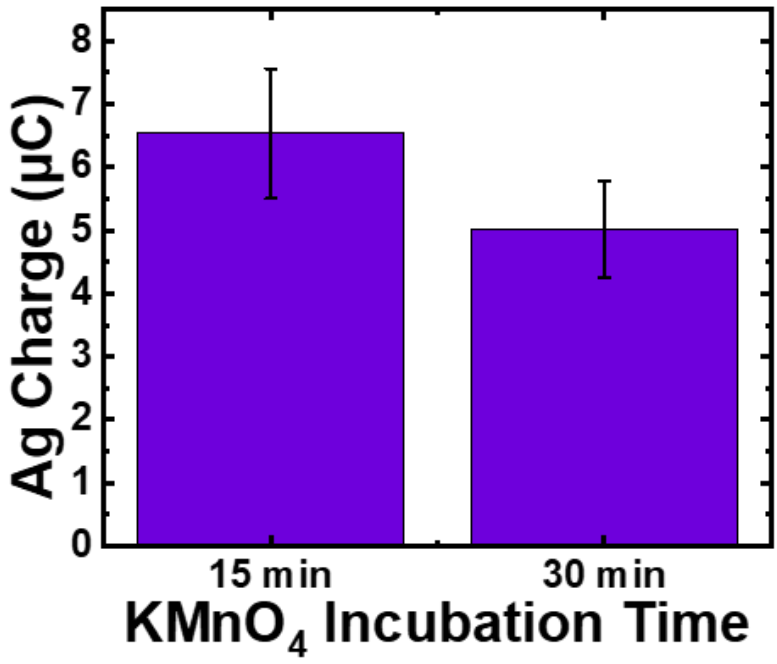

Figure 3.10 Electrochemical detection of unmodified, 20 nm-diameter, citrate-capped AgNPs incubated with $KMnO_4$ for the indicated times. The electrochemical procedure described in the Experimental Section was used. Briefly, however, 46 µL of 0.60 µM AgNPs in 1xPBS were incubated with 30 µL of 0.2 mM $KMnO_4$ for 15 and 30 min at 1000 rpm in the wells of a microtiter plate. Note that, here no target was immobilized on the wells of the microtiter plate. The entire content of each well was then placed on an electrode and the electrochemical protocol described in Chapter 3 was performed. The resulting Ag charges are not statistically different with a *p-value* greater than 0.05 (0.2380). This experiment proves that all of the AgNPs are oxidized within a 15 min incubation period. Thus, the experimental procedure used to obtain the ASV results discussed in Chapter 3 results in complete oxidation of the AgNPs. Therefore, the Ag charge detected corresponds to the binding activity of each conjugate for the immobilized target (N-terminal prohormone brain natriuretic peptide) on the plate. The maximum amount of target immobilized on the plate during the Ab activity experiments corresponded to 0.60 µM, and therefore a molar equivalent of AgNPs were used for this control experiment. Note that, the $KMnO_4$ solution was in excess, which was confirmed by the presence of the strong pink color observed throughout the experiment.

To prepare for electrochemical analysis, 46 µL of PBS and 30 µL of 0.2 mM $KMnO_4$ were added to the wells to denature the metalloimmunoassay and oxidize all bound AgNPs (Figure 3.9). After 15 min (a sufficient amount of time) of incubation at 1000 rpm, the entire content of the well (in a single drop) was then placed on an electrode for electrochemical analysis (Figure 3.10). Next, the working electrode was stepped from 0 to -0.70 V vs. a carbon quasi-reference for 800.0 s to electrodeposit Ag^+ in solution to Ag^0 on the electrode surface. After electrodeposition, anodic stripping voltammetry (ASV) was used to determine the Ag content on the working electrode surface. ASV was carried out by sweeping the working electrode potential from -0.70 to 0.20 V at 50 mV/s to oxidize Ag^0. The ASV traces were background subtracted (Figure 3.11).

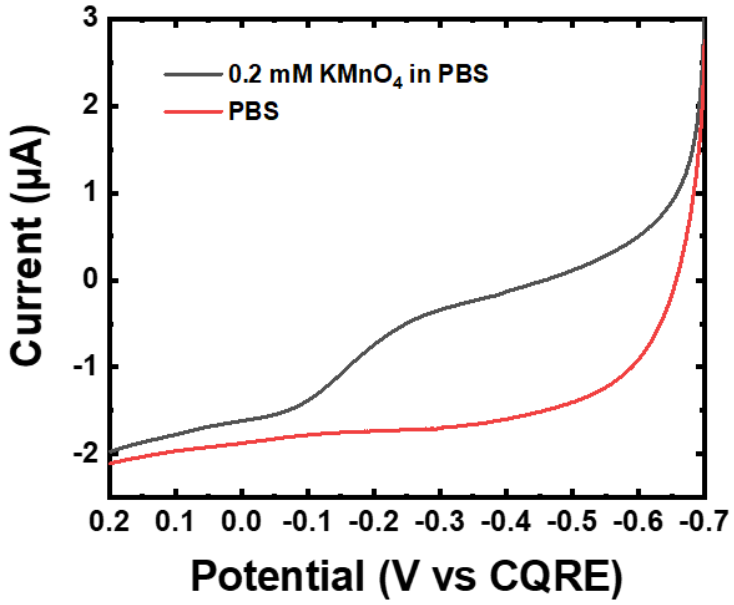

Figure 3.11 ASV results obtained using a solution containing only $KMnO_4$ and PBS. The electrochemical protocol described in the Experimental Section in of this chapter was used for these experiments. The electrochemical analysis was carried out in solutions containing: (black trace) 30 µL of freshly prepared 0.20 mM $KMnO_4$ and 46 µL of PBS; (red trace) 76 µL PBS. The purpose of this experiment was to evaluate the background current arising from the presence of $KMnO_4$. The black background trace was subtracted from all ASV data presented in this chapter.

The charge under the voltammogram was then determined by integration. It is important to note that this experiment was not intended to quantify total Ag from the assay since it relied solely on the diffusion of Ag^+ to the electrode surface, nonetheless, a variation in the Ag charge was obtained for the three conjugates.[65] This analysis was completed for identically prepared conjugate samples on days 0, 1, 2, 6, and 14, where day 0 represents the day the AgNPs were first conjugated to Ab-

HBCL1, Ab-HBCL2, and unmodified Abs. The Ag content was then correlated to the Ab activity of the conjugates. The stability of the AgNP portion of the conjugates was also tested using UV-vis spectroscopy, and these results can be found in Figure 3.12.

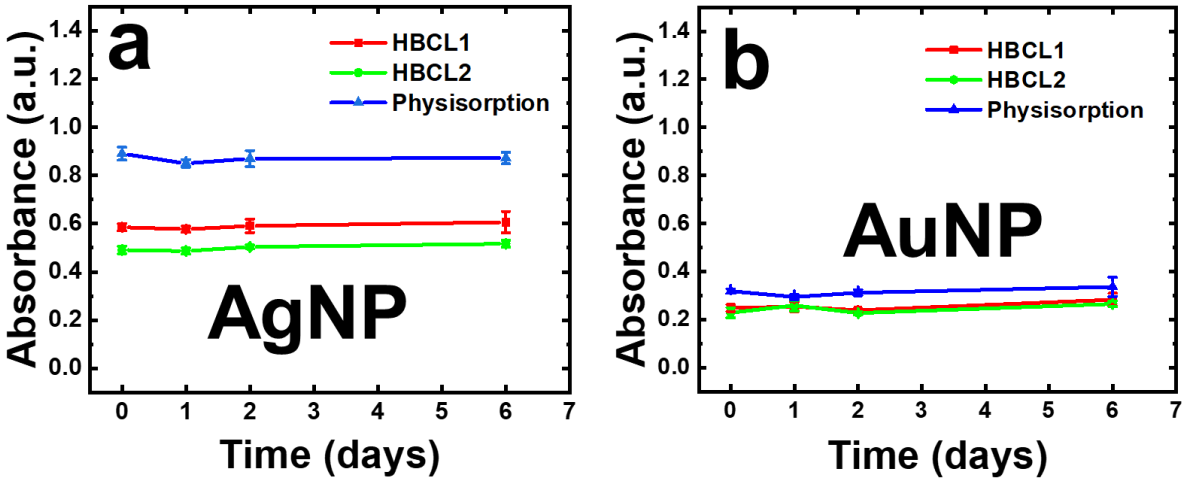

Figure 3.12 Spectrophotometric data related to the stability of AgNPs and AuNPs. The absorbance spectra were measured at (a) 395 nm for AgNPs and (b) 520 nm for AuNPs. This experiment was performed by freshly preparing the conjugates on day 0 and then analyzing the solutions on day 0, 1, 2, and 6. The NPs were suspended in SBB for analysis. 70 µL of each sample were added to the wells of a microtiter plate on each testing day and absorbance determined at the indicated wavelengths. The overall trend is that there is no change for either NP solution throughout the duration of the experiments. A decrease in intensity would be indicative of NP aggregation and because this is not observed, we conclude there is no detectable aggregation.[106,136,137]

3.4 Results and Discussion

3.4.1 Characterization of the AgNP-Ab conjugates

The hydrazone bioconjugation method has been used previously for preparing AuNP-Ab conjugates,[106] but to the best of our knowledge there are no such reports of HBCL-modified Abs being conjugated to AgNPs. The main goal of the present chapter, therefore, is to show that hydrazone bioconjugation is possible with AgNPs and that it is a superior alternative to physisorption. To accomplish this, AgNPs were conjugated with Ab-HBCL1, Ab-HBCL2, and unmodified Abs (physisorption), and resulting materials were characterized.

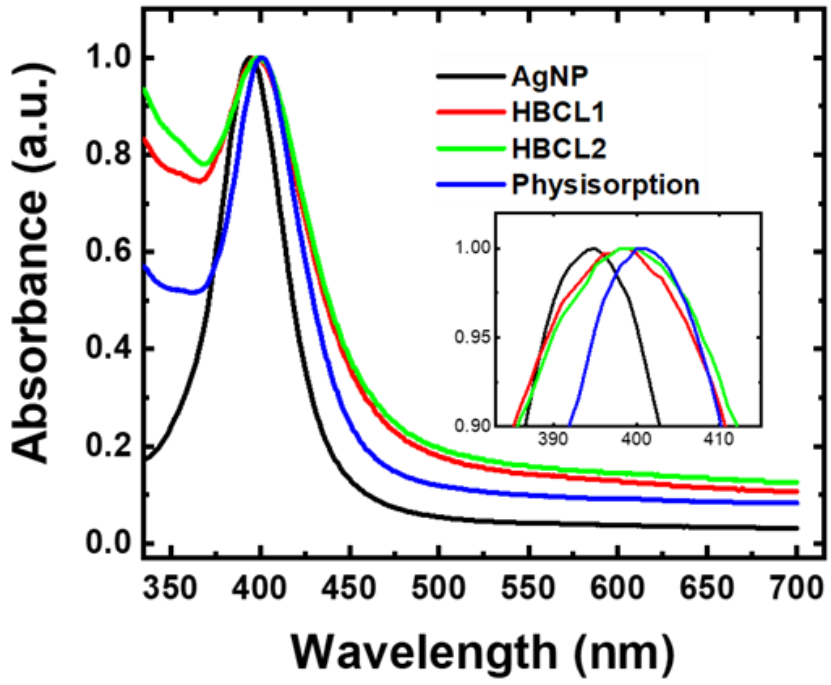

Figure 3.13 Normalized UV-Vis spectra of the citrate-capped AgNPs (black) and the AgNPs after bioconjugation with Ab-HBCL1 (red), Ab-HBCL2 (green), and unmodified Abs (physisorption, blue). The inset is an expanded view of the maxima of the plasmon peaks: λ_{max} = 395, 398, 398, and 400 nm for citrate-capped AgNPs, AgNP-HBCL1-Ab, AgNP-HBCL2-Ab, and physisorbed conjugates, respectively. The spectra are representative of three independent measurements, and λ_{max} did not shift within precision of the measurement (accuracy within 1 nm) for the three trials.

Figure 3.13 shows representative UV-Vis spectra for unconjugated 20 nm AgNPs and the three Ab conjugates. The characteristic plasmon band for the unmodified, citrate-capped AgNPs is present at λ_{max} = 395 nm (black trace). After functionalization with Ab-HBCLs or unmodified Abs, the plasmon band undergoes a red-shift of 3 nm (red and green traces) and 5 nm (blue trace), respectively. This red shift is in agreement

with a change in the refractive index of the environment surrounding the metallic NPs,[136,137] which is characteristic of bioconjugation. Note that the spectra depicted in Figure 3.12 are normalized to a λ_{max} intensity of 1.0 to better highlight the red shift. The same experiments were carried out with AuNPs as a benchmark, and the results are shown in Figure 3.14.

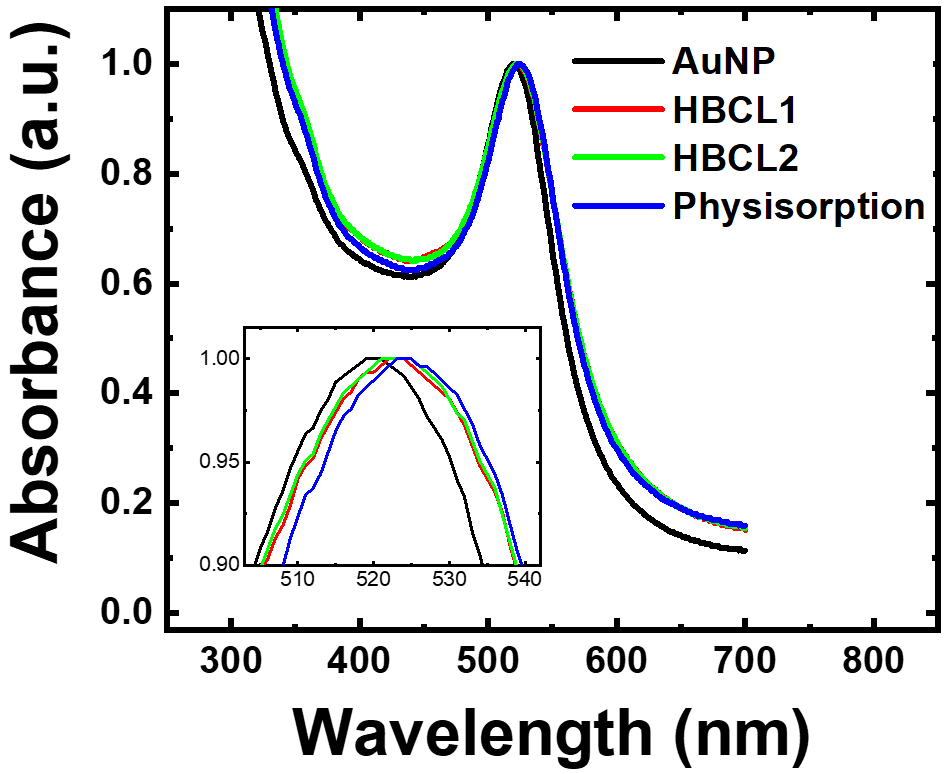

Figure 3.14 Normalized UV-Vis spectra of 20 nm-diameter citrate-capped AuNPs before (black) and after bioconjugation with HBCL1-modified Abs (red), HBCL2-modified Abs (green), and unmodified Abs (physisorption, blue). The AuNP-HCBL-Ab conjugates were prepared using the procedure described in the Experimental Section of the main text. The inset is an expanded view of the maxima of the plasmon peaks. λ_{max} = 520, 523, 523 and 525 nm for citrate-capped AuNPs, AuNP-HBCL1-Ab, AuNP-HBCL2-Ab and physisorbed conjugates, respectively. The experiment was carried out by adding 100 µL of each solution (containing the NPs and SBB) to the wells of a microtiter plate. For clarity, only one spectrum of triplicate measurements is depicted here. λ_{max} did not shift within the precision of the measurement (accuracy within 1 nm). The shift in the plasmon peak corresponds to a change in the refractive index of the environment of the NP[136,137] and is in agreement with literature results.[106]

In this case a similar red shift of 3 to 5 nm was observed. From these results, we conclude that the AgNPs have been successfully conjugated to the Abs. In a subsequent section we will discuss the extent of conjugation.

3.4.2 Quantification of the total number of Abs per AgNP

It is usually not possible to directly quantify the number of Abs or proteins on a solid phase, such as a NP, because the solid phase can interfere with the analysis.[104] To avoid such interferences, destructive techniques can be used. These include dissolution of the metal NP to prevent fluorescence quenching,[138–140,141,142] or complete digestion of the conjugate followed by high-performance liquid chromatography to determine the total protein content on the NP.[143] However, we wanted to avoid destructive techniques so that it would be possible to compare every batch of conjugates without having to sacrifice samples. Thus, an indirect quantification method was used; that is, measuring the amount of unbound Abs remaining after bioconjugation.

The number of unbound Abs for the three conjugates in this study were determined as follows. First, the conjugation reaction was carried out. Second, the supernatant resulting from the first centrifugation (washing) step, which contains the unbound Abs, was collected. Third, an indirect ELISA was

performed following the procedure described in the Experimental Section of this chapter.

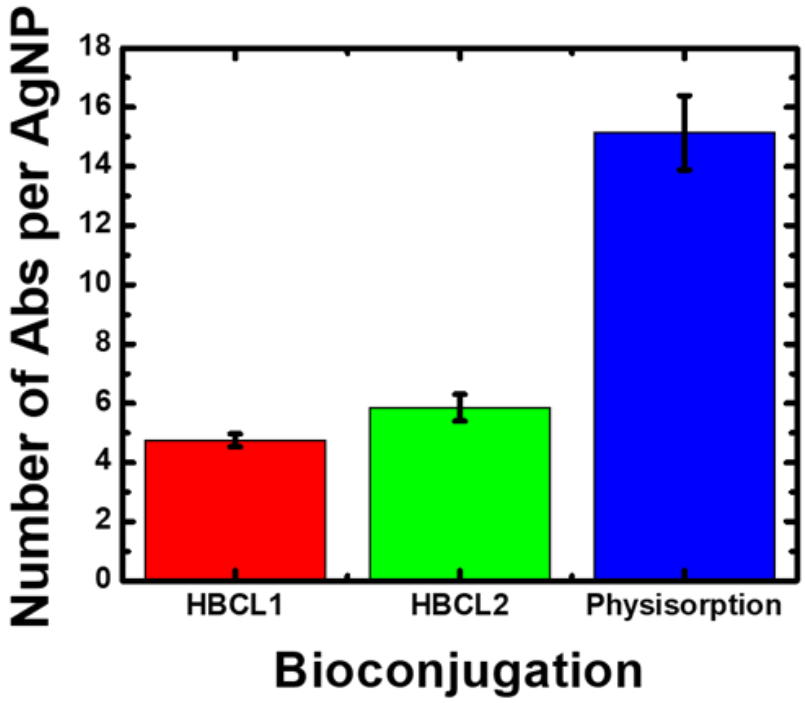

Figure 3.15 Histogram showing the number of Abs bound per AgNP for each of the conjugation methods. The data were obtained using an indirect enzyme-linked immunosorbent assay (ELISA). The error bars represent the standard deviation of three independent measurements.

Figure 3.15 is a histogram of the results from the indirect ELISA. The data represent results obtained from three independent reactions for each conjugate. Interestingly, the coverage is strongly dependent on the conjugation method. More specifically, using the hydrazone chemistry, 5 ± 1 Abs are reproducibly immobilized per AgNP for both HBCLs, while approximately three times more Abs are directly physisorbed to

the AgNPs. These trends are similar to those we determined for AuNPs (Figure 3.7).

To ensure that the foregoing results are within a reasonable range, we calculated the approximate maximum Ab coverages for our materials. By considering typical dimensions for an Ab (14.5 nm x 8.5 nm x 4 nm),[130] the surface area of a smooth 20.0 nm-diameter sphere (1260 nm^2), and the orientation of the surface-confined Abs, it is possible to estimate maximum coverage. Using this approach, the maximum coverage for Abs oriented side-on is 10, while for end-on coverage it is 40. As shown in Figure 3.14, the coverage of physisorbed Abs on 20 nm AgNPs is 15 ± 2 Abs/NP, which is almost the same as we measured for physisorption onto AuNPs (13 ± 2 Abs/NP, Figure 3.7). This suggests that, independent of the metal, physisorbed Abs are present in both side-on and end-on orientations. There may also be Ab-Ab interactions that result in bilayer formation.

In contrast to physisorption, Abs immobilized *via* the hydrazone method should bind only in an end-on orientation due to the positioning of the HBCLs on the Fc region of the Ab. This configuration should result in higher activity. Evidence for significant structural differences between physisorbed Abs and those linked *via* the HBCLs comes from dynamic light scattering measurements (Table 3.1). The increase in

hydrodynamic diameter (Δ_H) of the physisorbed materials was found to be 24.6 ± 1.2 nm, while for the materials having HBCLs the Δ_H were 9.4 ± 0.7 and 7.1 ± 1.3 nm for AgNP-HBCL1-Ab and AgNP-HBCL2-Ab, respectively.

Sample	Change in hydrodynamic diameter (Δ_H)
Physisorbed conjugate in SBB	24.6 ± 1.2 nm
AgNP-HBCL1-Ab in SBB	9.4 ± 0.7 nm
AgNP-HBCL2-Ab in SBB	7.1 ± 1.3 nm

Table 3.1 Hydrodynamic diameter measurements obtained for various AgNP conjugates using dynamic light scattering spectroscopy (DLS). The experiment was performed as follow: 1 mL of 0.25 nM AgNP solution was added to a quartz cuvette through a PTFE 0.2 µm membrane. The DLS measurement was performed in triplicate. A change in the hydrodynamic diameter was reported in comparison to the hydrodynamic diameter of AgNP in SBB. All the quartz cuvettes were washed with aqua regia (3 HCl: 1 HNO_3) prior to being used to get rid of any residual NPs. The HBCL itself was used as the "backfill" ligand in these experiments in place of the mPEG-SH. The mPEG-SH used in the conjugate protocol has a molecular weight of 5 kDa, which would generate false increased diameters with this technique.

3.4.3 Comparison of the Ab activity of the conjugates

To confirm the orientations of the Abs, our next step was to quantitatively compare their binding activity for a specific antigen, NT-proBNP. The basis for correlating antigen-binding activity to orientation is the well-known fact that only an accessible and intact Fab region will bind its antigen.[104,115]

Here, Ab activity was directly determined using the half-metalloimmunoassay described in the Experimental Section. Briefly, the target, NT-proBNP, was adsorbed to the wells of a microtiter plate, then the AgNP-labeled Ab conjugates were introduced, and after washing, the amount of Ag present in each well was determined by anodic stripping voltammetry (ASV). In this assay, only the active fraction of the Abs will bind to the immobilized target, and therefore the amount of Ag charge collected is indicative of Abs having an end-on (active) orientation.[130]

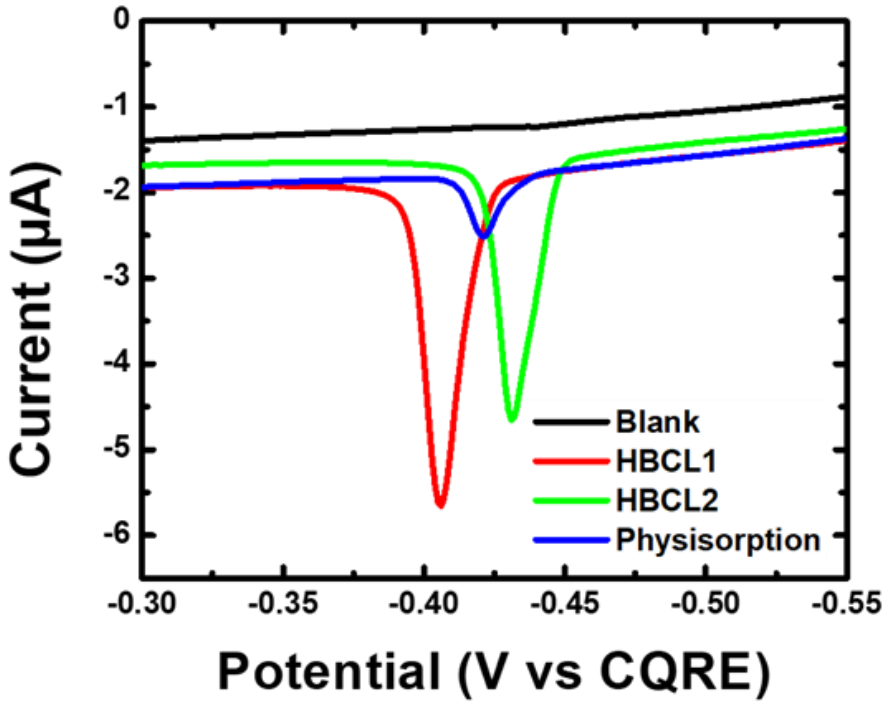

Figure 3.16 Anodic stripping voltammograms (ASVs) obtained by forming a half-metalloimmunoassay with the conjugates in a microtiter plate, adding $KMnO_4$ to oxidize bound AgNPs, transferring the entire contents of each well to a carbon paste working electrode, and then carrying out the electrochemical protocol discussed in the text. The scan rate was 50 mV/s. For clarity, only one ASV trace is shown for each conjugate, but the measurements were carried out in triplicate. The position of the ASV peaks varies due to the use of a quasi-carbon reference electrode.

Figure 3.16 shows Ag ASV traces for the half-metalloimmunoassay formed with the AgNP-Ab conjugates. Each trace is representative of three individually formed half-metalloimmunoassays that were tested on three independently prepared electrodes. The blank for this experiment consisted of citrate-capped AgNPs suspended in SBB with no Abs present. Both AgNP-HBCL-Ab conjugates (red and green traces) yielded an

average Ag charge of 1.68 ± 0.20 µC, while the physisorbed conjugate (blue trace) gave just 0.41 ± 0.06 µC.

This experiment clearly proves the superiority of the hydrazone conjugation method compared to the more common physisorption technique. Specifically, despite a low quantity of immobilized Abs (5 vs. 15 for the HBCL and physisorbed conjugates, respectively), the higher charge obtained for the AgNP-HBCL-Ab conjugates is evidence of the orientation control exerted by the cross-linker. On the other hand, the lower charge resulting from the physisorbed conjugates can be related to misorientation of the Abs on the AgNP surface. Additionally, the weak electrostatic interactions might not have been sufficient to keep the Abs on the AgNP surface during formation of the metalloimmunoassay. The key point is that HBCLs help to circumvent these drawbacks.

3.4.4 Determination of the stability of the Abs

To more fully characterize the AgNP-HBCL-Ab conjugates, their stability (Figure 3.12) and that of the Abs on the AgNP were examined. The stability of the Ab portion of the conjugates was determined electrochemically using the protocol described in the previous section. The only difference being that the assay was carried out on 0, 1, 2, 6, and 14 days after the conjugates were

prepared. Day 0 corresponds to the day they were first assembled.

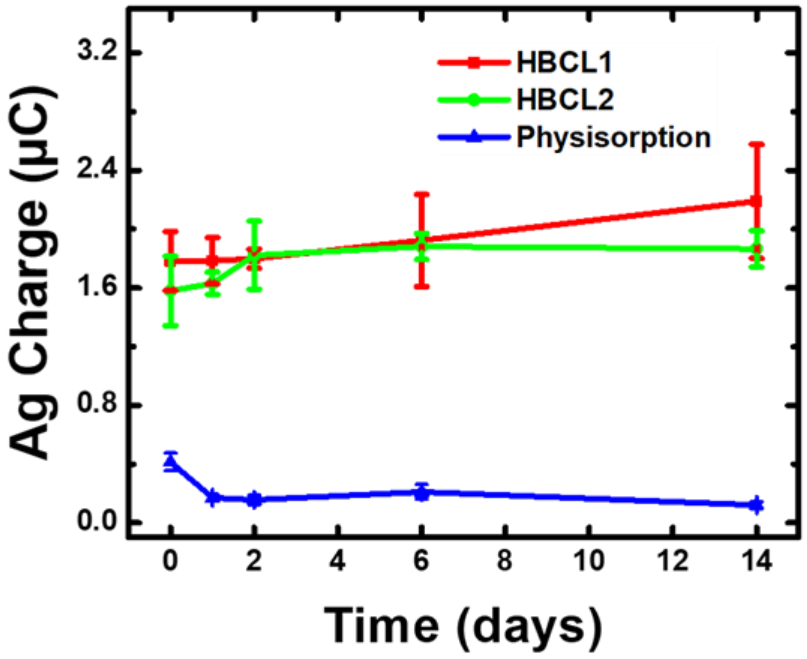

Figure 3.17 Ag charge obtained for the conjugates using the same electrochemical protocol as in Figure 3.16, but performed on days 0, 1, 2, 6, and 14. Day 0 indicates the day the conjugates were prepared. Each data point represents the standard deviation from the mean for three replicate measurements obtained using independently prepared electrodes.

Figure 3.17 is a plot of the Ag charge resulting from the ASV analysis of the half-metalloimmunoassays as a function of time. The AgNP-HBCL1-Ab and AgNP-HBCL2-Ab conjugates, shown in red and green respectively, display the same average activity throughout the 14-day study. This is an important result, because typically the stability of metal-conjugated Abs is not reported (only the

stability of the NPs is reported). The outcome of this stability study is beneficial for many applications, because it is important to know how reliable the NP-Ab conjugates are in solution for a given amount of time. In contrast to the HBCL conjugates, the physisorbed conjugates (blue) underwent a nearly 60% decrease in activity between day 0 and day 1. This decrease from 0.41 ± 0.06 µC to 0.17 ± 0.02 µC is in accord with the poor stability of other physisorbed conjugates reported in the literature.[115,123,124] Specifically, the electrostatic interactions between Abs and NPs are weak and lead to desorption over time.[104] Additionally, it is well-known that protein-surface interactions may induce conformational changes in Abs after some time. This is due to the physisorbed Abs slowly reconfiguring their packing to reach equilibrium. This process may also cause the protein to unfold and lose activity.[144]

3.4.5 Investigation of the stability of the HBCLs

This part of our study focused on the relative stability of the two HBCLs. The preceding results have demonstrated that despite differences in their chemical compositions, HBCL1 and HBCL2 are equivalent in terms of conjugation efficiency and Ab stability. On the other hand, assays performed with HBCL1 tended to produce irreproducible results over a time period of a few months (data not shown). Such a decrease in bioconjugation efficiency can

potentially be caused by a time-dependent change at either end (thiol or hydrazide) of the cross-linker resulting in poor attachment of the HBCL to the NP or the Ab, respectively. Thus, an NMR stability study was performed on HBCL1 and HBCL2 to identify possible structural changes. Note: this part of the study was focused on just the cross-linkers, not the conjugates.

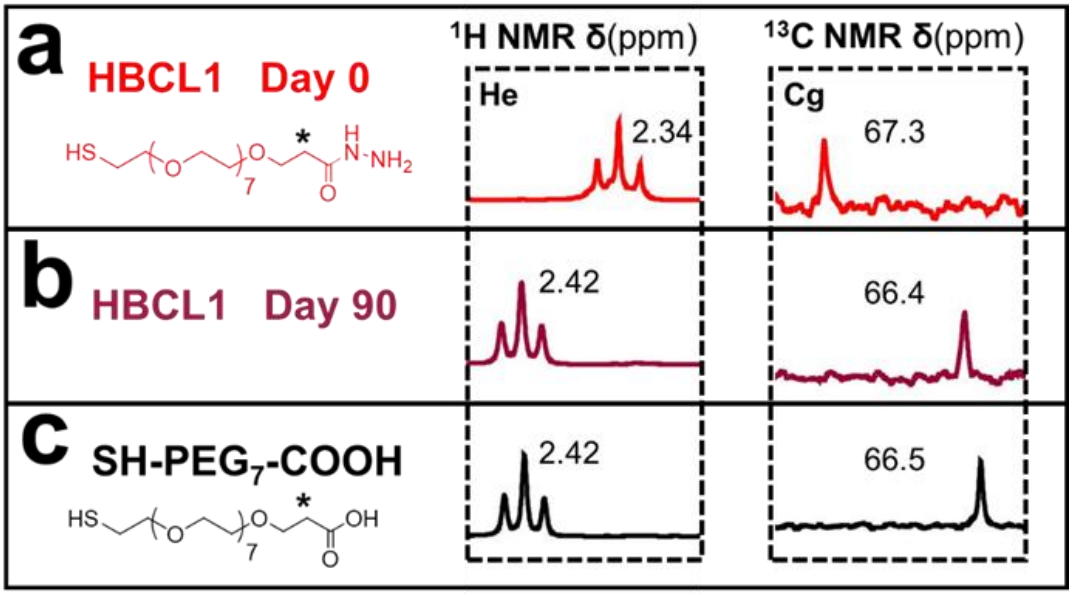

Figure 3.18 Stability study of HBCL1 (just the linker, not the full conjugate) as a function of time. The ^{1}H and ^{13}C NMR (400 MHz, $DMSO_{d6}$) spectra of HBCL1 are shown at (a) day 0 and (b) day 90. The cross-linker was stored in DI water during the 90-day period. **He** and **Cg** peaks are denoted by an asterisk. Figure 3.1 provides complete labeling of the spectra. (c) The ^{1}H and ^{13}C NMR (400 MHz, $DMSO_{d6}$) spectra of SH-PEG_7-COOH.

Figure 3.18 presents the ^{1}H and ^{13}C NMR spectra and chemical shifts for the methylene group closest to the hydrazide-end of HBCL1, marked as (*), resulting from a 90-day study. In Figure 3.18a and 3.18b, the NMR spectra of HBCL1 is shown for days 0

and 90, respectively. Figure 3.18c presents the spectra of SH-PEG_7-COOH, a possible degradation product of HBCL1. After 90 days, the protons of the methylene group (*****) underwent a strong deshielding from 2.34 to 2.42 ppm, meanwhile the carbon underwent a slight shielding from 67.3 to 66.4 ppm. This means that the composition of the adjacent carbo-hydrazide group was altered. The chemical shifts obtained at day 90 correspond perfectly to the signature shifts of SH-PEG_7-COOH. The correlation of the NMR shifts confirms the transformation of HBCL1 into a non-reactive form.

Finally, no evidence of chemical shifts was observed for HBCL2 over the 90-day test duration, which confirms that HBCL2 is chemically stable within this time frame in aqueous solution (Figure 3.3). We attribute the increased stability to the difference in the composition of the spacer arms (PEG vs. alkyl chains). Presumably, the PEG residues affect the solubility of the molecule and bring a water-rich environment close to the hydrazide, while the alkyl chain will have the opposite effect. All in all, these findings show that HBCL2 is the more advantageous cross-linker, and therefore it is the better choice for bioassays.

3.5 Summary and Conclusion

To summarize, the goal of this study was to develop a nearly universal route for conjugating Abs to AgNPs. We elected the hydrazone bioconjugation method, because it provides control over the orientation of the Abs by targeting the Fc region of Abs. We also took advantage of the affinity of the thiol endgroup for the AgNP surface. Using this generalized format, two novel HBCLs were synthesized with each bearing a hydrazide group for forming the hydrazone bond with the Abs, and a thiol group for forming a dative bond with the AgNP surface. The results showed that the AgNP-HBCL-Ab conjugates are reproducible and consist of an average of 5 ± 1 Abs per AgNP.

Using a half-metalloimmunoassay, it was possible to show that the hydrazone bioconjugation method significantly improves the activity of the conjugated Abs compared to the more common physisorption technique. Moreover, the AgNP-HBCL-Ab conjugates are stable for at least 14 days, while the physisorbed conjugates exhibit a sharp decrease in stability one day after preparation. Finally, we found that the spacer arm of the HBCLs plays an important role in the stability of the hydrazide group of the cross-linker. More specifically, an alkyl chain spacer confers significantly more stability to the HBCL than a PEG spacer.

In conclusion, the method reported here provides a viable route for conjugation of AgNPs to Abs. This finding is significant given the recent interest in using AgNPs as electrochemical[57,58,61] and spectroscopic[113,114,118,119] labels for bioassays. Indeed, we are currently using the AgNP-HBCL2-Ab conjugate as a key component of a point-of-care electrochemical sensor for heart failure.[59] The results of that work will be reported in due course.

Chapter 4: Electrochemical Detection of NT-proBNP using a Metalloimmunoassay on a Paper Electrode Platform

4.1 Synopsis

In this chapter we demonstrate an electrochemical method for detection of the heart failure biomarker, N-terminal prohormone brain natriuretic peptide (NT-proBNP). The approach is based on a paper electrode assembly and a metalloimmunoassay; it is intended for eventual integration into a home-use sensor. Sensing of NT-proBNP relies on the formation of a sandwich immunoassay and electrochemical quantification of silver nanoparticle (AgNP) labels attached to the detection antibodies (Abs). There are four important outcomes reported in this chapter. First, compared to physisorption of the detection Abs on the AgNP labels, a 27-fold increase in signal is observed when a heterobifunctional cross-linker is used to facilitate this labeling. Second, the assay is selective in that it does not cross-react with other cardiac natriuretic peptides. Third, the assay forms in undiluted human serum (though the electrochemical analysis is carried out in buffer). Finally, and most important, the assay is able to detect NT-proBNP at concentrations between 0.58-2.33 nM. This performance approaches

the critical NT-proBNP concentration threshold often used by physicians for risk stratification purposes: ~0.116 nM.*

* Chapter 4 is based on a pervious publication: N. E. Pollok; C. Rabin, C. T. Walgama, L. Smith, I. Richards, R. M. Crooks, Electrochemical Detection of NT-proBNP Using a Metalloimmunoassay on a Paper Electrode Platform. *ACS Sensors* 2020, 5, 853-860. NEP designed the experiments. RMC was the research advisor. IR contributed to the generation of ideas and experimental design. CR, CTW, and LS assisted in data collection.

4.2 Introduction

Here, we report on the detection of the cardiac biomarker, N-terminal prohormone brain natriuretic peptide (NT-proBNP) using a metalloimmunoassay adapted to a paper-based electrochemical sensor. There are four important outcomes of this study. First, the use of a heterobifunctional cross-linker (HBCL), instead of the more common physisorption technique, for the bioconjugation of monoclonal immunoglobulin G antibodies (Abs) to silver nanoparticle (AgNP) labels improves the limit of detection and reproducibility of the assay. Second, the assay is selective in that there is no cross-reactivity with other cardiac natriuretic peptides, such as brain, atrial, and C-type natriuretic peptides (BNP, ANP, and CNP, respectively).[145–147] Third, detection of NT-proBNP is not impacted by matrix effects[148,149] in that the sandwich assay forms in undiluted human serum prior to analysis. Finally, and most important, the assay is able to detect NT-proBNP at concentrations between 0.58-2.33 nM with an overall relative standard deviation of <15%. These findings represent a notable contribution to current efforts aimed at detecting NT-proBNP using a state-of-the-art system that is evolving toward home-use applications.[150–153]

NT-proBNP is a peptide that is secreted by ventricular cardiomyocytes that are stretched as a consequence of cardiac

volume overload. [154,155] Stretching of these heart muscle cells results in secretion of the prohormone brain natriuretic peptide (proBNP), which is enzymatically cleaved into BNP and NT-proBNP before being released into the bloodstream.[155,156] The primary function of natriuretic peptides, such as BNP, ANP, and CNP, are to lower the blood pressure by increasing natriuresis and diuresis (reducing excess salt and water retention), inhibit the production and action of vasoconstrictor peptides, and promote vascular relaxation.[157] The overall effect of this cascade of events is to reduce cardiac output and central venous pressure.

Because they both originate from proBNP, BNP and NT-proBNP are initially present in equal concentrations in the body. The biological function of NT-proBNP is unknown, but for a number of reasons it is used as a proxy for BNP in clinical settings to track the progression and severity of HF. Specifically, the circulation half-life of NT-proBNP in the body is six times longer than BNP (120 min vs. 20 min, respectively), making it a more desirable biomarker for HF.[158]

The critical NT-proBNP concentration threshold used by physicians for risk stratification purposes is 1000 pg/mL (116 pM).[159–162] This threshold allows physicians to identify HF patients as being at a high or low risk of hospitalization or mortality. It should be noted, however, that serum natriuretic

peptide concentration values can vary greatly depending on co-morbidities, race, disease severity, and the age of the patient.[162–167] Due to this variability, it would be desirable for HF patients to be able to monitor their HF status at home, because this could reduce the likelihood of decompensation and hospitalization.[168–170] This is the motivation for the study presented here.

There are numerous analytical methods for detecting NT-proBNP, such as enzyme-linked immunosorbent assays (ELISA),[55,171] immunofluorescence,[172,13] and electrochemiluminescence (ECL).[14–17] These methods typically require some type of immunological or aptameric[173,174] technique to capture the peptide, and also a signal amplification mechanism.[41] For example, in 2017, Shi *et al.* developed a sandwich-type (immunoassay) ECL sensor for detecting clinical levels of NT-proBNP, in which the concentration of NT-proBNP in diluted human serum was correlated to the ECL quenching efficiency.[14] In another example, an immunochromatographic assay consisting of monoclonal Abs labeled with a genetically engineered fluorescent protein was used to capture NT-proBNP on nitrocellulose paper, and then the assay was quantified fluorometrically.[13] While these methods provide low limits of detection, they are not appropriate for home use.

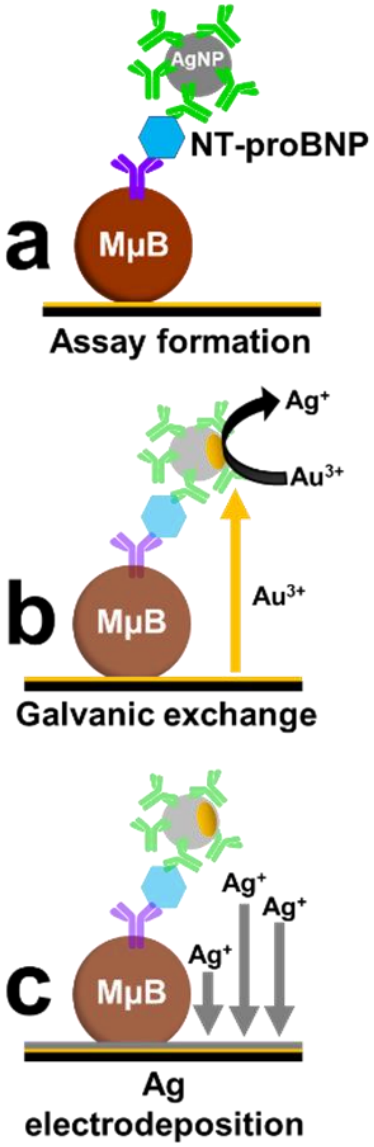

Illustration 4.1. Scheme of the galvanic exchange method used to detect Ag following formaiton of the assay.

Our group previously reported on electrochemical detection of NT-proBNP using a metalloimmunoassay consisting of a capture Ab conjugated to a magnetic microbead (MμB) and a AgNP-labeled detection Ab.[59] As shown in Illustration 4.1, the detection

process, which has its roots in a method reported by Limoges and coworkers,[54] proceeds as follows. First, the peptide is captured by the Ab pair in solution, and then the MμB is brought to the electrode surface by a magnetic force for detection (Illustration 4.1a). In this case, and in our previous reports,[57,58,61] the detection Ab is physisorbed to a AgNP label. Second, a process known as galvanic exchange (GE) is used to detect the AgNPs electrochemically.[127,66] GE takes advantage of a difference in the standard potentials of two metals such that they undergo a redox process. In our detection system (Illustration 4.1b) the metals are Au and Ag (E^0 = 1.52 and 0.79 V, respectively).[65] The more noble Au^0 is pre-electrodeposited on an electrode and then is electrochemically oxidized to Au^{3+} which subsequently diffuses to the AgNPs and then spontaneously exchanges with the less noble, zerovalent AgNP labels. This results in oxidation of the AgNPs to Ag^+, which, in a third step, is subsequently electrodeposited onto the working electrode (Illustration 4.1c). Finally, anodic stripping voltammetry (ASV) is used to quantify the amount of Ag on the electrode surface. The resulting charge is directly related to the amount of target originally present in the sample.

The predominant means for immobilizing Abs on metal nanoparticles is physisorption.[54,142,175–178] In this context,

physisorption relies primarily on interactions between the surface of a metal, and thiol and amine residues present on Abs.[62,112] While this bioconjugation method is quick and simple, the active orientation of the Abs on the nanoparticle surface is not well controlled unless the Ab is specifically engineered to bind in a particular way.[179] Misorientation of the detection Ab can result in poor activity of the Ab in a metalloimmunoassay.[115] An additional disadvantage of physisorption is that there is a likelihood that other biomolecules present in real biological matrixes will effectively compete for the metal nanoparticle surface, thereby dislodging the detection Abs.[62,123,148,149] For these reasons, we sought to control the orientation of the Abs on the AgNP surface with a hydrazide- and dithiolane-containing HBCL, which has previously been reported by our group[180] to have a positive effect on the capture efficiency of Abs on the surface of AgNPs by targeting the fragment crystallizable (Fc) region.[106]

The primary goal of the present chapter is to report a bioassay that can be integrated into an electrochemical detection workflow on a paper-based, point-of-need device. Accordingly, we report on a metalloimmunoassay for NT-proBNP using a HBCL to bioconjugate AgNPs to the detection Ab rather than the more common physisorption technique. This makes it

possible to detect NT-proBNP near the risk stratification threshold in buffered solution. Additionally, the assay is selective for NT-proBNP compared to other cardiac natriuretic peptides, and it resists matrix effects associated with human serum.

4.3 Experimental

4.3.1 Chemicals and Materials

All solutions were prepared using deionized (DI) water (>18.0 MΩ-cm, Milli-Q Gradient System, Millipore, Burlington, MA). Phosphate buffered saline (PBS) pH 7.4 (P3813), casein, superblock blocking buffer containing PBS (SBB) (cat. no. 37515), siliconized low-retention microcentrifuge tubes, H_2SO_4, $HAuCl_4$, KNO_3, Whatman grade 1 chromatography paper (180 µm thick, 20 cm × 20 cm sheets, linear flow rate of water = 0.43 cm/min), and Costar 3590 high-binding microtiter plates were purchased from Fisher Scientific (Pittsburgh, PA). A horseradish peroxidase (HRP) conjugate kit (cat. no. LNK002P) was purchased from Bio-Rad (Richmond, CA).

All PBS concentrations were 1x. The 5 kDa mPEG-SH was obtained from Nanocs (New York, NY). 1-Step Ultra TMB-ELISA Substrate Solution (34028) and sodium meta-periodate ($NaIO_4$) were obtained from Thermo Scientific (Grand Island, NY). Citrate-

capped AgNPs (nominal 20 nm diameter) were purchased from nanoComposix (San Diego, CA). N-terminal prohormone brain natriuretic peptide (NT-proBNP), monoclonal immunoglobulin G anti-NT-proBNP 13G12 detection Ab, biotinylated monoclonal immunoglobulin G anti-NT-proBNP 15C4 capture Ab (15C4-biotin), and non-biotinylated monoclonal immunoglobulin G anti-NT-proBNP 15C4 capture Ab were obtained from HyTest (Turku, Finland). Polyclonal anti-mouse immunoglobulin G HRP-labeled secondary antibody (SAb) and prohormone brain natriuretic peptide (proBNP) were obtained from Abcam (Cambridge, UK). Atrial natriuretic peptide (ANP), C-type natriuretic peptide (CNP), brain natriuretic peptide (BNP), and polyoxyethylene (20) sorbitan monolaurate (Tween-20) were purchased from Sigma-Aldrich (St. Louis, MO). Human chorionic gonadotropin (hCG) was purchased from Fitzgerald (Acton, MA). Streptavidin-coated magnetic microbeads (MμBs) having a diameter of 1.0 μm (cat. no. 65601) were obtained from Life Technologies (Grand Island, NY).

Amicon ultra 0.5 mL centrifugal filters (10 K) and normal human serum were purchased from Millipore-Sigma (Taunton, MA). Conductive carbon paste (Cl-2042) was purchased from Engineered Conductive Materials (Delaware, OH). Cylindrical neodymium magnets (1/16 in x ½ in, N48) were purchased from Apex Magnets

(Petersburg, WV). All chemicals and reagents were used without further purification unless otherwise specified.

4.3.2 Instrumentation

Absorbance measurements were obtained and path length corrected using a Synergy H4 Hybrid Multi-Mode Microplate Reader from BioTek (Winooshi, VT). A Sorvall Legend Micro 21R centrifuge from Thermo Scientific (Grand Island, NY) was used for washing and separation steps during bioconjugation. A tube revolver (cat. no. 88881001), also from Thermo Scientific, was used for incubation steps during the conjugation of Abs to MµBs. A Mini Vortexer (945300) from VWR International (Radnor, PA) was used to briefly mix solutions while a BioShake iQ from Quantifoil Instruments GmbH (Jena, Germany) was used for incubation steps during bioconjugation. A magnetic bead separation block (cat. no. VP771HH-Rz) was purchased from V&P Scientific (San Diego, CA) and was used for washing steps involving MµBs.

4.3.3 Electrode fabrication

A slight modification of a previously published procedure was used to fabricate the electrodes.[127] Specifically, they were fabricated by stencil-printing carbon paste onto wax-patterned sheets of chromatography paper that had been printed using a Xerox ColorQube 8570DN printer. Following printing, the wax was melted through the thickness of the paper by placing it in an

oven at 120 °C for 25.0 s. Photopaper was glued to the back of the wax-printed chromatography paper to improve rigidity, and then it was cut into 12 rectangles (2.0 cm × 5.0 cm, each). A stencil for defining the 3.0 mm-diameter disk-shaped working electrode, hook-shaped carbon quasi-reference electrode, and counter electrode was created using CorelDRAW (Ottawa, ON). The stencil was cut into a thin plastic sheet of transparency film using an Epilog laser engraving system (Zing 16). Finally, the stencil was placed over the paper (wax side up), the electrodes were printed through the stencil using the conductive carbon paste, and then they were left to dry in air for 14 h (Illustration 4.2).

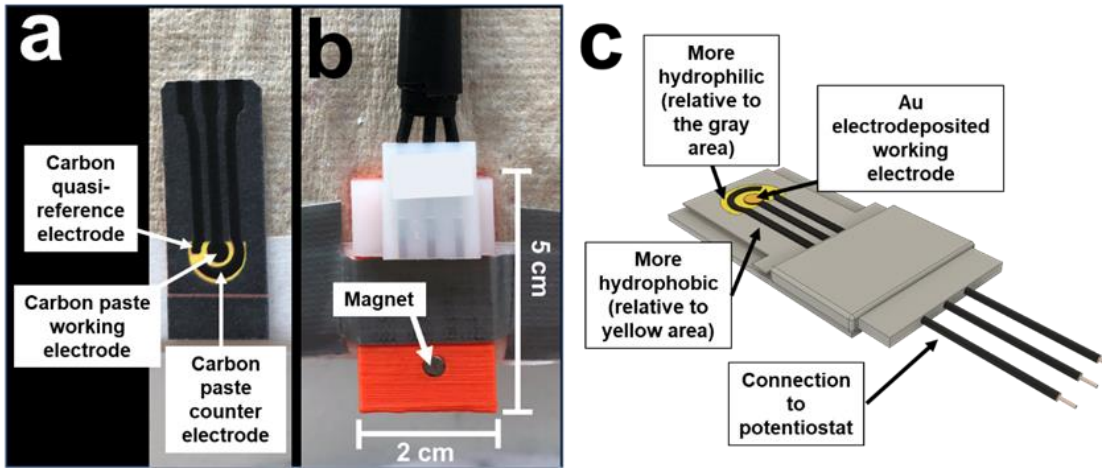

Illustration 4.2 Description of the paper electrochemical platform used for determining the amount of Ag charge obtained from the metalloimmunoassay for NT-proBNP. Electrode fabrication steps such as Au pre-electrodeposition on the working electrode and anodic stripping voltammetry were performed using this device. (a) Photograph of the electrodes before Au was electrodeposited on the working electrode. (b) Photograph of the cell which contains a magnet and holds the paper device. (c) Computer-aided design image of the fully assembled cell featuring the Au electrodeposited working electrode. The white portion of the cell (b) incorporates metal contacts within the enclosure to provide ohmic contact between the carbon paste electrodes and the potentiostat. Duct tape is placed across the orange platform of the cell to hold it in place during analysis. As discussed in the Experimental Section of this chapter, the electrodes were stencil printed with conductive carbon paste. When the device is fully assembled, the magnet is located behind the working electrode. The regions printed in yellow wax (c) are more hydrophilic compared to the gray wax regions, thus allowing for the sample solution to span all three carbon electrodes. The yellow region can hold an aqueous volume of 50-80 µL. In the present chapter, 50.0 µL of sample solution were added to the electrode region.[180]

The working electrode was further modified by electrodepositing Au onto the carbon paste. This step was performed on-chip and was carried out by placing a.0 µL droplet of a solution consisting of 6.0 mM $HAuCl_4$ and 0.10 M KNO_3 on the electrode region of the sensor. Because the region of the sensor incorporating the electrodes is hydrophilic relative to the rest of the paper assembly, the deposition solution was confined to just the electrode region and hence no additional electrochemical cell was required. Next, the potential of the working electrode was stepped from 0 V to -0.60 V (unless otherwise stated, all potentials are vs. a carbon quasi-reference electrode, CQRE) for 2.0 s.[127] This process results in islands of Au (not a conformal coating) on the surface of the carbon.[127] The electrode was then rinsed twice with DI water, and dried with a Kimwipe (Illustration 4.2).

4.3.4 Electrochemical detection

All electrochemical measurements were performed using a CH Instruments model 760B electrochemical workstation (Austin, TX). A previously published electrochemical protocol was used to determine the charge resulting from the process illustrated in Illustration 4.1.[127] Briefly, to initiate GE, the potential of the working electrode was stepped from 0 to 0.80 V for 12.0 s to oxidize Au^0 to Au^{3+}. Next, the potential was stepped from 0 to -

0.70 V for 50.0 s to reduce Ag^{+} to Ag^{0} onto the electrode. These two steps were carried out twice, and then the potential was swept two times from -0.70 to 0.20 V at a scan rate of 50.0 mV/s to oxidize Ag^{0}. The charge resulting from the last ASV scan was obtained by integration and represents the output signal of the sensor.[66,127] All electrochemical measurements were performed in a PBS solution.

4.3.5 Assessing Ab cross-reactivity

The cross-reactivity of the 13G12 and 15C4 Abs was determined using an indirect, half ELISA and a full capture ELISA. The 13G12-HRP Ab was prepared using a kit and protocol provided by the manufacturer.[181] Unless stated otherwise, all incubation steps were performed for 30 min at 600 rpm at room temperature (RT) (22 ± 3˚C) and were followed by three washing steps with PBS. Briefly, 100 µL of 58.2 nM NT-proBNP, proBNP, BNP, ANP, CNP, or hCG in PBS were incubated for 14 h at 4 ˚C without shaking in a high-binding microtiter plate. Second, the wells were blocked by adding 400 µL of 2% (w/v) casein solution in PBS for 30 min without shaking. Third, 100 µL of 6.7 µM of 13G12 Ab were added to each well and incubated. The same process was carried out with the 15C4 Ab. Fourth, 100 µL of 6.7 µM SAb (the secondary Ab) were added to each well and incubated. Finally, 100 µL of the 1-Step Ultra TMB-ELISA Substrate solution were

added and 50.0 µL of 2 M H_2SO_4 were used to quench the reaction after it reached the desired color intensity (~3 min), and then the absorbance was measured at 450 nm. The degree of cross-reactivity was determined quantitatively. That is, if the Abs were cross-reactive with the different targets on the plate, a color change would be observed. Positive controls were also performed to ensure all the assay components were functioning properly. Specifically, hCG and CNP were detected using an anti-hCG or anti-CNP Ab, respectively (Figure 4.1).

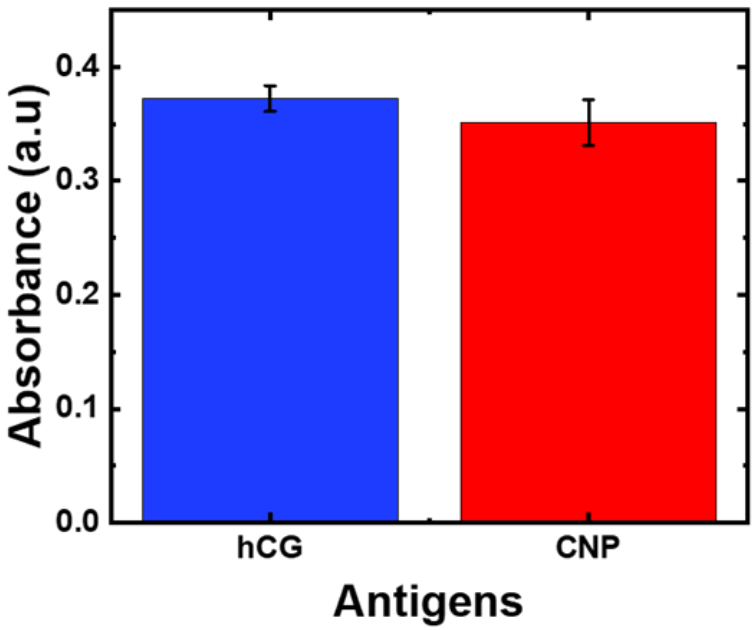

Figure 4.1 Enzyme-linked immunosorbent assay (ELISA) results obtained by forming a half indirect ELISA with human chorionic gonadotropin (hCG) or C-type natriuretic peptide (CNP) and their appropriate monoclonal Abs. This experiment was performed similarly to those described in the Experimental Section. Specifically, all the incubation steps were performed at room temperature (RT) (22 ± 3 °C) for 30 min at 600 rpm, and then were followed by washing three times with 1x phosphate buffered saline (PBS). This experiment was carried out by first immobilizing the antigens by adding 100 µL of 58.2 nM of hCG or CNP to the wells of a microtiter plate. Second, 100 µL of 6.7 µM of monoclonal anti-hCG or monoclonal anti-CNP were added. Third, 100 µL of 6.7 µM of the HRP-labeled polyclonal secondary Ab were added to each well. Finally, 100 µL of the 1-Step Ultra TMB-ELISA Substrate solution were added and 50.0 µL of 2.0 M H_2SO_4 were used to quench the reaction after it reached the desired color intensity (~3 min). These results show that for both hCG and CNP, a color change was detected, confirming that the immobilized model cross-reactants described in this chapter are functioning properly.

A complementary cross-reactivity experiment, similar to that described in the previous paragraph, was also performed. In this case, a full capture ELISA for NT-proBNP was prepared in the presence of all the potentially cross-reactive species. Specifically, this experiment was carried out by first immobilizing the anti-NT-proBNP capture Ab by adding 100 µL of 6.7 µM of the 15C4 Ab to the wells of a microtiter plate. Next, a 100 µL mixture containing 58.2 nM of each of the following was introduced: NT-proBNP, BNP, CNP, and ANP. Next, 100 µL of 6.7 µM 13G12-HRP detection Ab were added to each well. Finally, 100 µL of the 1-Step Ultra TMB-ELISA Substrate solution were added and 50.0 µL of 2 M H_2SO_4 were used to quench the reaction after it reached the desired color intensity (~3 min). The blank for this experiment was prepared following the same procedure, however, SBB was added to the wells in place of the antigen mixture.

An advantage of the Abs used for this assay is that they target amino acids at the ends of the NT-proBNP peptide. This is important, because post-translational modifications of peptides, such as glycosylation, can hinder the ability of Abs to recognize a specific target. Indeed, endogenous NT-proBNP is known to have several locations on its amino acid sequence where glycosylation occurs. These regions are amino acids located in

the middle of the peptide: amino acids 28-60.[182] These regions are avoided by the Ab pair used in this study.[147,183]

4.3.6 Preparing assay components

The 13G12 Ab was conjugated to the AgNPs using a previously published protocol, and a more detailed version can be found in the Appendix (A3).[47,48] Briefly, the 13G12 Ab was modified by bioconjugating it to a HBCL. The modified Ab was then added to 500 µL of AgNPs (4.9 x 10^{11} AgNPs/mL) and incubated for 1 h, followed by back-filling with mPEG-SH for 20 min at 600 rpm at RT. Excess conjugation reagents were then removed by centrifugation for 30 min at 16,600 g at 4 ˚C. The formed conjugate was washed three times by centrifugation and then resuspended in 500 µL of SBB. Henceforth, this will be referred to as the AgNP-HBCL-Ab conjugate. The protocol for preparing the physisorbed conjugate (denoted as AgNP-Ab), used for comparison, is provided in the Appendix (A2).

The 15C4-biotin Ab was conjugated to streptavidin-coated MµBs using the protocol provided by the manufacturer.[184] In short, 50.0 µL of MµBs (~7–10 × 10^9 MµBs/mL) were added to a SBB-blocked tube and washed by magnetic separation four times with PBS. Next, 30.0 µL of 4.6 µM 15C4-biotin Ab and 20.0 µL of PBS were added to the tube and incubated for 30 min at 40 rpm at RT, using the tube revolver. Finally, the conjugated MµBs were

washed by magnetic separation five times with SBB and resuspended to a final volume of 50.0 µL. Henceforth, this will be referred to as the MµB-Ab conjugate. A more detailed protocol is provided in the Appendix (A4).

4.3.7 Step-wise formation of the NT-proBNP metalloimmunoassay

Once all the assay components were prepared, they were used in the full metalloimmunoassay for NT-proBNP. This assay was formed in SBB-blocked wells of a microtiter plate as follows. First, 2.0 µL of the MµB-Ab conjugate were placed in each well along with 100 µL of a known concentration of NT-proBNP in SBB. These components were incubated for 30 min at 1000 rpm at RT. Next, the partially formed assay was washed to remove unbound peptide. Washing was performed by magnetic separation wherein the MµBs were collected at the bottom of the wells, the supernatant was removed, and the half-formed conjugate was resuspended in 0.1% (v/v) Tween-20 and PBS solution. This washing step was performed three times. Next, 20.0 µL of the AgNP-HBCL-Ab conjugate and 80.0 µL of SBB were added. This mixture was incubated using the procedure stated in the previous section and then washed by magnetic separation. The fully formed assay was resuspended in a final volume of 50.0 µL of PBS and then transferred to the paper-based electrode. The MµBs were focused onto the working electrode (~30.0 s) by the magnet (Illustration 4.2), and the

electrochemical analysis was performed as discussed earlier. For experiments involving assays formed in undiluted human serum, the same protocol was followed, except the NT-proBNP samples and the assay components were diluted into serum rather than SBB.

4.4 Results and Discussion

4.4.1 Determining Ab cross-reactivity

One of the most important aspects of any bioassay is its specificity. That is, the degree to which the assay can distinguish the target molecule from all other possible components of a biological sample. In our case, other natriuretic peptides can be considered good model cross-reactants for the NT-proBNP-targeting Abs used in this study. Accordingly, we carried out two sets of cross-reactivity studies using NT-proBNP, proBNP, BNP, ANP, CNP, and hCG. The first set used an indirect half ELISA to specifically check for individual antigen cross-reactivity for each Ab of the assay, while the second set used a full capture ELISA to perform a mixed-antigen cross-reactivity experiment (described in the Experimental Section of this chapter). Briefly, for the half indirect ELISA, the model cross-reactants were immobilized in different wells of a microtiter plate, and then either the unmodified 13G12 detection Ab or the 15C4 capture Ab was added to the wells,

followed by a SAb. In the case of the mixed-antigen cross-reactivity experiment, the 15C4 capture Ab was immobilized on the plate, followed by the addition of the antigen mixture (including NT-proBNP) to the wells of the plate, and then a 13G12-HRP signaling Ab. The degree of reactivity was determined by UV-Vis spectroscopy for both experiments.

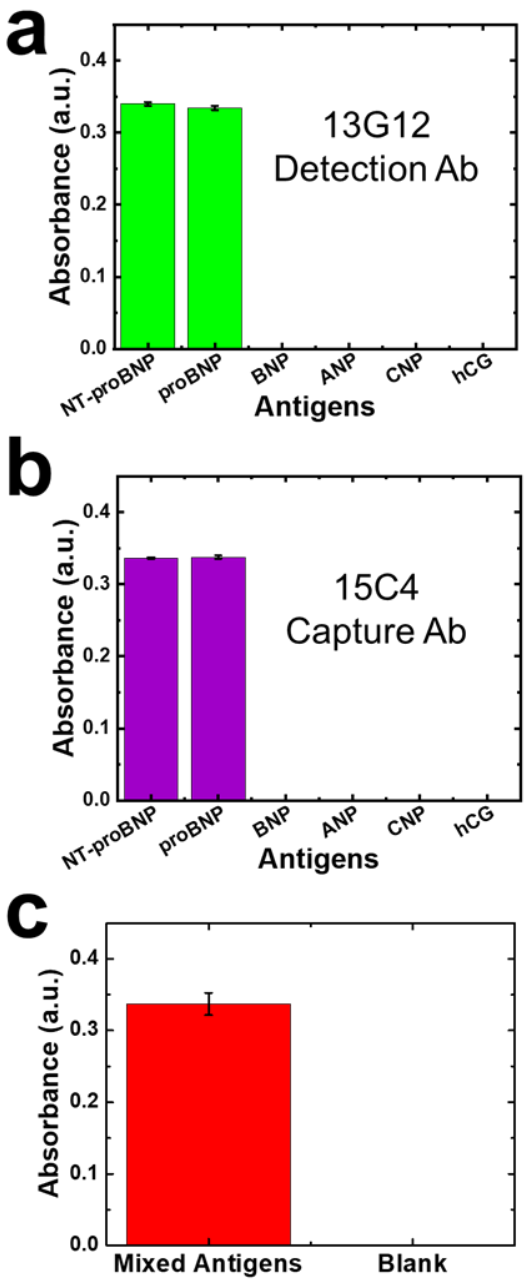

Figure 4.2 Histograms representing the cross-reactivity absorbance results obtained using an indirect enzyme-linked immunosorbent assay (ELISA). Results for the anti-NT-proBNP Ab pair including, (a) the 13G12 detection Ab and (b) the 15C4 capture Ab. (c) Full capture ELISA results from the assay prepared with a mixed antigen solution containing 58.2 nM of each of the following: NT-proBNP, BNP, CNP, and ANP, prepared in 2% (w/v) casein-PBS. The error bars represent the standard deviation of three independent measurements.

Figures 4.2a and 4.2b show the results of the foregoing experiments obtained using the 13G12 detection Ab and the 15C4 capture Ab, respectively. The histograms indicate that these two Abs are not cross-reactive with the other natriuretic peptides tested, or with hCG. A positive control experiment was also performed (Figure 4.1), which further validates this conclusion.

Figure 4.2c displays the results for the mixed-antigen cross-reactivity experiment. These results show that even in the presence of multiple antigens that are related to NT-proBNP, NT-proBNP is captured to the same degree as when the potential interferants are omitted. It is important to note that because NT-proBNP originates from proBNP, the Ab pair also recognizes proBNP (which was omitted in this mixed antigen experiment). This has little impact on the bioassay, however, because most commercial assays capture both NT-proBNP and proBNP, and the latter is almost ten times lower in concentration than NT-proBNP in HF patient samples.[146]

4.4.2 Comparing physisorbed and HBCL-modified conjugates

After ensuring that the Ab pair used for the analysis are not cross-reactive with the other tested natriuretic peptides, two different bioconjugation routes were explored to determine the best technique for immobilizing the detection Ab on the AgNP label: physisorption and HBCL modification. These experiments

were carried out by preparing both the physisorbed AgNP-Ab and the AgNP-HBCL-Ab conjugates, as described in the Experimental section, and then using them to electrochemically detect a single concentration of NT-proBNP in the full metalloimmunoassay (detection of multiple concentrations is discussed in the next section). Specifically, the metalloimmunoassay was formed with 100 µL of 0.58 nM of NT-proBNP and 2.0 µL of the MµB-Ab conjugate. The detection Ab, which was in excess, was either physisorbed to the AgNP label (AgNP-Ab conjugate) or covalently attached using the HBCL (AgNP-HBCL-Ab conjugate). After assay formation, the electrochemical protocol was executed.

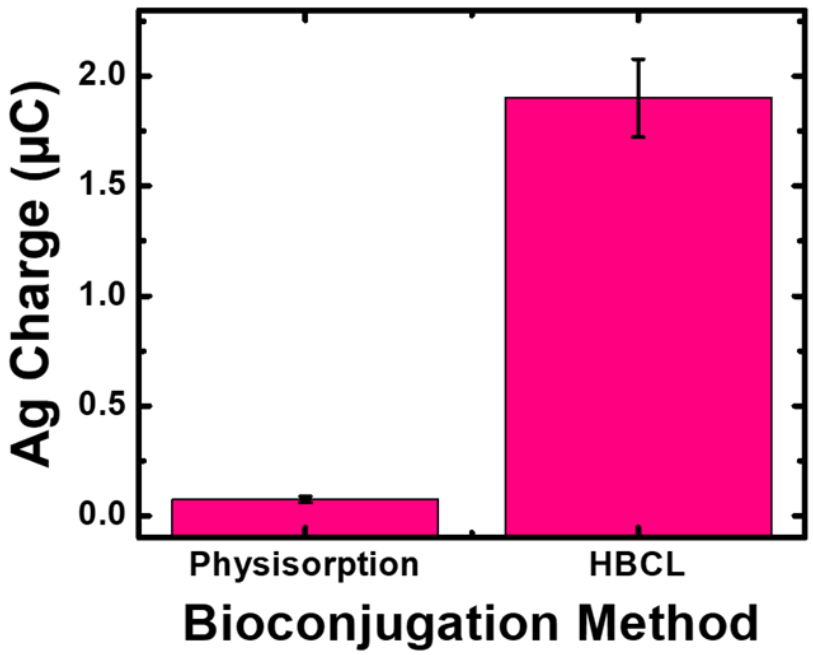

Figure 4.3 Histograms representing the amount of Ag charge obtained by forming the full metalloimmunoassay for a single concentration of NT-proBNP (0.58 nM) using either the AgNP-Ab physisorbed conjugate or the AgNP-HBCL-Ab conjugate. The electrochemical experiment was carried out in PBS. The error bars represent the standard deviation of five independent measurements performed using five independently prepared paper electrodes.

Figure 4.3 is a histogram comparing the Ag charge obtained using the two different conjugation methods. These data represent three independently prepared assays analyzed on independently prepared paper electrodes. The magnitude of the signal arising from the AgNP-HBCL-Ab conjugate is 27-fold higher than that of the AgNP-Ab (physisorbed) conjugate. Specifically, the charge arising from the AgNP-HBCL-Ab conjugate was 1.90 ± 0.18 vs. 0.07 ± 0.01 μC for the conjugate formed by physisorption. As mentioned earlier, there is a direct

correlation between the measured charge and the amount of peptide captured in the assay, which means that the HBCL leads to an increased target peptide capture and a lower limit of detection.

Physisorption is widely used in the literature as a simple means for immobilizing Abs on NP surfaces; however, this technique has limitations. As noted previously, one of these is that there is usually (but not always)[179] limited control over the orientation of the Ab on the surface of the particle. This is a consequence of the fact that conjugation by physisorption does not target a specific region of the Ab.[62] The advantage of the HBCL, and specifically the hydrazone chemistry used in this study, is that it exclusively targets the polysaccharide groups residing in the Fc region of the Ab. This ensures that the antigen-binding fragment (Fab) regions of the Ab are completely accessible to the target molecule.[106,180] Indeed, the results in Figure 4.3 suggest that the 13G12 detection Ab is more effectively oriented for capturing NT-proBNP. Additionally, we have previously shown that the Ab is also more strongly attached to the NP when the HBCL is used instead of physisorption.[180] Accordingly, the AgNP-HBCL-Ab conjugate was selected for subsequent experiments.

4.4.3 Detecting multiple concentrations of NT-proBNP

After determining that the HBCL-modified detection Ab performs better than the physisorbed AgNP-Ab conjugate, the latter was used for preparing a dose-response curve. The assay was prepared in SBB using a step-wise procedure as described in the Experimental Section. Briefly, 2.0 µL of the MµB-Ab conjugates were added to the wells of a pre-blocked microtiter plate, and then 100 µL of varying concentrations of NT-proBNP were added. Following incubation and washing, an excess of the AgNP-HBCL-Ab conjugate was added to the wells. Once the assay was fully formed, the entire content of the well was transferred to the paper electrode, and the electrochemical protocol was carried out in PBS.

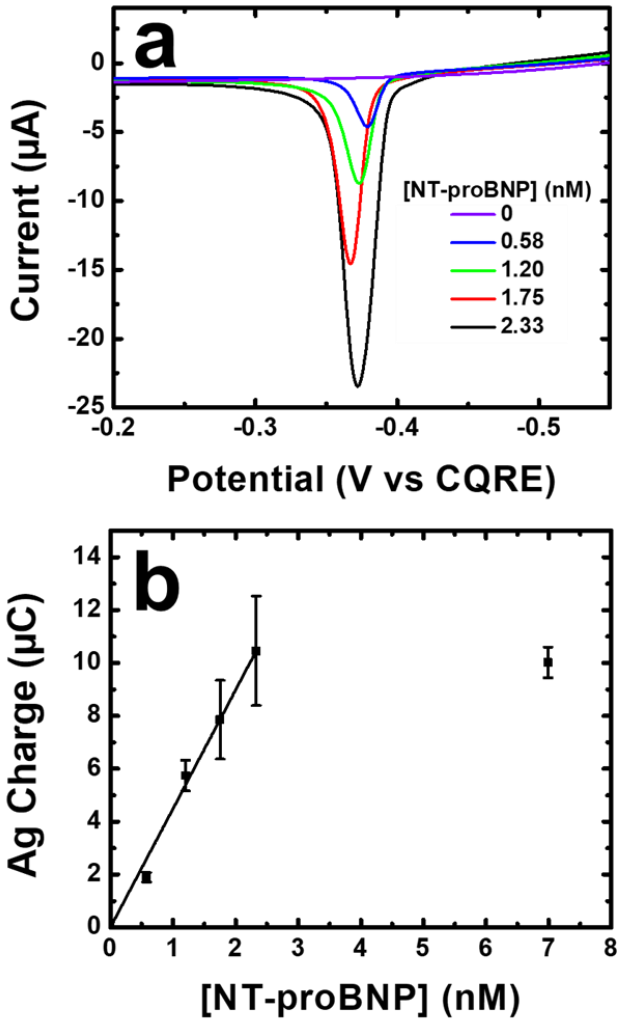

Figure 4.4 Electrochemical results for detection of NT-proBNP using the full metalloimmunoassay in PBS on a paper electrode. (a) Anodic stripping voltammograms (ASVs) for the concentrations of NT-proBNP indicated in the legend. For clarity, only one ASV trace is shown for each concentration. The position of the ASV peaks vary slightly due to the use of a carbon quasi-reference electrode (CQRE). (b) Calibration curve showing the correlation between Ag charge (obtained by integrating ASVs like those in (a)) and the concentration of NT-proBNP. Note that for clarity the ASV for 7.0 nM of NT-proBNP is not shown in (a). The linear regression value is 0.99, and the scan rate is 50 mV/s. Each data point represents the average of five measurements carried out using independently fabricated electrodes. The error bars represent the standard deviation of those five measurements. Outliers were eliminated using the Grubb's test with a 95% confidence level.

Figure 4.4 shows the results of this experiment. The voltammograms in Figure 4.4a indicate that the AgNP oxidation current increases as a function of the concentration of NT-proBNP used to form the bioassay. The charges under the voltammograms were obtained by integration, and the results for five independent experiments per concentration are plotted in Figure 4.4b. These data demonstrate that the charge increases linearly from 0.58-2.33 nM of NT-proBNP and then it begins to saturate (the data point for 12.0 nM is not shown in Figure 4.4b, but it is about the same as the point for 7.0 nM). Note that concentrations below 0.58 nM could not be differentiated from the blank and are thus not shown in Figure 4.4. An additional important feature of Figure 4.4b is that the overall relative standard deviation of this assay is <15%.

To put the linear range of the bioassay into perspective, the critical concentration used by physicians to identify HF patients who are at risk of poor outcomes is 1000 pg/mL (116 pM).[159,160] Accordingly, the results in Figure 4.4b indicate that the performance of the bioassay is approaching the risk stratification threshold. Clearly, additional work is required to further reduce the limit of detection, but to the best of our knowledge the value we have achieved thus far is the lowest

reported for detection of NT-proBNP using a simple, paper-based device.[59]

4.4.4 Forming the metalloimmunoassay in undiluted serum

The primary goal of the present chapter is to report on a bioassay that can be easily integrated into a point-of-need device. In part, this means an assay having the ability to capture NT-proBNP from a serum matrix. Accordingly, the full metalloimmunoassay for NT-proBNP was prepared exactly as described in the previous section, but in this case one set of replicates was prepared in SBB and another in undiluted human serum, both spiked with 0.58 nM NT-proBNP. The assays were formed in their respective matrixes, washed with 0.1% (v/v) Tween-20 and PBS, resuspended in PBS, and transferred to the paper-based electrodes for electrochemical detection.

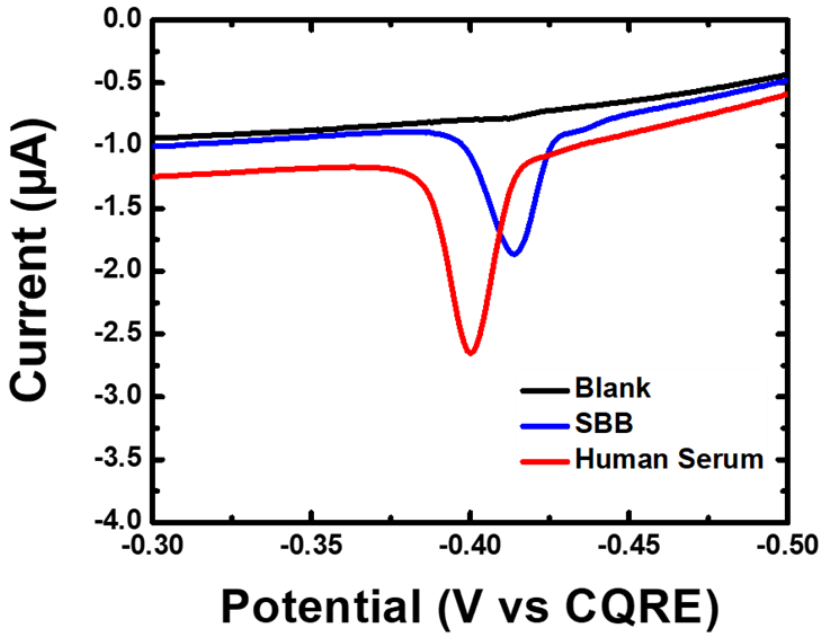

Figure 4.5 Anodic stripping voltammograms (ASVs) obtained by forming the full metalloimmunoassay for NT-proBNP in either a superblock blocking buffer matrix (SBB) or an undiluted human serum matrix. The scan rate was 50 mV/s. For clarity, only one ASV trace is shown for each conjugate, but the measurements were carried out in triplicate using independently fabricated electrodes. The position of the ASV peaks varies due to the use of a carbon quasi-reference electrode (CQRE).

Figure 4.5 displays the ASVs for the assays formed in both SBB and human serum. The blank for this experiment was the assay formed in serum with no NT-proBNP present. The Ag charge obtained from this experiment was 0.60 ± 0.10 µC, regardless of whether the assay was formed in SBB or undiluted human serum. This means that the serum matrix has no detectable adverse effects on formation of the assay.

4.5 Summary and Conclusion

To summarize, the goal of this study was to describe a bioassay that can be integrated into an electrochemical detection workflow on a paper-based, point-of-need device for the detection of NT-proBNP. The detection limit of 0.58 nM of NT-proBNP is promising at this stage for such a simple immunological sensor. Indeed, we found that a 27-fold increase in detection efficiency is observed by just improving the linking chemistry between the detection Ab and the AgNP label. We attributed this result to the controlled orientation of the detection Ab on the surface of the AgNP label.[106,180] This advance made it possible to detect NT-proBNP near the risk stratification threshold with a relative standard deviation of <15%. Additionally, using both an indirect and a full-capture ELISA, we showed that the Ab pair selected for this bioassay was not cross-reactive with other cardiac natriuretic peptides. Finally, the bioassay could be formed in undiluted human serum with no change in signal (compared to buffer).

The detection method reported in this chapter provides a simple means for detecting an important HF marker that may be relevant in the evolving at-home, personal medicine environment.[55,150,174,185] There is, however, much more work to do. Specifically, it is necessary to further lower the limit of

detection, eliminate all off-chip reagents and manipulations, and test the device using human blood samples. All of these tasks are underway in our lab, and the results will be reported in due course.

Chapter 5: Effect of Serum on Electrochemical Detection on Bioassays having Ag Nanoparticle Labels

5.1 Synopsis

The effect of serum on electrochemical detection of bioassays having silver nanoparticle (AgNP) detection labels was investigated. Both a model assay and an antigen-specific sandwich bioassay for the heart-failure marker NT-proBNP were examined. In both cases, the AgNP labels were conjugated to a detection antibody. Electrochemical detection was carried out using a galvanic exchange/anodic stripping voltammetry method in which Au^{3+} exchanges with AgNP labels. The assays were carried out using a paper-based electrode platform. The bioassays were exposed to different serum conditions prior to and during detection. There are three important outcomes reported in this article. First, both the model and antigen-specific assays could be formed in undiluted serum with no detectable interferences from the serum components. Second, to achieve the maximum possible electrochemical signal, the highest percentage of serum that can remain in an assay buffer during electrochemical detection is 0.25% when no washing is performed. The assay results are rendered inaccurate when 0.50% or more of serum is present. Third, the factors inhibiting galvanic exchange in serum probably relate to surface adsorption of biomolecules onto

the AgNP labels, chelation of Au^{3+} by serum components, or both. The results reported here provide general guidance for using metal NP labels for electrochemical assays in biofluids.*

*Chapter 5 is based on a manuscript accepted for publication: N. E. Pollok, Y. Peng, C. Rabin, I. Richards, R. M. Crooks, Effect of Serum on Electrochemical Detection of Bioassays having Ag Nanoparticle Labels. *ACS Sensors* 2021, Accepted. NEP and YP contributed equally to the work. CR assisted in data collection. IR contributed to discussion and experimental design. RCM was the research advisor. NEP, YP, and RCM wrote the manuscript.

5.2 Introduction

There are three key steps to executing a typical bioassay: capture of the analyte of interest, removal (washing) of excess reagents, and detection. At each of these steps the detection medium can either play an advantageous[186,187] or a detrimental[188] role. In the present study, we evaluated the effect of serum on a previously reported method for detecting AgNP labels that combines galvanic exchange (GE) and anodic stripping voltammetry (ASV). Illustration 5.1 illustrates the GE/ASV method. In the first step (Illustration 5.1a), Au pre-deposited onto the working electrode (WE) is oxidized and then itself oxidizes AgNPs in the vicinity of the electrode surface. During the second step (Illustration 5.1b), the resulting Ag^+ is concentrated onto the electrode surface by electrodeposition and then detected by ASV. Though we examined the effect of serum on this GE/ASV detection method, the results are generally applicable to many different types of electrochemical bioassays.

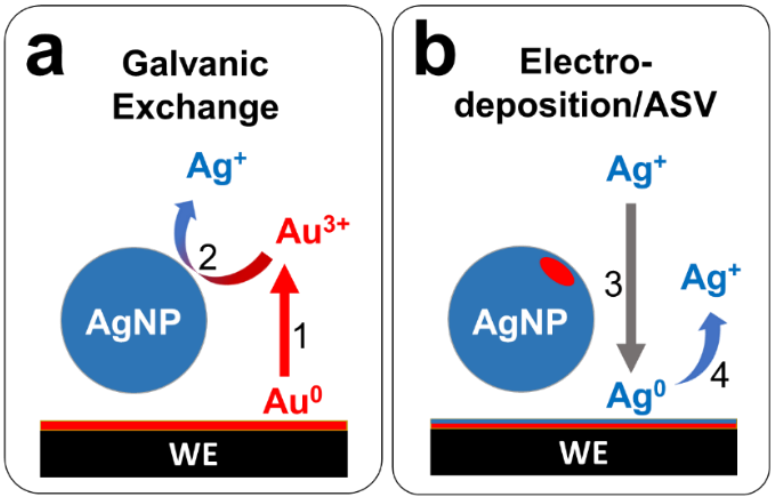

Illustration 5.1 Schematic of the galvanic exchange/anodic stripping voltammetry (GE/ASV) detection method.

Electrochemical biosensors are powerful tools used to monitor medical conditions at home,[18,19] in clinics,[20-22] and in hospitals.[23,24] Human biomarkers for point-of-care and point-of-need sensors are found in matrixes including sweat,[29,30] saliva,[26-28] and whole blood[31,32] (among others).[25] Serum is another common matrix used for bioassays. It is the fluid and solute component of whole blood that does not play a role in clotting. It includes all proteins not used in clotting, all electrolytes, antibodies (Abs), antigens, hormones, and exogenous substances.[189,190] Human serum albumin is the most abundant protein in human blood plasma, and it constitutes about 50% of the proteins in serum.[189] Due to the relatively high abundance of albumin in serum, its electrochemistry has been studied. For

example, both the oxidized and reduced forms of bovine serum albumin (BSA) exhibit reversible electron transfer when strongly adsorbed to a hanging mercury drop electrode through the interaction of exposed disulfide bonds with the mercury surface.[188]

Signal amplification is often a key component of bioassays. Amplification is usually accomplished using enzyme labels; for example, in enzyme-linked immunosorbent assays (ELISA).[55,171] Over the past 20 years, however, there has been growing interest in using metallic or semiconducting nanoparticles (NPs) for signal amplification due to their generally higher stability, lower cost, and faster read-out times.[41,54] More specifically, AgNPs and gold nanoparticles (AuNPs) conjugated to recognition elements, such as Abs,[42,57,59,142,180,191] nucleic acids,[66,95,127] or aptamers,[173] are becoming increasingly common. To ensure the stability of the metal label in complex media, many protocols include surface-modification steps; for example, addition of thiolated polyethylene glycol.[192] Furthermore, although a relatively complex matrix, serum can also work as an effective NP stabilizing agent and a conductive medium for electrochemical analysis.[33,34,186,193] In fact, in 2009, Murawala et al. described a simple and convenient one-step, room-temperature method for the synthesis of BSA-capped AgNPs and AuNPs. The resulting NPs were

easily dispersible in water and could withstand dynamic salt conditions, all of which are important characteristics of NPs used in bioassays.[33]

Previous work from our group has shown that metalloimmunoassays can be formed in undiluted human serum,[191] but that the GE/ASV detection process is inhibited. In the present chapter we aim to elucidate the factors leading to inhibition. Specifically, we will show that: (1) both a model and an antigen-specific metalloimmunoassay can be formed in serum; (2) systematic analysis of washing steps reveal the maximum amount of serum that can remain during detection to yield full recovery of the Ag signal; and (3) there are differences in detectability when serum or filtered serum are used. These findings should be of broad interest to those interested in carrying out electrochemical bioassays on analytes found in serum.

5.3 Experimental

5.3.1 Chemicals and materials

NaCl, NaOH, HCl, KNO_3, $NaIO_4$, Whatman grade 1 chromatography paper (180 µm thick, 20 cm x 20 cm sheets, linear flow rate of water = 0.43 cm/min) and siliconized low-retention microcentrifuge tubes were purchased from Fisher Scientific

(Pittsburgh, PA). $HAuCl_4$, $AgNO_3$, phosphate-buffered saline (PBS, pH=7.4, P3813), superblock blocking buffer containing PBS (SBB) (cat. no. 37515), polyoxyethylene (20) sorbitan monolaurate (Tween-20), 4-(2-hydroxyethyl)-1-piperazineethanesulfonic acid (HEPES), and bovine serum albumin (BSA) were purchased from Sigma Aldrich (St Louis, MO). Unfiltered human serum (hereafter, just "serum") was purchased from Millipore-Sigma (Taunton, MA). In some cases, the human serum was filtered using 10 kDa molecular weight cut-off spin filters (also from Millipore-Sigma), and this is hereafter referred to as "filtered serum"). The 5 kDa methoxy poly(ethyleneglycol) thiol(mPEG-SH) was obtained from Nanocs (New York, NY).

Conductive carbon paste (Cl-2042) was purchased from Engineered Conductive Materials (Delaware, OH). Streptavidin-coated, 1.0 µm-diameter magnetic beads (MµBs, Dynabeads, MyOne Streptavidin T1, 10 mg/mL) were obtained from Invitrogen (Grand Island, NY). Stock citrate-capped AgNPs (nominal 20 nm diameter, 0.18 mM Ag, 4.5×10^{11} NP/mL) were purchased from nanoComposix (San Diego, CA). N-terminal prohormone brain natriuretic peptide (NT-proBNP), monoclonal immunoglobulin G anti-NT-proBNP 13G12 detection (Ab), and 15C4 capture Ab were obtained from HyTest (Turku, Finland). The biotinylated polyclonal anti-mouse immunoglobulin G secondary antibody (SAb) was obtained from

Abcam (Cambridge, UK). All solutions were made using deionized (DI) water (>18.0 MΩ-cm, Milli-Q Gradient System, Millipore, Burlington, MA). All PBS concentrations were 1X unless otherwise noted.

5.3.2 Instrumentation

The UV-vis spectroscopic measurements were performed using a Hewlett-Packard HP8453 spectrometer with a micro quartz cuvette (50 µL, Hellma, Müllheim, Germany). A tube revolver (cat. no. 88881001, Thermo Scientific) and a BioShake iQ from Quantifoil Instruments GmbH (Jena, Germany) were used for incubation steps during bioconjugation. Neodymium magnets were purchased from K&J Magnetics (Pipersville, PA) and were used for washing and separating steps involving magnetic microbeads (MµBs).

5.3.3 Electrochemistry

Electrochemical measurements were performed using a CH Instruments model 760B electrochemical workstation (Austin, TX). The fabrication of paper electrodes and electrodeposition of Au onto the WE are described in the Appendix (A1) and are based on a previous publication.[127] A previously published electrochemical protocol was used to detect the AgNP labels.[59,66,127,191] Briefly, to initiate GE, the potential of the WE was stepped from 0 to 0.80 V for 12.0 s to oxidize Au^0 to Au^{3+}. Following GE, the potential was stepped from 0 to −0.70 V for 50 s to reduce Ag^+ to Ag^0 onto

the electrode. These two steps were carried out twice, and then the potential was swept twice from −0.70 to 0.20 V at a scan rate of 50.0 mV/s to oxidize Ag^0. The charge resulting from the last ASV scan was obtained by integration and represents the output signal of the sensor. All electrochemical measurements were performed in 1× PBS, unless stated otherwise, and all potentials are reported vs. a carbon quasi-reference electrode (CQRE).

5.3.4 Preparation of assay components

The 13G12 Ab was conjugated to the AgNPs using a previously published protocol[180] that is also discussed in more detail in the Appendix (A3). Briefly, the 13G12 Ab was modified by bioconjugating it to a heterobifunctional cross-linker. The modified Ab was then added to 500 µL of AgNPs (4.9×10^{11} AgNPs/mL) and incubated for 1 h, followed by back-filling with mPEG-SH for 20 min at 600 rpm at room temperature (RT, 22 ± 3 °C). Excess conjugation reagents were then removed by centrifugation for 30 min at 16,600g at 4 °C. The formed conjugate was washed three times by centrifugation and then redispersed in 500 µL of SBB. Henceforth, this will be referred to as the AgNP–Ab conjugate.

For the model assay, the biotinylated SAb was conjugated to streptavidin-coated MµBs using the protocol provided by the

manufacturer.[184] Specifically, 100 µL of MµBs (~7–10 × 10^9 MµBs/mL) were aliquoted and washed. Washing was performed by magnetic separation wherein the MµBs were collected on the wall of the tube, the supernatant was removed, and the conjugate was redispersed in PBS. This was done three times within a SBB-blocked microcentrifuge tube. Next, 40.0 µL of 6.67 µM SAb were added and the resulting solution was incubated for 30 min at 40 rpm at RT using the tube revolver. Finally, the conjugated MµBs were washed by magnetic separation five times with 100 µL of PBS-BSA solution (1% w/v in PBS) and redispersed in a final volume of 100 µL of the PBS-BSA solution. The resulting product is referred to as MµB-SAb.

In the case of the antigen-specific assay components, the 15C4 capture Ab was biotinylated using a kit and the protocol provided by the manufacturer.[194] After biotinylating the 15C4 capture Ab, the modified Ab was then conjugated to the streptavidin-coated MµBs using the same procedure as described for the MµB-SAb, wherein 40.0 µL of the 6.67 µM biotinylated 15C4 capture Ab were incubated with 100 µL of the streptavidin-coated MµBs for 30 min at 40 rpm at RT on the tube revolver. After incubation, the conjugate was washed by magnetic separation. The resulting product is referred to as MµB-15C4.

5.3.5 Formation of the metalloimmunoassay

Following preparation of the assay components, two different metalloimmunoassay were prepared: the model assay and the antigen-specific assay. The model assay was formed by bioconjugating MμB-SAb and AgNP-Ab through the attached Abs. Specifically, 16.0 μL of the as-prepared MμB-SAb were added to 100 μL of AgNP-Ab having the desired concentration and then incubated for 1.0 h in the tube revolver at 30 rpm. The components were washed with the 0.1% (v/v) Tween-20 and PBS solution five times using magnetic separation, and then they were redispersed in 16.0 μL of PBS. This conjugate will be referred to henceforth as the MμB-AgNP model composite.

A step-wise conjugation approach was used for the antigen-specific assay. More specifically, this assay was formed in a SBB-blocked microcentrifuge tube as follows. First, 16.0 μL of the MμB–15C4 conjugate was placed in a tube along with 100 μL of a known concentration of NT-proBNP in undiluted normal serum (or PBS). These components were incubated for 30 min at 30 rpm at RT. Next, the partially formed assay was washed three times by magnetic separation with 0.1% (v/v) Tween-20 and PBS solution to remove unbound peptide. Finally, 100 μL of the AgNP–Ab conjugate were added. This mixture was incubated for 30 min at 30 rpm and was then washed by magnetic separation. The fully formed

antigen-specific assay was resuspended in a final volume of 16.0 µL of PBS.

For analysis, both the model and the antigen-specific assays were prepared in a similar way in that 2.0 µL aliquots of the desired assay were combined with 48 µL of PBS in a tube to yield a final sample volume of 50.0 µL. These diluted samples were then transferred to the paper-based electrode, the fully formed assays were focused onto the WE (~30.0 s) by the magnet, and the electrochemical procedure was performed as discussed earlier.

5.3.6 Assay washing procedures

Two washing procedures were used: (1) washing of the MµB-AgNP model composite; and (2) washing following dispersion of the formed MµB-AgNP model composite in different percentages of serum prior to electrochemical detection. The latter washing protocol is described next.

After formation of the MµB-AgNP model composite, initial electrochemical measurements were performed by dispersing 2.0 µL of the MµB-AgNP composite into 48.0 µL of the diluted serum matrix to yield a final sample volume of 50.0 µL, and a final AgNP concentration of 100 pM. The percentages of serum were 100.0%, 50.0%, 20.0%, 10.0%, 5.0%, 2.0%, 1.0%, 0.50% and 0.25%, and these serum solutions were diluted with PBS. Aliquots of

50.0 µL of these solutions were transferred onto the paper-electrode, and then the GE/ASV detection process was carried out. The first GE/ASV assay was carried out directly on these samples with no washing steps.

Following the foregoing initial electrochemical detection experiments, identical experiments were undertaken after washing. For the first washing step, the MµB-AgNP model composites were separated from the serum samples identified in the previous paragraph using a magnet. Next, they were redispersed in 50.0 µL of PBS, and then the electrochemical assay was carried out using this solution. The second and third washing steps were performed the exact same way.

5.3.7 Ag^+ electrodeposition

To better understand the impact of serum on the GE/ASV detection process, we examined the Ag^+ electrodeposition step in the presence of serum or filtered serum. The filtered serum was prepared by centrifuging 500.0 µL of serum for 10 min at 10,000 g using a 10 kDa molecular weight cut-off spin filter. The filtrate was collected and used without further treatment.

The three test solutions used in this experiment contained the following components: (1) 1.0 mM $AgNO_3$ + 0.10 M KNO_3 in DI water, (2) 1.0 mM $AgNO_3$ + 0.10 M KNO_3 in 20.0% serum diluted with DI water, and (3) 1.0 mM $AgNO_3$ + 0.10 M KNO_3 in 20.0% filtered

serum diluted with DI water. The Ag^+ electrodeposition experiments were carried out as follows. First, 50.0 µL of the desired test solution was placed on the WE. Second, the WE potential was stepped from 0 V to -0.70 V (vs. CQRE) for 50 s to reduce Ag^+ onto the electrode surface. Third, the electrodeposited Ag^0 was anodically stripped from the electrode surface for two times by scanning the potential from -0.70 V to 0.20 V at a scan rate of 50 mV/s. The ASV data obtained from the second scan was collected and used for quantification.

5.3.8 GE in bulk solution

GE of AgNPs by $HAuCl_4$ in bulk solution (no electrode) was studied by UV-vis spectroscopy. Before performing these experiments, the AgNPs were capped with mPEG-SH (hereafter referred to as Ag-mPEG) to yield AgNPs similar to those in the MµB-AgNP composite. The experiments were carried out by combining DI water, Ag-mPEG, $HAuCl_4$, and either serum, or filtered serum in a 1.5 mL microcentrifuge tube. The resulting solution were then mixed using a vortexer for ~30 s. The total volume for the solutions was 100.0 µL. The specific reagent usages for each experiment are provided in Table 5.1.

AgNPs (0.18 mM Ag atoms)	Serum (S) or filtered serum (FS)	Au^{3+} (1.0 mM)	DI Water	Notes
50.0 µL	-	-	50.0 µL	Control pair in DI water
50.0 µL	-	3.0 µL	47.0 µL	
50.0 µL	20.0 µL	-	30.0 µL	Pair in 20.0% serum
50.0 µL	20.0 µL	3.0 µL	27.0 µL	
50.0 µL	20.0 µL FS	-	30.0 µL	Pair in 20.0% FS
50.0 µL	20.0 µL FS	3.0 µL	27.0 µL	
50.0 µL	10.0 µL	-	40.0 µL	Pair in 10.0% serum
50.0 µL	10.0 µL	3.0 µL	37.0 µL	
50.0 µL	5.0 µL	-	45.0 µL	Pair in 5.0% serum
50.0 µL	5.0 µL	3.0 µL	42.0 µL	
50.0 µL	20.0 µL(10% S)	-	30.0 µL	Pair in 2.0% serum
50.0 µL	20.0 µL(10% S)	3.0 µL	27.0 µL	
50.0 µL	10.0 µL(10% S)	-	40.0 µL	Pair in 1.0% serum
50.0 µL	10.0 µL(10% S)	3.0 µL	37.0 µL	
50.0 µL	5.0 µL(10% S)	-	45.0 µL	Pair in 0.50% serum
50.0 µL	5.0 µL(10% S)	3.0 µL	42.0 µL	
50.0 µL	2.5 µL(10% S)	-	47.5 µL	Pair in 0.25% serum
50.0 µL	2.5 µL(10% S)	3.0 µL	44.5 µL	

Table 5.1 Reagents used for GE in different percentages of serum (S), filtered serum (FS), and DI water.

A series of experiments were performed in which the percentage of serum or filtered serum was varied in the presence of a constant charge equivalent ratio of $HAuCl_4$ to Ag (because we do not necessarily know the speciation of oxidized Au in solution, we hereafter refer to all forms of oxidized Au as Au^{3+}). In all cases, the extent of GE was determined by transferring a portion of each sample to a 50.0 µL cuvette having a 1.00 cm pathlength, and then analyzing the solutions by UV-vis spectroscopy.

5.4 Results and Discussion

5.4.1 Effect of serum on assay formation

A key step in biosensing is the formation of the assay, or, in other words, capture of the target molecule. Depending on the complexity of the matrix and the specificity of the capture molecules, this step can be challenging. Here, two different assays, the MµB-AgNP model composite and the antigen-specific assay for NT-proBNP, were prepared in different matrixes and then they were analyzed electrochemically. Each of the assays was formed in either PBS or serum. In all cases, the MµB-AgNP model composite contained 200 pM of AgNPs. The antigen-specific assay was prepared using a step-wise approach with 2.0 nM of NT-proBNP. Following formation of the assays, they were washed

three times as described in the Experimental Section, transferred to the paper electrode, and analyzed by GE/ASV.

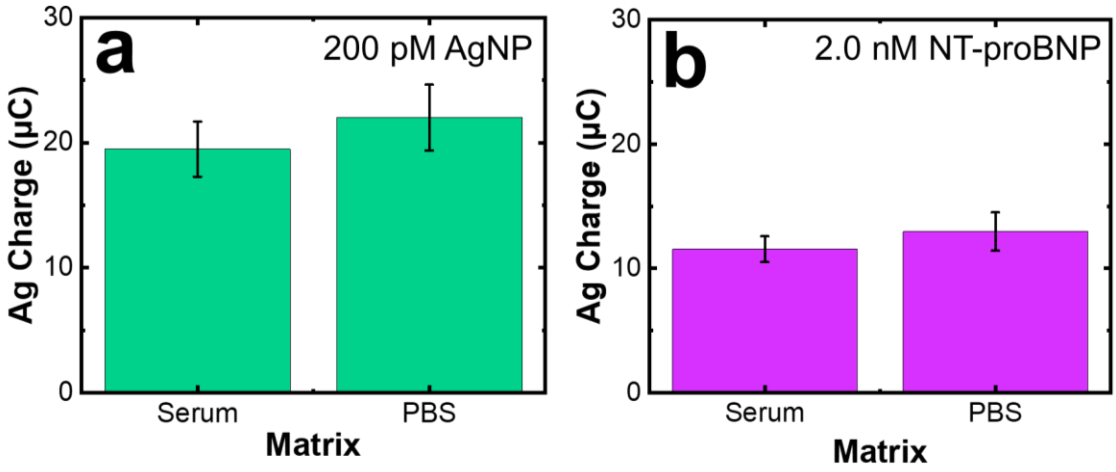

Figure 5.1 Histograms representing the Ag charge obtained when the (a) MµB-AgNP model composite (prepared using 200 pM AgNP) and (b) the antigen-specific assay for NT-proBNP (prepared using 2.0 nM NT-proBNP) were formed in either PBS or serum. Following assay formation, the samples were both washed and aliquoted, as described in the Experimental section of this chapter, and transferred to the paper-electrode for analysis in 50.0 µL of PBS. The error bars represent the standard deviation from the mean for five independent measurements.

Figure 5.1a is a histogram showing the results of the foregoing experiment for the MµB-AgNP model composite. The results clearly indicate that, within experimental error, the total charge collected for the MµB-AgNP model composite is independent of whether the assay is formed in serum or PBS. An identical conclusion obtains for the antigen-specific assay (Figure 5.1b). We conclude that that the matrix in which the assay is formed does not impact the outcome of the GE/ASV

detection method. To be clear, however, while the assays were formed in either serum or PBS, the actual electrochemical detection was carried out in aqueous PBS following washing of the assays with the 0.1% (v/v) Tween-20 and PBS.

5.4.2 Effect of serum on electrochemical detection

After confirming that the serum matrix has no detectable impact on the formation of the two metalloimmunoassays, the impact of serum on electrochemical detection was studied. In this experiment the MµB-AgNP model composite was prepared in PBS and then exposed to different percentages of diluted serum for >1 min. In all cases, the concentration of AgNPs was 100 pM. The preformed assays were then washed up to three times with PBS prior to analysis, and the resulting charge was determined using the GE/ASV method described earlier.

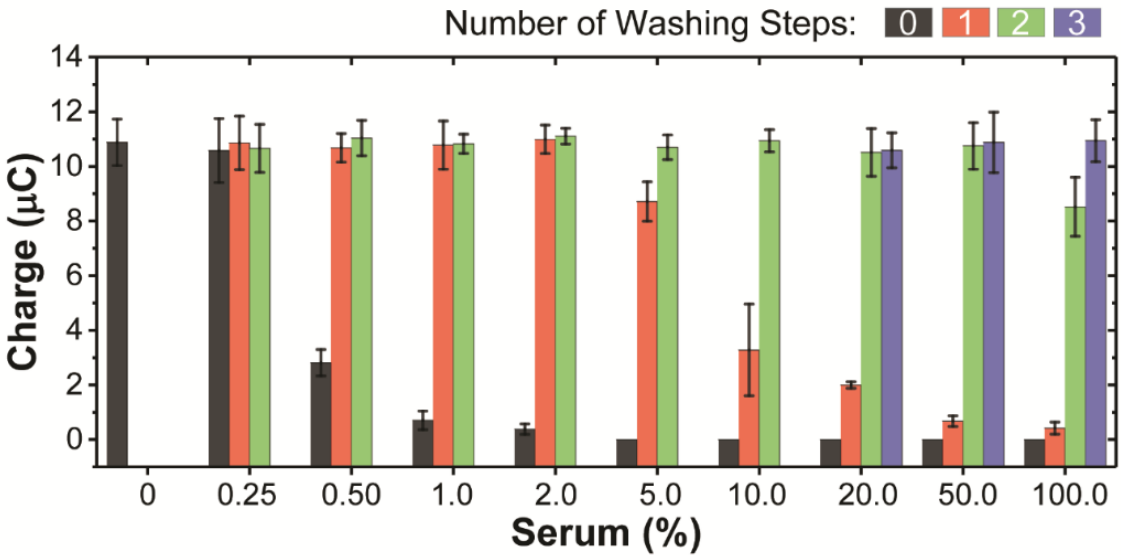

Figure 5.2 Histograms representing the amount of Ag charge collected from the preformed MµB-AgNP model composite after it was exposed to various percentages of serum for >1 min and washed 0-3 times via magnetic separation. After washing, the samples were transferred to the paper electrode and the GE/ASV detection protocol was carried out using 50.0 µL of PBS. The error bars represent the standard deviation from the mean for three independent measurements.

Figure 5.2 presents histograms showing the total charge recovered from the analysis of the MµB-AgNP model composite as a function of the number of washing steps and the percentage of serum. The black histograms correspond to the charge detected from the as-prepared model composite (no washing steps after exposure to the indicated percentages of serum). At serum percentages >5.0%, no Ag charge is detected, but for lower percentages there is a gradual increase. For the smallest percentage of serum, 0.25%, a limiting charge of 10.6 ± 1.2 µC was detected. In other words, with no washing steps included in

the protocol, the presence of even 0.50% serum renders the assay inaccurate.

The remaining histograms represent the charge recovered after the MµB-AgNP model composite was washed once, twice, or three times with PBS to remove residual serum prior to the electrochemical analysis. Specifically, after exposure to serum, 50.0 µL of the MµB-AgNP model composite was washed using magnetic separation and then redispersed in 50.0 µL PBS before electrochemical detection. The trends in Figure 5.2 are quite clear: lower percentages of serum require less washing steps to achieve limiting charge detection, and more washing steps result in detection of higher charge. In fact, three washing steps result in limiting charge detection even after the model composite is exposed to 100% serum. This same experiment was performed with two other washing buffers (1× PBS + 1.0% Tween-20 and HEPES), and in both cases the charge collected was lower than with 1× PBS only (Figure 5.3).

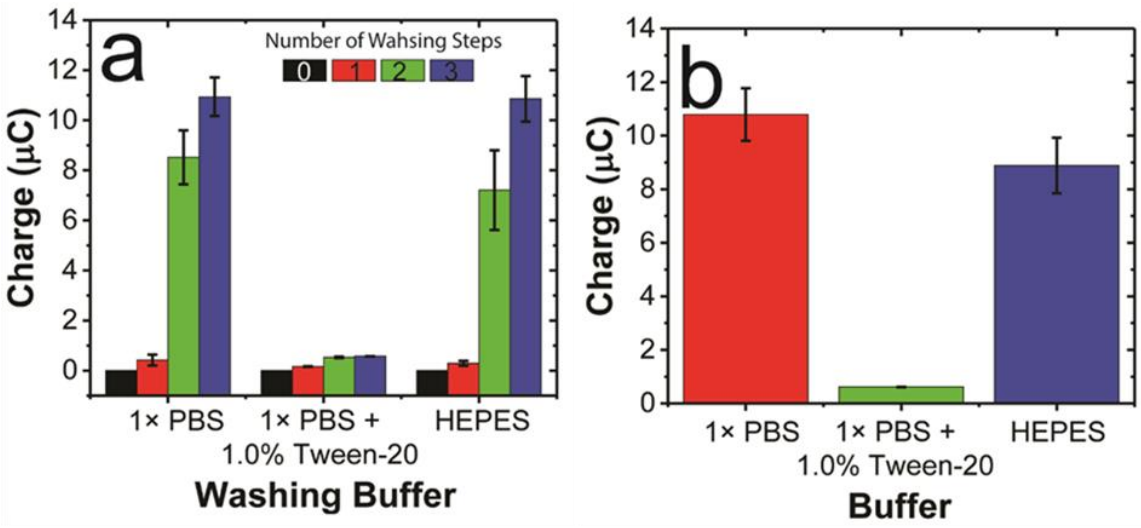

Figure 5.3 (a) Histograms representing the amount of Ag charge collected from the preformed MμB-AgNP model composite after it was exposed to 100% serum for >1 min and washed by magnetic separation 0-3 times using either 1× PBS, 1× PBS + 1.0% Tween-20, or 4-(2-hydroxyethyl)-1-piperazineethanesulfonic acid (HEPES) buffer. After washing, the samples were transferred to the paper electrode and the GE/ASV detection protocol was carried out using 50.0 μL of 1× PBS. (b) Histograms representing the amount of Ag charge collected when the preformed MμB-AgNP model composite was not exposed to serum. In this case the GE/ASV detection protocol was carried out in 50.0 μL of either 1× PBS, 1× PBS + 1.0% Tween-20, or HEPES. The results indicate that Tween-20 significantly suppresses electrochemical detection. The error bars for all data represent the standard deviation from the mean for three independent measurements.

On the basis of the foregoing results, we conclude that even after exposure to relatively small amounts of serum, limiting charge detection cannot be obtained in the absence of washing. The question then remains: what exactly is the effect of serum on the GE/ASV electrochemical detection method and, by extension, other electrochemical detection methods?

5.4.3 Effect of serum on Ag^+ electrodeposition

Inhibition of electron and mass transfer by biofilms is a common problem in biosensing applications,[195,196] although there are some notable exceptions.[197–200] Accordingly, we evaluated the effect of serum on the GE/ASV detection method by isolating the electrodeposition step. This was achieved by eliminating the analyte and AgNPs from the assay and simply carrying out Ag^+ electrodeposition in solutions containing serum. Specifically, electrodeposition was performed in bulk solutions containing 1.0 mM of $AgNO_3$, 0.10 M KNO_3, and different percentages of serum. The electrochemistry itself was carried out by stepping the WE potential from 0 V to -0.70 V for 50 s, and then the potential was swept twice from -0.70 V to 0.20 V. The second ASV was recorded and the area under the peak was integrated to determine the charge.

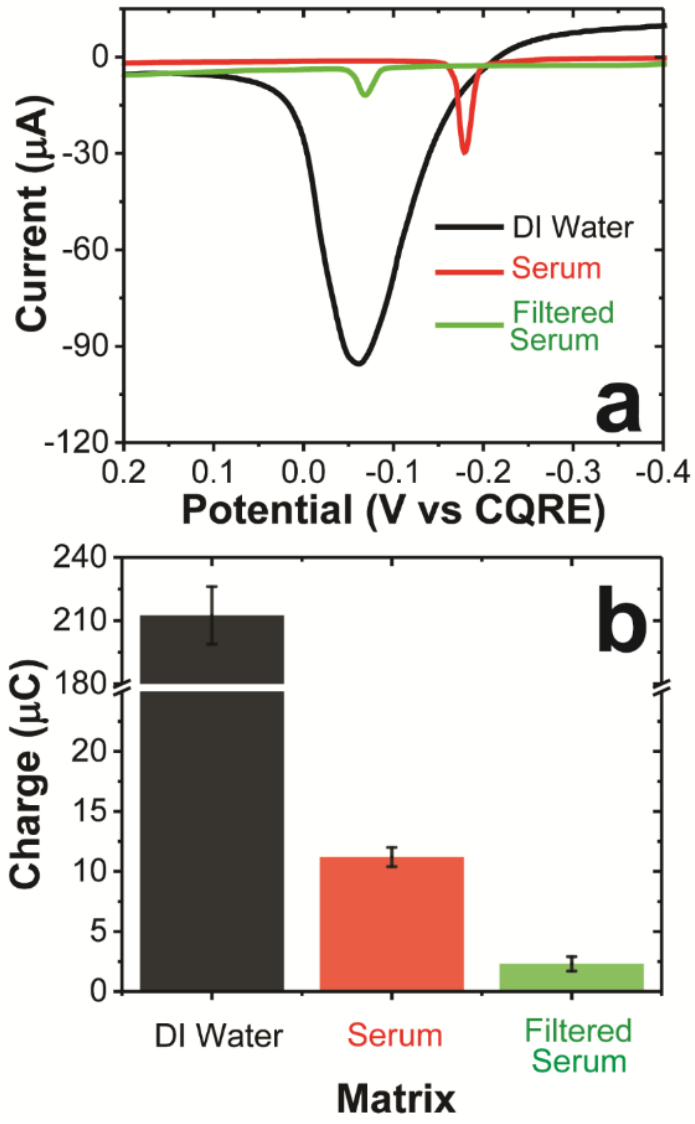

Figure 5.4 Effect of serum on Ag^+ electrodeposition. (a) ASVs obtained following electrodeposition of Ag^+ from 50.0 µL solutions (DI water, 20.0% serum, or 20.0% filtered serum) containing 1.0 mM $AgNO_3$ and 0.10 M KNO_3. Electrodeposition was carried out for 50 s at -0.70 V (vs. CQRE) on the paper-electrode platform. The ASV scan rate was 50 mV/s.(b) Histograms representing the amount of Ag charge obtained by integrating the traces in (a). The error bars represent the standard deviation from the mean for three independent measurements.

Figure 5.4a shows three representative ASV traces collected using DI water, 20.0% serum, and 20.0% filtered serum. Filtering removes components of the serum having molecular weights larger than about 10 kDa, principally, human serum albumin, globulin, and other large biomolecules. The obvious immediate observation is that even the presence of 20.0% serum dramatically reduces the ASV charge. This conclusion is reinforced by the histograms shown in Figure 5.4b, which indicate a 20-fold decrease in charge for the serum solution. As an aside, it seems counter intuitive that filtered serum would have a more dramatic effect on ASV than the serum (Figure 5.4b), and except for pointing out that this observation is reproducible we are unable to offer an explanation for this finding.

We propose that the underlying reason for the dramatic effect of serum on Ag^+ electrodeposition may relate to either of the following two factors. First, it has previously been reported that Ag^+ is chelated by albumin which is present in serum.[201] Chelation shifts the redox potential of ions to more negative potentials in proportion to the strength of binding.[65,187] A second possible effect of serum on electrodeposition relates to electrode passivation by biomolecules. Passivation can hinder electron transfer, mass transfer, or both (Figure 5.5).[35,36]

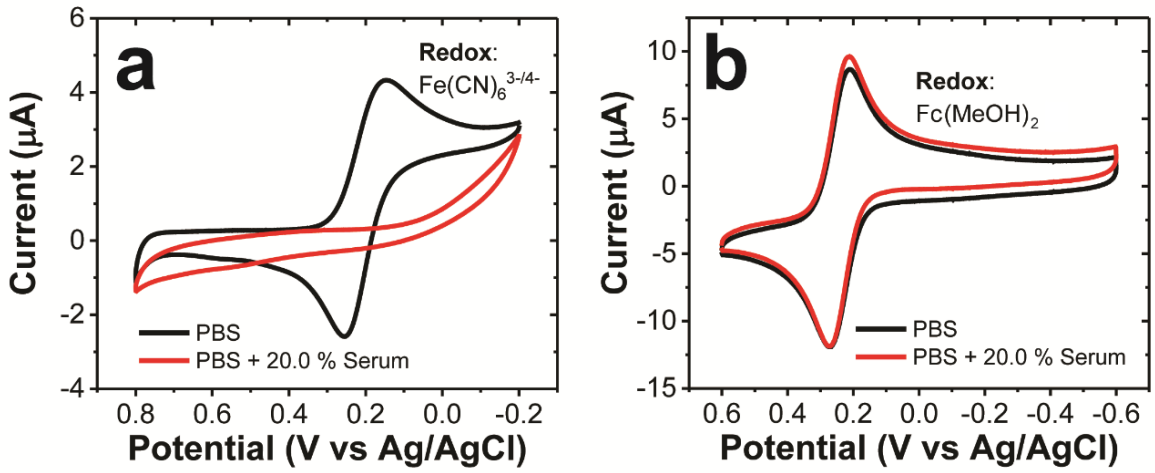

Figure 5.5 Effect of serum on mass transfer and electron transfer. (a) Representative cyclic voltammograms (CVs) collected with 1.0 mM $K_3Fe(CN)_6$ in only PBS (black trace) and in PBS plus 20.0% serum (red trace). (b) Representative CVs collected with 1.0 mM ferrocenedimethanol ($Fc(MeOH)_2$) in only PBS (black trace) and in PBS plus 20.0% serum (red trace). The working electrode was glassy carbon, the reference electrode was Ag/AgCl (sat'd NaCl), and the counter electrode was a Pt wire. The scan rate was 50 mV/s. In (a), a pair of redox peaks for $Fe(CN)_6^{3-/4-}$ were observed in PBS, but this pair of redox peaks was suppressed in the presence of 20.0% serum. Because $Fe(CN)_6^{3-/4-}$ undergoes an inner-sphere electron-transfer reaction, the redox molecule must make contact with the electrode surface. Accordingly, the absence of redox peaks in the presence of serum shows that serum inhibits mass transfer to the electrode surface.[35,36] In (b), a pair of redox peaks for $Fc(MeOH)_2$ is observed in PBS with or without 20.0% serum. Because the redox of $Fc(MeOH)_2$ is an outer-sphere electron-transfer reaction, which does not require direct contact with the electrode, the existence of the redox peaks in serum suggests that serum does not present a barrier to mass transfer to the electrode surface.[36]

5.4.4 Impact of serum on GE in bulk solution

Apart from the Ag^{+} electrodeposition step, the other important reaction in the GE/ASV detection process is GE. Therefore, in this section we examine the impact of serum on GE.

As shown in Illustration 5.1a, detection in the electrochemical assay is initiated by first generating Au^{3+} by electrooxidation of metallic Au pre-deposited on the paper electrode. Because this step is necessary for GE, we investigated it in the presence of serum first. As shown in Figure 5.6, the result is that there is no statistically significant difference in the charge recorded for Au oxidation when using PBS or PBS plus 20.0% serum. Accordingly, we conclude that serum does not affect the first step of the GE process.

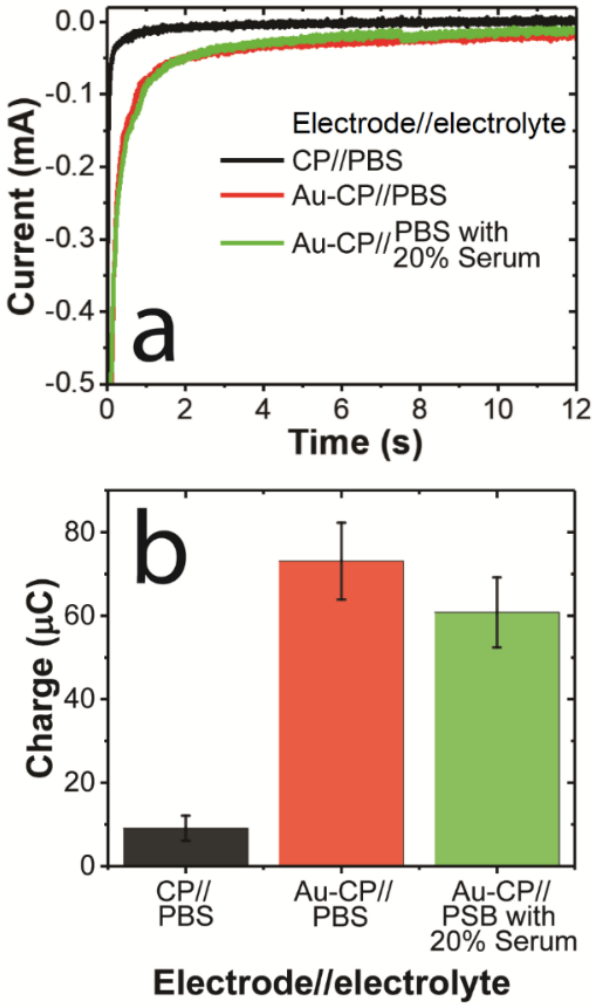

Figure 5.6 Effect of serum on the electrooxidation of Au. These experiments were carried out by stepping the potential from 0 to 0.80 V vs. CQRE for 12 s using the type of paper-based, carbon paste (CP) working electrode described in this chapter. For the data represented in the red and green traces and histograms, Au was electrodeposited onto the CP electrode prior to analysis. (a) Representative chronoamperometric curves and (b) the corresponding integrated charges. The integrated charges derived from the chronoamperometric curves are 73±9 and 61±8 µC measured in PBS only and PBS with 20.0% serum, respectively. This suggests that the presence of serum has no significant impact on Au electrooxidation. The error bars represent the standard deviation from the mean for three independent measurements.

After determining that the Au^{3+} electrogeneration step is unhindered by serum, the GE reaction between Au^{3+} and Ag-mPEG was analyzed in bulk solution (Illustration 5.1a). Ag-mPEG was used as the model AgNP label because of its similarity to the Ag labels in the MµB-AgNP model composite. Recall, that in this composite the Ab-modified AgNPs are back-filled with mPEG-SH to improve NP stability. Accordingly, the only difference between Ag-mPEG and the AgNP-Ab bioconjugate is the presence of the MµBs and the Abs present in the latter.

The GE experiments were performed by combining DI water; Ag-mPEG; Au^{3+}; and serum, or filtered serum in a microcentrifuge tube and vortexing for ~30 s. Following mixing, the solutions were analyzed by UV-vis spectroscopy. It should be noted that Au^{3+} was introduced into the system with increasing equivalents of charge. For example, one charge equivalent of Au^{3+} corresponds to 3.00 nmol of Au atoms for every 9.00 nmol of Ag atoms.

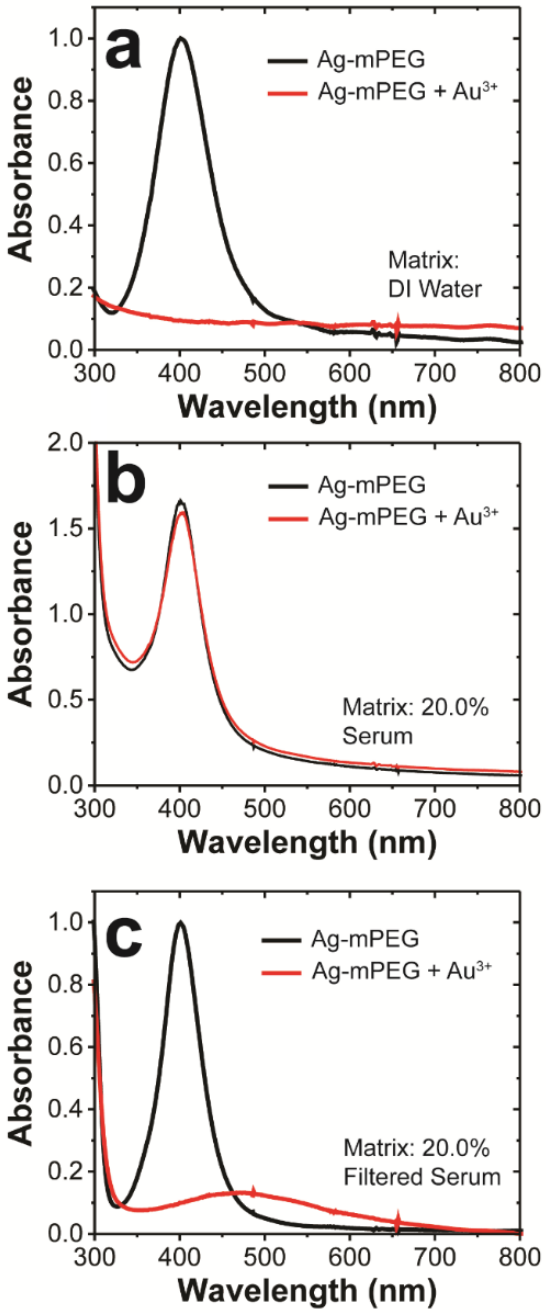

Figure 5.7 Representative UV-vis spectra of Ag-mPEG before (black trace) and after (red trace) the addition of about one charge equivalent of Au^{3+} relative to Ag in (a) DI water, (b) 20.0% serum, and (c) 20.0% filtered serum. The peak at ~400 nm is due to the SPR of AgNPs.

The black trace in Figure 5.7a is an absorbance spectrum of Ag-mPEG in DI water. It exhibits an SPR peak at ~400 nm arising from the AgNPs. When one charge equivalent of Au^{3+} is introduced into this solution, the red trace results after just 1 min. The loss of the SPR peak indicates that Ag-mPEG was converted to Ag^{+} via GE. One might expect the presence of a new AuNP SPR peak in the red spectrum following GE, and in fact a peak at 535 nm does emerge after 4 h (Figure 5.8).

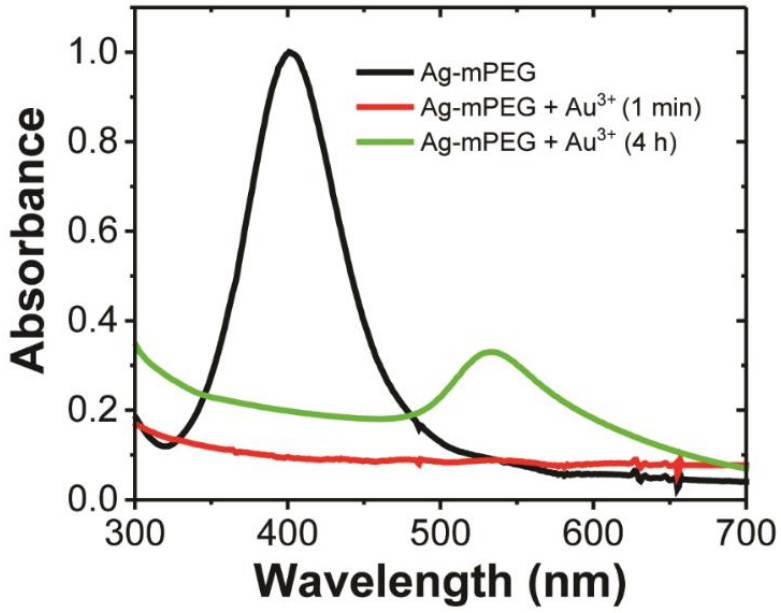

Figure 5.8 Representative UV-vis spectra of Ag-mPEG (black traces) and upon the addition of one charge equivalent of Au^{3+} in DI water collected after ~1 min (red trace) and ~4 h (green trace).

When the foregoing experiment is carried out in a matrix containing 20.0% serum instead of DI water (Figure 5.7b), there is no change in the absorbance of the SPR peak following the addition of Au^{3+}. This finding indicates that even 20.0% serum completely inhibits GE. The results of additional experiments in which the percentage of serum was varied are presented in Figure 5.9. These spectra show that even 2.0% serum partially inhibits GE.

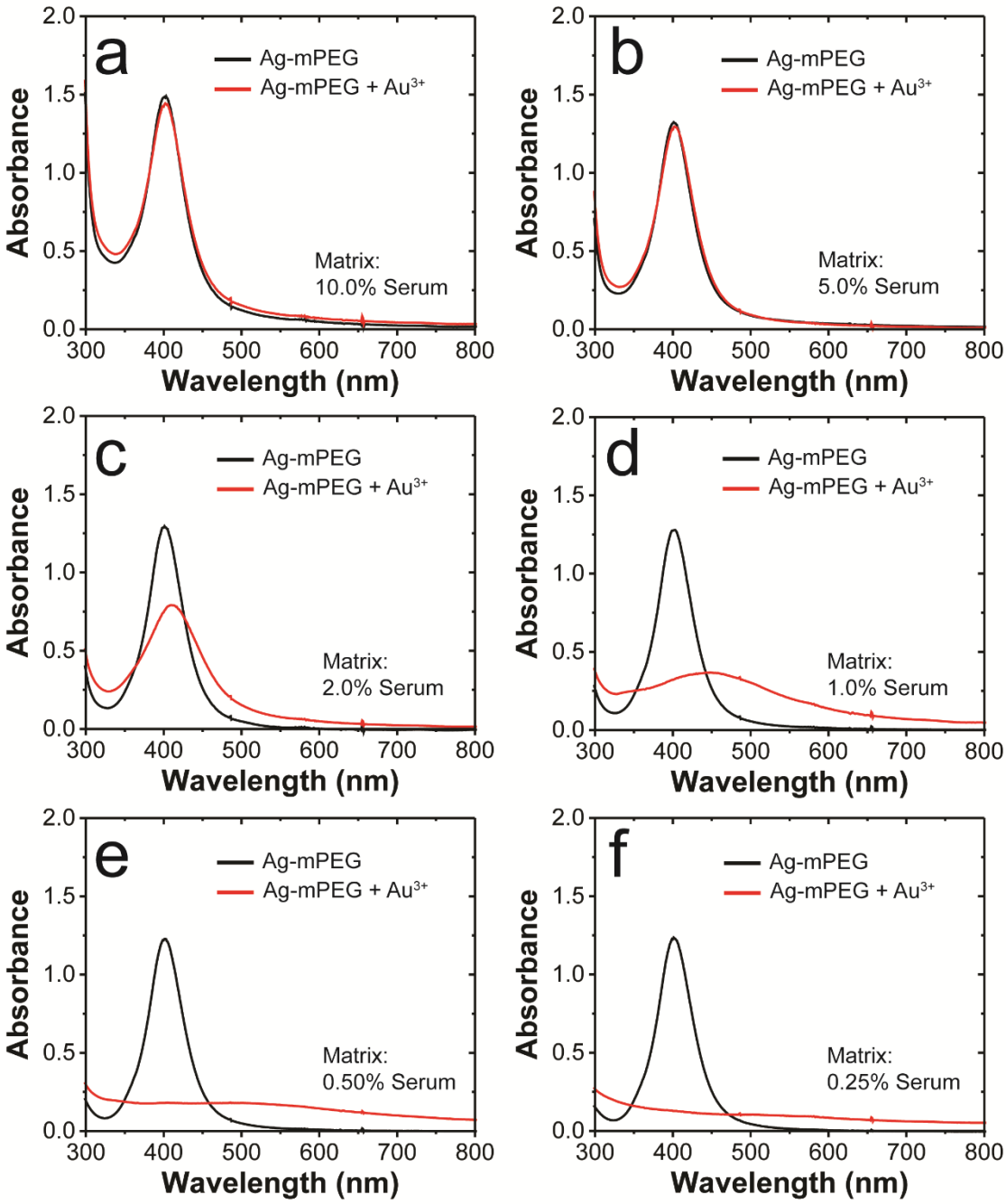

Figure 5.9 Representative UV-vis spectra of Ag-mPEG (black traces) and upon the addition of one charge equivalent of Au^{3+} (red traces) in solutions containing different percentages of serum. (a) 10.0%, (b) 5.0%, (c) 2.0%, (d) 1.0% and (e) 0.50% and (f) 0.25%.

Interestingly, as shown in Figure 5.7c, when the serum was filtered through a 10 kDa molecular weight cut-off filter, the intensity of the peak decreased by 87% indicating that the extent of GE is only slightly affected in this case. This indicates that biomolecules having molecular weights >10 kDa are principally responsible for inhibition of GE. In addition to the decrease in the magnitude of the absorbance peak, the peak position shifts from ~400 nm to ~480 nm. This change suggests that the products of the GE may be different depending on whether the reaction is carried out in 20.0% filtered serum or DI water.[202]

Taking into account the foregoing discussion, we conclude there are two possible explanations for the inhibition of GE by serum. First, biomolecules may adsorb to the surface of the Ag-mPEG NPs and prevent penetration by Au^{3+}, thereby inhibiting GE by limiting mass transfer. The second possibility is that biomolecules present in serum chelate Au^{3+}, which would shift its redox potential into a regime that hinders GE.[65,187] At present we are unable to determine if one or both of these mechanisms is responsible for suppression of GE.

5.5 Summary and Conclusion

To summarize, the goal of this study was to determine the effect of serum on electrochemical bioassays that use AgNPs as detection labels. Using a GE/ASV detection method previously developed in our group,[66] we confirmed that both a model and an antigen-specific assay for NT-proBNP could be formed in undiluted serum with no detectable adverse effects from the matrix. In addition to assay formation, we also performed a systematic analysis of the washing steps. This part of the study revealed that there is a high degree of signal inhibition in the absence of washing if even 0.50% of serum remains in solution.

Inhibition of electron and mass transfer by biofilms is a common issue in biosensing applications, and therefore this study offers generally useful insights into how this problem affects electrochemical detection of NP labels. Accordingly, the results are likely to be valuable to many in the field of chemical sensing. The findings described here will be applied to the ongoing development of a biosensor for heart failure that is currently underway in our lab. The results of that work will be reported in due course.

Chapter 6: Dual-Shaped Silver Nanoparticle Labels for Electrochemical Detection of Bioassays

6.1 Synopsis

In this chapter we demonstrate the use of dual-shaped silver nanoparticles (AgNPs) as detection labels for electrochemical bioassays. The key finding is that by using AgNP labels having two different shapes simultaneously, the limit of detection (LOD) for the assays is lowered compared to using either of the two shapes separately. The two shapes were silver nanocubes (AgNCs) having edge lengths of 40 ± 4 nm and spherical AgNPs (sAgNPs) having diameters of 20 ± 3 nm. Two different bioassays were examined. In both cases the Ag labels were functionalized with antibodies. In the one assay, the labels are directly linked to a second antibody immobilized on magnetic beads. In the second assay, the antibodies on the AgNP labels and the antibodies on the magnetic beads are linked via a peptide. The peptide is N-terminal prohormone brain natriuretic peptide (NT-proBNP), which is a heart failure marker. The efficacy of the two electrochemical assays as a function of the ratio of the two labels was investigated using a galvanic

exchange/anodic stripping voltammetry method. The key finding is that by optimizing the ratio of the two types of AgNP labels, it is possible to decrease the LOD of the assays without compromising the dynamic range compared to using either of the two labels independently. This made it possible to achieve the clinically relevant range for NT-proBNP analysis used by physicians for heart failure risk stratification.*

*Chapter 6 is based a manuscript in preparation: N. E. Pollok, Y. Peng, C. Walgama, I. Richards, R. M. Crooks, Dual-Shaped Silver Nanoparticle Labels for the Electrochemical Detection of Bioassays via Galvanic Exchange, *ACS Sensors* (in preparation). NEP designed the experiments, collected, and analyzed the data. YP performed synthesis. CW collected data. IR contributed to the generation of ideas and experimental design. RMC was the research advisor. NEP and RMC wrote the manuscript.

6.2 Introduction

Here, we report on the simultaneous use of two different Ag nanoparticle (NP) shapes as detection labels for electrochemical bioassay signal amplification. The two shapes, cubes (AgNCs) and spheres (sAgNPs), are responsive to different concentration ranges of the assay. Accordingly, the novelty of this work is that by combining the two shapes into a single assay, the dynamic range is expanded compared to using either of the two shapes individually. Specifically, both NPs were functionalized with a monoclonal antibody and tethered to a magnetic microbead (MμB) surface prior to electrochemical detection. Using a previously reported galvanic exchange and anodic stripping voltammetry (GE/ASV) detection method,[127] the optimal ratio of these particles on the MμB surface was systematically investigated.

Compared to a single label, simultaneous use of both the sAgNP and AgNC labels leads to the following results. First, there is a three-fold decrease in the limit of detection (LOD) for a model immunoassay. Second, the total amount of Ag charge collected increases by 20%. Third, the LOD for a metalloimmunoassay for the heart failure

biomarker N-terminal prohormone brain natriuretic peptide (NT-proBNP) decreases by an order of magnitude. This decrease results in the metalloimmunoassay overlapping with the clinically relevant concentration range and risk stratification threshold for NT-proBNP.[159–162] This latter goal could not be achieved using either of the two AgNP shapes individually.[191]

NPs differing in composition,[203,204] size,[205] shape,[206] and surface modifications[207–209] have been applied to a variety of assays and bioassays.[191,59,210] Due to their robust characteristics, the optical,[107,113,118,119] magnetic,[211] and electrochemical[57–59,191,207] properties of metal NPs have been utilized for immunological assays in the biosensor field in place of the more common enzymatic,[55,171] fluorescent,[13] and radioactive[212] labels.[213,214] Gold NPs are the most commonly used metallic labels for bioassays, primarily due to their stability and their desirable optical properties.[215–218] While AgNPs also have useful optical properties, they are significantly less stable than AuNPs.[66] This is a consequence, in part, of the fact that Ag has a much lower standard potential (E° = 0.79 V) than Au (E° = 1.52 V).[65] For many applications, this large difference in standard

potentials is a drawback, but as we have shown previously it can also be an advantage.[59,66,127]

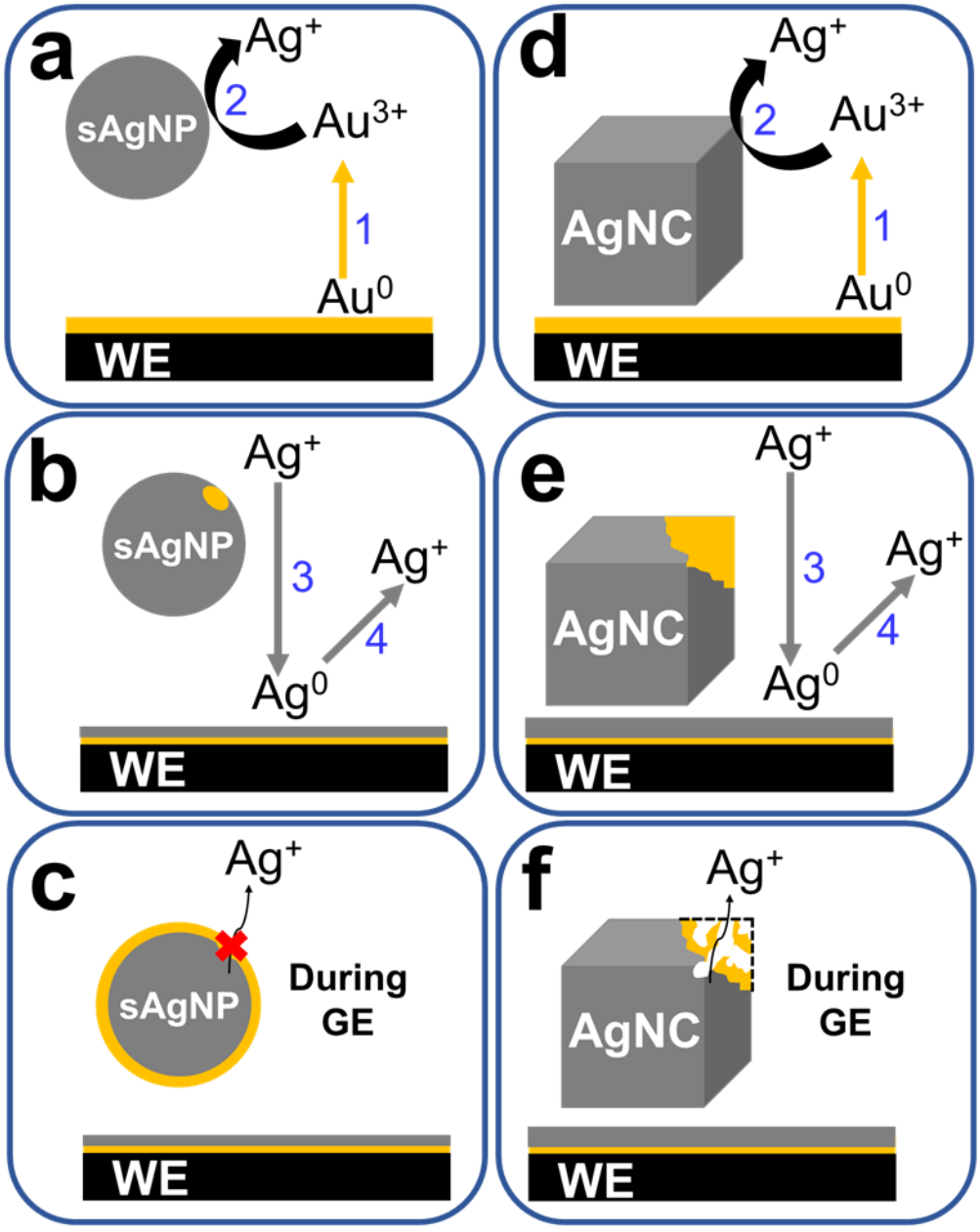

Illustration 6.1 Schematic of the galvanic exchange/anodic stripping voltammetry (GE/ASV) detection method involving (a-c) sAgNPs or (d-f) AgNCs.

Our group has previously combined GE with ASV to detect the heart failure marker NT-proBNP using sAgNPs.[191,59] Illustration 6.1a-c displays how sAgNP labels are detected in these studies. As shown in Illustration 1a, metallic Au pre-deposited on the detection working electrode (WE) is first oxidized. The resulting Au^{3+} (here representing all species of oxidized Au) diffuses to the sAgNPs and partially oxidizes them to Ag^{+} by GE. Next, as shown in Illustration 6.1b, the resulting Ag^{+} is electrodeposited onto the surface of the WE. This can be thought of as a preconcentration step. Finally, the surface-bound Ag is electrochemically oxidized by ASV. The charge resulting from the ASV step corresponds to the detection signal. The GE step is essential in this approach because the distance between the sAgNP labels (which are linked to the ~1.0 µm-diameter MµBs) and the WE, precludes direct oxidation of the sAgNPs. A intrinsic drawback of the GE process is that, depending on their size, a Au shell may form around the sAgNPs thereby preventing complete oxidation (Illustration 6.1c).[219,220]

In an effort to circumvent the foregoing partial sAgNP oxidation problem, and thereby lower the LOD for GE/ASV

assays, we recently introduced the idea of replacing sAgNPs with AgNC labels.[221] AgNCs are known to form a more porous Au shell during GE with Au^{3+} (Illustration 6.1d-f),[79,82,90,222,223] and we reasoned that this would result in a higher ASV charge and thus a lower LOD for the NT-proBNP assay. Illustration 6.1c-f shows the general conclusions from these earlier reports as they relate to the present study. Comparison of Illustration 6.1c and 6.1f demonstrates the key point: GE is prematurely terminated by formation of the Au shell in Illustration 6.1c, but the porous Au shell of the AgNCs (Illustration 6.1f) permits more complete GE.[79,82,84,90,221,223]

In this chapter, a combination of AgNC and sAgNP labels were used to detect both a model assay and an antigen-specific assay for NT-proBNP. As alluded to earlier, previous results from our lab showed that sAgNP labels yield a broad dynamic range but an insufficient lower LOD for this assay.[191,59] Conversely, AgNC labels result in a limited dynamic range but a superior LOD. Accordingly, we hypothesized that by combining the two types of NPs it would be possible to access the clinically relevant range for NT-proBNP detection.[159–162] The key point

is that this hypothesis is proven correct by the results presented herein.

6.3 Experimental

6.3.1 Chemicals and materials

NaCl, NaOH, HCl, KNO_3, $NaIO_4$, ethylene glycol (EG), sodium citrate, Whatman grade 1 chromatography paper (180 µm thick, 20 cm x 20 cm sheets, linear flow rate of water = 0.43 cm/min) and siliconized low-retention microcentrifuge tubes were purchased from Fisher Scientific (Pittsburgh, PA). $HAuCl_4$, $AgNO_3$, phosphate-buffered saline (PBS, pH=7.4, P3813), NaSH, CF_3COOAg, superblock blocking buffer containing PBS (SBB) (cat. no. 37515), polyvinylpyrrolidone (PVP, MW~55,000 g/mol), and polyoxyethylene (20) sorbitan monolaurate (Tween-20) were purchased from Sigma Aldrich (St Louis, MO). The 5 kDa methoxy poly(ethyleneglycol) thiol(mPEG-SH) was obtained from Nanocs (New York, NY).

All solutions were made using deionized (DI) water (>18.0 MΩ-cm, Milli-Q Gradient System, Millipore, Burlington, MA). The PBS concentrations were 1X unless otherwise noted. Conductive carbon paste (Cl-2042) was purchased from Engineered Conductive Materials (Delaware,

OH). Streptavidin-coated, 1.0 µm-diameter magnetic beads (MµBs, Dynabeads, MyOne Streptavidin T1, 10 mg/mL) were obtained from Invitrogen (Grand Island, NY). Stock citrate-capped sAgNPs (nominal 20 nm diameter, 0.18 mM Ag, 4.5×10^{11} NP/mL) were purchased from nanoComposix (San Diego, CA). The biotinylated polyclonal anti-mouse immunoglobulin G secondary antibody (SAb) was obtained from Abcam (Cambridge, UK). N-terminal prohormone brain natriuretic peptide (NT-proBNP), monoclonal immunoglobulin G anti-NT-proBNP 13G12 detection (Ab), and 15C4 capture Ab were obtained from HyTest (Turku, Finland).

6.3.2 Electrochemistry

Electrochemical measurements were performed using a CH Instruments model 760B electrochemical workstation (Austin, TX). The fabrication of paper electrodes and electrodeposition of Au onto the WE are provided in the Appendix (A1) and are based on methods described in a previous publication.[127] A previously published electrochemical protocol was used to detect the AgNP labels.[59,66,127,191] Briefly, to initiate GE, the potential of the WE was stepped from 0 to 0.80 V (all potentials are vs. a carbon quasi-reference electrode, CQRE) for 12.0 s to

oxidize Au^0 to Au^{3+}. Following GE, the potential was stepped from 0 to −0.70 V for 50 s to reduce Ag^+ to Ag^0 onto the electrode. These two steps were carried out twice, and then the potential was swept twice from −0.70 to 0.20 V at a scan rate of 50.0 mV/s to oxidize Ag. The charge resulting from the last ASV scan was obtained by integration and represents the output signal of the sensor. All electrochemical measurements were performed in 1X PBS unless stated otherwise.

6.3.3 Preparation of the Ag-Ab conjugates

The 13G12 Ab was conjugated to the sAgNPs and AgNCs using previously published protocols.[180,221] Briefly, the 13G12 Ab was bioconjugated to a heterobifunctional cross-linker (HBCL). The modified Ab was then added to 500 µL of sAgNPs (4.9×10^{11} sAgNPs/mL) and incubated for 1 h, followed by back-filling the AgNP surface with mPEG-SH for 20 min at 600 rpm at room temperature (RT, 22 ± 3 °C). Excess conjugation reagents were then removed by centrifugation for 30 min at 16,600g at 4°C. The formed bioconjugate was washed three times by centrifugation and then redispersed in 500 µL of SBB. Henceforth, this will be referred to as the sAgNP–Ab conjugate.

The procedure for synthesizing the AgNCs is provided in the Appendix (A5).[221] The AgNC-Ab conjugates were prepared as follows. First, the AgNCs were washed with a Tween-20 solution (0.01% w/v in water) by centrifugation at 12,000g and then dispersed in a Tween-20 solution. Second, 500 μL of a AgNC solution (6.02×10^{10} particles/ mL) was added to 25.0 μL of 1.33 μM HBCL-modified Ab and incubated for 1 h in the dark. Third, excess reagents were removed by centrifugation for 25.0 min at 12,000g at 4°C, and then the conjugates were resuspended in 500 μL of the Tween-20 solution.

6.3.4 Preparation of the MμB-Ab conjugates

For the model assay, the biotinylated SAb was conjugated to streptavidin-coated MμBs using the protocol provided by the manufacturer.[184] Specifically, 100 μL of MμBs (~7–10 × 10^9 MμBs/mL) were aliquoted and washed. Washing was performed using magnetic separation wherein the MμBs were collected on the wall of a SBB-blocked microcentrifuge tube with a neodymium magnet, the supernatant was removed, and the conjugate was redispersed in PBS. This process was carried out three times. Next, 40.0 μL of 6.67 μM SAb were added to the tube and the resulting solution was incubated for 30

min at 40 rpm at RT using the tube revolver. Finally, the conjugated MμBs were washed using magnetic separation five times with 100 μL of SBB and then redispersed in a final volume of 100 μL of SBB. The resulting conjugate is referred to as MμB-SAb.

For the NT-proBNP assay, the 15C4 capture Ab was biotinylated using a kit and the protocol provided by the manufacturer.[194] Next, the modified Ab was conjugated to the streptavidin-coated MμBs using the same procedure as described for the MμB-SAb, wherein 40.0 μL of the 6.67 μM biotinylated 15C4 capture Ab were incubated with 100 μL of the streptavidin-coated MμBs for 1 h at 30 rpm at RT on the tube revolver. After incubation, the conjugate was washed by magnetic separation. The resulting product is referred to as the MμB-15C4 conjugate.

6.3.5 Formation of the metalloimmunoassay

Following preparation of the assay components, two different metalloimmunoassay were prepared: the model composite assay and the NT-proBNP assay. The model composite assay was formed by bioconjugating MμB-SAb and sAgNP-Ab (or the AgNC-Ab) by interaction of the two Abs. Specifically, 16.0 μL of the as-prepared MμB-SAb were added

to 100 µL of a mixture of sAgNP-Ab and AgNC-Ab having the desired ratio and then incubated for 30.0 min in the tube revolver at 30 rpm (Table 6.1). The product of the conjugation reaction was washed with 0.1% (v/v) Tween-20 and PBS solution five times using magnetic separation, and then it was redispersed in 16.0 µL of PBS. These composites will be referred to henceforth as the MµB-sAgNP model composite when prepared with sAgNP-Ab, and the MµB-AgNC model composite when prepared with AgNC-Ab.

Desired NP Ratio	sAgNP-Ab (µL)	AgNC-Ab (µL)	Total Volume (µL)
100:0	100.0	-	100.0
0:100	-	100.0	100.0
50:50	50.0	50.0	100.0
70:30	70.0	30.0	100.0
30:70	30.0	70.0	100.0
80:20	80.0	20.0	100.0
20:80	20.0	80.0	100.0
90:10	90.0	10.0	100.0
10:90	10.0	90.0	100.0
*Initial buffer volume of MµBs (16.0 µL) was removed prior to sAgNP-Ab and AgNC-Ab additions, which left only the MµBs in the tube and an initial volume of zero.			

Table 6.1 Preparation of the different NP ratios used to form the metalloimmunoassay.

A step-wise conjugation approach was used for the NT-proBNP assay. More specifically, this assay was formed in a SBB-blocked microcentrifuge tube as follows. First, 16.0 µL of the MµB–15C4 conjugate was placed in the tube along with 100 µL of a desired concentration of NT-proBNP in SBB. These components were incubated for 30 min at 30 rpm at RT. Next, the partially formed assay was washed three times using magnetic separation with 0.1% (v/v) Tween-20 and PBS solution to remove unbound peptide. Finally, 100 µL of the desired ratio of the sAgNP-Ab and AgNC-Ab conjugates were added (Table 6.1). This mixture was incubated for 30 min at 30 rpm and was then washed using magnetic separation. The fully formed NT-proBNP assay was resuspended in a final volume of 16.0 µL of PBS.

For analysis, both the model and the NT-proBNP assays were prepared in a similar way in that 2.0 µL aliquots of the desired assay were combined with 48 µL of PBS in a tube to yield a final sample volume of 50.0 µL. These diluted samples were then transferred to the paper-based electrode, the fully formed assays were focused onto the WE (~30.0 s) by the magnet, and the electrochemical procedure was performed as discussed earlier.

6.4 Results and Discussion

6.4.1 Electrochemical analysis of the sAgNP-Ab and AgNC-Ab conjugates

The first step for comparing the efficacy of the sAgNP-Ab and AgNC-Ab conjugates was to determine a figure-of-merit that could remain constant for both of them. These two types of NPs are similar in that they are both composed of Ag and they both have HBCL-modified Abs bioconjugated to their surface. There are, however, some differences. Specifically, these NPs differ in size (20 vs. 40 nm diameter for sAgNP and AgNC, respectively), surface ligands (PEG vs. PVP for sAgNP and AgNC, respectively), and GE efficiency. Accordingly, the best figure-of-merit is the total Ag charge collected after the GE/ASV detection method is performed on the model composites. Briefly, the MµB-sAgNP and MµB-AgNC model composites were prepared as described in the Experimental Section using different concentrations of just the sAgNP-Ab or just the AgNC-Ab conjugates. These formed composites were then transferred to the paper-electrode platform for electrochemical analysis. The goal for this first experiment was to determine a concentration of both composites that would

lead to the same amount of charge collected by GE/ASV. The results would then provide a context for comparing the labels in subsequent experiments.

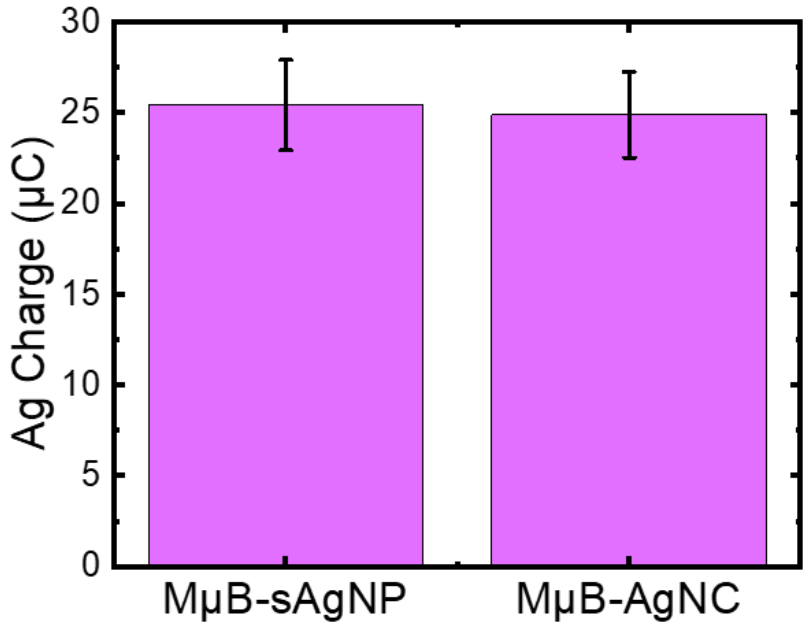

Figure 6.1 Histograms representing the amount of Ag charge obtained by forming the model composite assay with either sAgNP-Ab or AgNC-Ab conjugates (100 pM and 60.8 pM, respectively). These model composites were prepared using the MµB-SAb conjugate and either only the sAgNP-Ab conjugate, to make the "MµB-sAgNP" model composite, or only the AgNC-Ab conjugate, to make the "MµB-AgNC" model composite. Following assay formation, the samples were both washed and aliquoted, as described in the Experimental Section, and transferred to the paper electrode for analysis in 50.0 µL of PBS. The error bars represent the standard deviation from the mean for five independent measurements.

Figure 6.1 is a histogram comparing the Ag charge obtained using 100 pM of just the MµB-sAgNP model composite or 60.8 pM of just the MµB-AgNC model composite. The results indicate that at these concentrations there is no statistical difference in the charge collected using the two different model composites. Specifically, both model composites, which were prepared with Ag particles having different sizes, shapes, and surface ligands, resulted in a Ag charge of ~25.0 µC.

6.4.2 Optimization of the NP ratio

After establishing an appropriate context for comparing the sAgNP-Ab and AgNC-Ab conjugates (Figure 6.1), the model composite was systematically prepared using a mixture of the sAgNP-Ab and AgNC-Ab conjugates. The different volumetric ratios of the two conjugates were prepared using a 100 pM solution of the MµB-sAgNP model composite and a 60.8 pM solution of the MµB-AgNC model composite. These solutions were prepared as described in the Experimental Section and in accordance with Table S1. The key point is that the concentrations of the two composites (100 pm or 60.8 pm) used individually yield the same detection signal (Figure 6.1). Henceforth, we refer to this as "Ag charge

equivalence". Therefore, when the two labels are mixed in different ratios, it is possible to determine if a particular ratio leads to an optimal dynamic range and LOD that is superior to either of the two labels used individually.

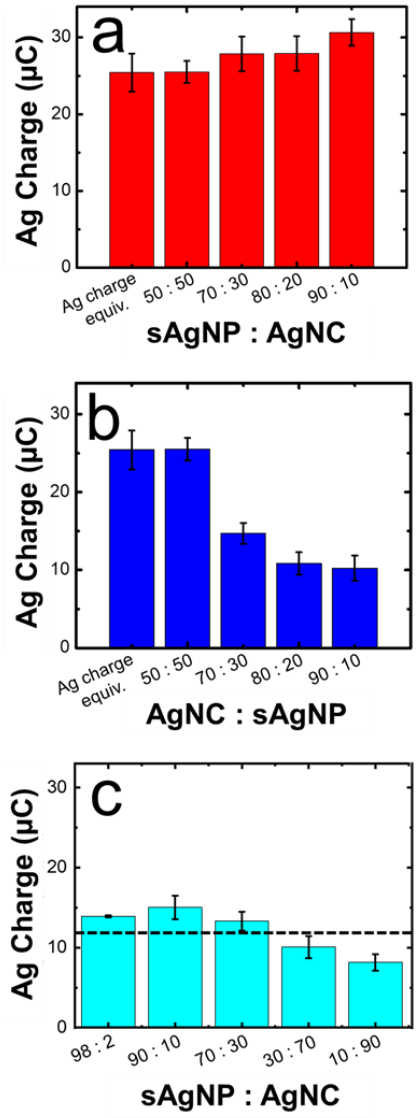

Figure 6.2 Histograms representing the amount of Ag charge collected from the model composite when it was prepared using different volumetric ratios of 100 pM sAgNP-Ab and 60.8 pM AgNC-Ab conjugates (Table 6.1).(a) NP ratios containing more sAgNPs than AgNCs (sAgNP:AgNC)and (b) NP ratios containing more AgNCs than sAgNPs (AgNC:sAgNP).(c) Same experiment as in (a), but the concentration of the model composite was diluted by 50%. The dashed line represents the expected Ag charge based on the result for the Ag charge equivalence in (a). The error bars represent the standard deviation from the mean for five independent measurements.

The histograms in Figure 6.2a correspond to the Ag charge collected when the model composite was formed with volume ratios that included more sAgNPs than AgNCs in the mixture. For example, for the 70:30 model composite, 70.0 µL of the sAgNP-Ab conjugate and 30.0 µL of the AgNC-Ab conjugates were added to 16.0 µL of MµB-SAb (Table 6.1). This result, and the other ratios, are compared to the "Ag charge equivalence" (first histogram in Figure 6.2a). Recall, that the Ag charge equivalence is the Ag charge resulting from the model composite yielding the same Ag charge but comprising only sAgNPs or only AgNCs (Figure 6.1). The results in Figure 6.2a show that the 90:10 NP ratio generated a Ag charge which was ~20% higher than when the model composite is formed with only the sAgNPs or only the AgNCs.

The histograms in Figure 6.2b were obtained exactly as discussed for Figure 6.2a, except for NP ratios that included more AgNCs than sAgNPs. The results indicate that when there are more AgNCs than sAgNPs present in the labeling mixture, the Ag charge collected after the GE/ASV detection method is significantly lower than the Ag charge equivalence results. The results in Figure 6.2b indicate

that NP ratios that include more AgNCs than sAgNPs are not optimal for sensing applications.

Up to this point, a relatively high concentration of the sAgNPs-Ab and AgNC-Ab conjugates (various percentages having concentrations of 100 pM and 60.8 pM, respectively) was used to form the model composite. The next step in the optimization process was to reduce the NP concentration by 50% (Figure 6.2c) to ensure that the same trends are observed over a range of concentrations (as would be encountered in a bioassay). An additional 98:2 ratio was also included in this part of the study. The dotted line in Figure 6.2c represents the expected Ag charge if the initial Ag concentration was diluted by 50%. For example, the benchmark value used in this experiment was the Ag charge equivalence, which resulted in ~25.0 µC of charge (Figure 6.1), therefore the expected Ag charge when the concentration is reduced by 50% is ~12.5 µC. The data in Figure 6.2c show that even when the concentration is reduced, the 90:10 sAgNP:AgNC ratio still results in a 20% increase in the expected Ag charge. On the basis of these results, the 90:10, sAgNP:AgNC ratio was used for the remaining experiments.

6.4.3 Calibration curve for the 90:10 sAgNP:AgNC model composite

After confirming that the 90:10, sAgNP:AgNC ratio is optimal for one concentration of Ag, this same ratio was applied to a series of different Ag concentrations. Accordingly, the model composite was prepared as described in the Experimental Section using a 90:10 volumetric ratio of the sAgNP-Ab and AgNC-Ab conjugates at total Ag NP concentrations ranging from 2.07 to 100 pM. The formed model composites were then washed using magnetic separation and transferred to the paper-electrode for electrochemical analysis.

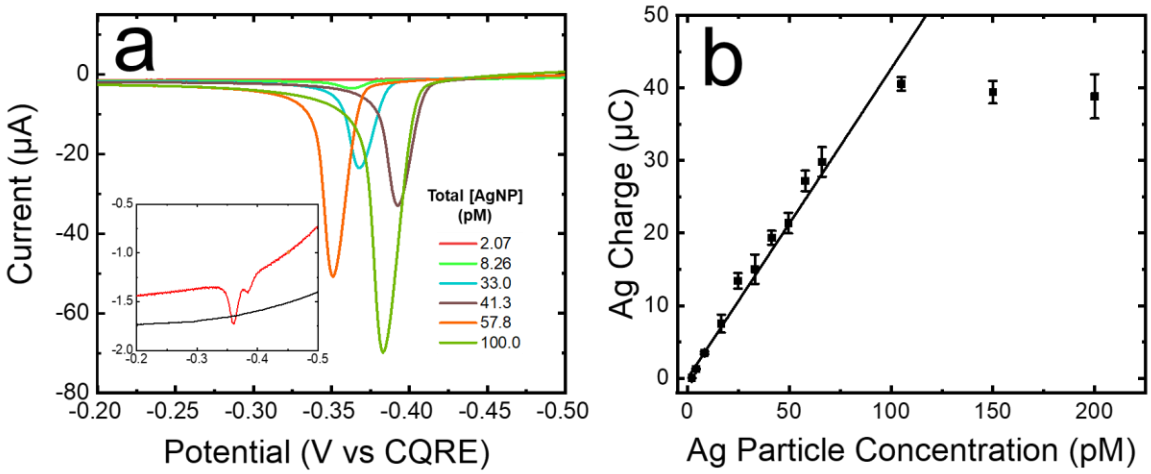

Figure 6.3 Electrochemical results for detection of the model composite formed using the 90:10 sAgNP:AgNC volumetric ratio and the GE/ASV detection protocol. (a) Representative ASVs for the total concentration of AgNPs (sAgNPs + AgNCs) indicated in the legend. For clarity, representative ASVs for only half of the concentrations used to construct the calibration curve in (b) are shown. The other half are provided in Figure 6.4. The position of the ASV peaks varies somewhat because the references electrode is a CQRE. (b) Calibration curve showing the correlation between the Ag charge (obtained by integrating ASVs like those in (a)) and the total AgNP concentrations (sAgNPs + AgNCs). This plot contains data shown in (a) and in Figure 6.4. The LOD, 2.07 pM, was calculated using the standard deviation of the linear regression line and the slope of the calibration curve. The linear regression value is 0.99 and the scan rate was 50 mV/s. Each data point represents the average of five measurements carried out using independently fabricated electrodes. The error bars represent the standard deviation of these five measurements. Outliers were eliminated using the Grubb's test with a 95% confidence level.

Figure 6.3 shows the results of this experiment. Specifically, the representative voltammograms in Figure 6.3a indicate that the Ag oxidation current increases as a function of the total concentration of AgNPs used to form the model composite assay. The inset includes an expanded view of the voltammogram for the blank (black trace). This solution contained AgNPs that were not bioconjugated to Abs, and it demonstrates that the assay has an intrinsic zero background. The inset also shows data for the lowest detectable AgNP concentration (2.07 pM, red trace).

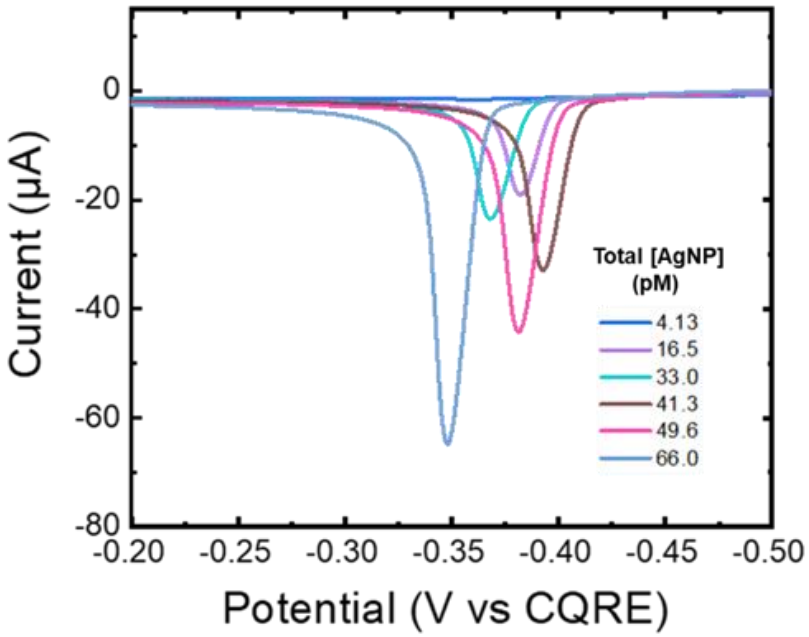

Figure 6.4 Representative ASVs for the total concentration of AgNPs (sAgNPs + AgNCs) indicated in the legend. ASVs for these concentrations were omitted from Figure 6.3a of this chapter for clarity. These data are for the 90:10 sAgNP:AgNC ratio. The position of the ASV peaks varies somewhat because the references electrode is a CQRE. The scan rate was 50 mV/s.

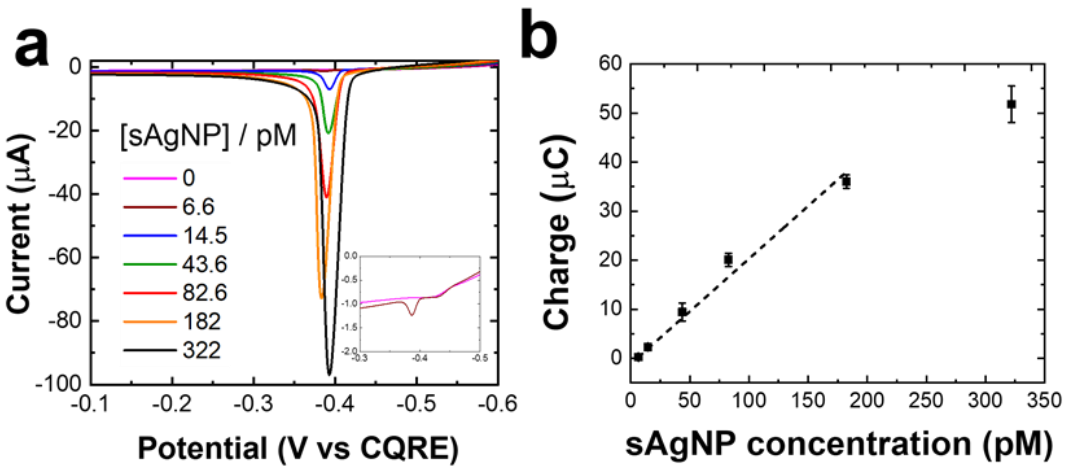

Figure 6.5 Calibration curve for the model composite formed using only the sAgNP-Ab conjugate. Specifically, this model composite was prepared by adding 100.0 µL of different Ag concentrations of the sAgNP-Ab conjugate to 16.0 µL of the MµB-SAb conjugate. The prepared model composite was washed using magnetic separation, and 50 µL were transferred to the paper-electrode for electrochemical analysis. (a) ASVs for the concentrations of sAgNPs indicated in the legend. For clarity, only one ASV trace is shown for each concentration. The position of the ASV peaks varies slightly because of the use of a CQRE. (b) Calibration curve showing the correlation between the Ag charge (obtained by integrating ASVs like those in (a)) and the sAgNP concentration. The linear regression value is 0.98 and the scan rate was 50 mV/s. Each data point represents the average of five measurements carried out using independently fabricated electrodes. The error bars represent the standard deviation of these five measurements. Outliers were eliminated using the Grubb's test with a 95% confidence level. These results show a linear dynamic range of 6.6-322 pM. This assay has an LOD that is three-fold higher than when the model composite assay is prepared using an optimized mixture of sAgNP-Ab and AgNC-Ab conjugates.

The charges under voltammograms like those shown in Figure 6.3a, plus voltammograms obtained at other concentrations (Figure 6.4) were obtained by integration, and the results for five independent experiments per concentration are plotted in Figure 6.3b. These data demonstrate that the charge increases linearly from 2.07 to 100.0 pM of total AgNPs (sAgNPs + AgNCs) and then begins to saturate. Note that concentrations below 2.07 pM could not be differentiated from the blank and thus are not shown in Figure 6.3. Nevertheless, the LOD of 2.07 pM represents a threefold decrease compared to the same assay carried out using only sAgNPs (Figure 6.5). Another important aspect of Figure 6.3b is that the relative standard deviation of the combined dataset is <11%.

6.4.4 Dose-response curve for the NT-proBNP metalloimmunoassay

The ultimate goal in this dual-shaped AgNP investigation is to ensure that the results leading up to this point can be translated to the NT-proBNP metalloimmunoassay, which is the main focus of our sensor-related research. Accordingly, the NT-proBNP bioassay was prepared in SBB using the step-wise procedure described in the Experimental Section. Specifically, 16.0 µL of the MµB-15C4 conjugate were added

to a SBB blocked microcentrifuge tubes, and then 100 µL of different concentrations of NT-proBNP were added. Following incubation and washing, an excess of the 90:10, sAgNP:AgNC conjugate ratio was added to the tubes. The fully formed assay was then transferred to the paper-electrode, and the electrochemical detection protocol was carried out in PBS.

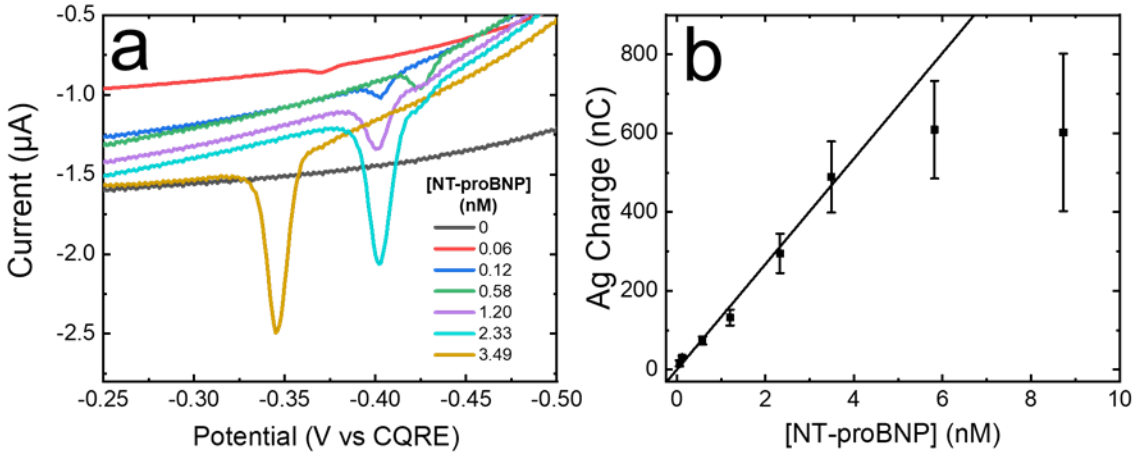

Figure 6.6 Electrochemical results obtained for detection of NT-proBNP using the 90:10 sAgNP:AgNC volumetric ratio and the GE/ASV detection protocol. (a) Anodic stripping voltammograms (ASVs) were obtained by aliquoting 2.0 µL of the formed assay, diluting it with 48.0 µL of PBS, and then carrying out the GE/ASV protocol described in the text. The concentrations listed in the legend represent the concentrations of NT-proBNP used to form the metalloimmunoassay. The scan rate was 50 mV/s. (b) Calibration curve showing the correlation between the Ag charge (obtained by integrating ASVs like those in (a)) and the concentration of NT-proBNP used to form the immuno-sandwich. Additionally, for clarity, the ASV for 5.82 nM of NT-proBNP is not shown in Figure 6.6a. The error bars represent the standard deviation obtained using five independent measurements. Outliers were eliminated using the Grubb's test with a 95% confidence level.

Representative ASV curves for this experiment are shown in Figure 6.6. The voltammograms in Figure 6.6a indicate that the Ag stripping current increases as a function of the concentration of the NT-proBNP used to form the assay. Note, however, that concentrations below 0.06 nM could not be differentiated from the background. The charges under voltammograms like those shown in Figure 6.6a were obtained by integration, and the results for five independent experiments per concentration are plotted in Figure 6.6b. These data show that the linear dynamic range for this assay is 0.06-3.49 nM of NT-proBNP, and then the calibration curve begins to saturate at 5.82 nM. The average relative standard deviation for the points on the linear part of the calibration curve is <21%.

Earlier we stated that the lowest LOD we have been able to achieve for the NT-proBNP metalloimmunoassay formed using only the sAgNP-Ab conjugate was about five-fold higher than the clinically relevant minimum value. Specifically, the lowest LOD heretofore achieved was 0.58 nM,[191] but the minimum clinical concentration used by physicians to identify heart failure patients who are at

risk of poor outcomes is 0.116 nM.[159–162] Using the dual-shaped AgNP conjugates, the risk stratification threshold for this bioassay is 0.06 nM, well below the target of 0.116 nM. We attribute this lower LOD to the incorporation of the AgNC-Ab conjugates to the Ag detection labels used in this bioassay. Recall that according to previously published literature, the AgNCs perform more efficiently during the GE process than the sAgNPs because the Au shell formed around the AgNCs is more porous, and therefore more exchange can occur.[79,82,84,90,221,223]

6.5 Summary and Conclusion

The overall goal of the present chapter was to develop an assay for the heart failure biomarker NT-proBNP that could perform within the clinically relevant concentration range. This range includes the risk stratification threshold used by physicians to determine next steps in the care of a patient. We have previously reported on this specific assay in which only sAgNPs were used as detection labels.[191] The use of only the sAgNP labels resulted in an LOD which was still five-fold higher than the clinically relevant minimum concentration of NT-proBNP. In an effort to reduce the LOD

of the assay, AgNCs were introduced as an additional detection label. This decision was made because prior literature indicated that AgNCs experience more efficient GE with Au^{3+} than sAgNPs.[79,82,84,90,221,223] Specifically, instead of a Au shell forming around the exterior of the NPs, as occurs for sAgNPs,[219,220] a porous Au layer forms. The porous Au layer results in more exchange during the GE process.[79,82,84,90,221,223]

The optimal volumetric ratio of the two labels was found to be 90:10 sAgNP:AgNCs. Using both types of lables simultaneously, we achieved a threefold decrease in the LOD for the model metalloimmunoassay. We attribute this result to the presence of the of the AgNCs, which undergo more efficient GE than the sAgNPs. The findings for the model assay translated well to the antigen-specific assay for NT-proBNP. In particular, the LOD for the metalloimmunoassay for NT-proBNP decreased by an order of magnitude, but the high end of the dynamic range was not affected by the presence of the AgNCs.[191] Accordingly, the NT-proBNP assay overlaps with the clinically relevant concentration range and risk stratification threshold for NT-proBNP in buffer.[159–162] The next steps for this NT-proBNP assay include

transitioning it into a serum matrix with the dual-shaped AgNP detection labels. The results of this work will be reported in due course.

Chapter 7: Summary and Conclusion

In this dissertation, the evolution of an electrochemical POC device for the detection of the heart failure biomarker, NT-proBNP was presented and discussed. Much like any biosensor, sensitivity and signal amplification were a few of the most important aspects that went into the design of this bioassay. Several other components came into play during the development process as well. Specifically, the sample matrix, the size of the biomarker of interest, the critical concentration range needed to determine the next steps in patient care, the frequency of use, and who the target consumer was.

All in all, the initial designs and fundamental research that starts at a laboratory bench must encompass all the above criteria, almost simultaneously. The fundamental mechanism of the detection method needs to be understood to the best of our ability, such as the investigation of the GE/ASV detection method described in Chapter 2. To facilitate a high-level of sensitivity and selectivity of the system, bioconjugation methods need to be optimal, such as the method described in Chapter 3. This optimization can also ensure that reagents are not being

wasted or used in extreme excess. This is largely because reagent waste can potentially increase the overall cost of the POC device, which would essentially negate one of the primary characteristics of the POC: low-cost.

Making the leap from one matrix to another is a critical component during development. In this case, transitioning the fully formed metalloimmunoassay from a simple buffer system to a more complex serum system, much like the processes discussed in Chapters 4 and 5. Additionally, piggybacking on that work to push the LOD of the sensor as close as possible to the risk stratification threshold, by simply changing the shape of the detection label to enhance signal amplification, such as the work described in Chapter 6.

We have made several significant and recent advancements with this biosensor, however there is much more work to be done. In general, transitioning all the off-chip manipulation steps to on-chip processes which could occur within a lateral flow or microfluidic setup. I am hopeful that this POC biosensor can eventually bring better patient care and peace of mind to individuals

currently struggling to maintain control of their own disease state and health.

Appendices

A1. Electrode fabrication

A slight modification of a previously published procedure was used to fabricate the electrodes.[127] Specifically, they were fabricated by stencil-printing carbon paste onto wax-patterned sheets of chromatography paper that had been printed using a Xerox ColorQube 8570DN printer. Following printing, the wax was melted through the thickness of the paper by placing it in an oven at 120 °C for 25.0 s. Photopaper was glued to the back of the wax-printed chromatography paper to improve rigidity, and then it was cut into 12 rectangles (2.0 cm × 5.0 cm, each). A stencil for defining the 3.0 mm-diameter disk-shaped working electrode, hook-shaped carbon quasi-reference electrode, and counter electrode was created using CorelDRAW (Ottawa, ON). The stencil was cut into a thin plastic sheet of transparency film using an Epilog laser engraving system (Zing 16). Finally, the stencil was placed over the paper (wax side up), the electrodes were printed through the stencil using the conductive carbon paste, and then they were left to dry in air for 14 h.

The working electrode was further modified by electrodepositing Au onto the carbon paste. This step was performed on-chip and was carried out by placing a 50.0 µL droplet of a solution consisting of 6.0 mM Au^{3+} and 0.10 M KNO_3 onto the electrode region of the sensor. Because the region of the sensor incorporating the electrodes is hydrophilic relative to the rest of the paper assembly, the deposition solution was confined to just the electrode region, and hence, no additional electrochemical cell was required. Next, the potential of the working electrode was stepped from 0 to −0.60 V (unless otherwise stated, all potentials are vs a carbon quasi-reference electrode, CQRE) for 2.0 s.[127] This process results in islands of Au (not a conformal coating) on the surface of the carbon.[127] The electrode was then rinsed twice with DI water and dried with a Kimwipe.

A2. The physisorption of Abs to NPs

Using a microcentrifuge tube blocked with Superblock blocking buffer (SBB), 500 µL of nanoparticle (NP) stock solution (4.9 x 10^{11} AgNPs/mL or 7.4 x 10^{11} AuNPs/mL) were added to 5 µL of 6.7 µM Ab. The mixture was incubated for

30 min at RT and 1400 rpm. Unbound Abs were removed with one centrifugation step (25 min, 4 ˚C, 16,600 g,), after which the supernatant was removed to leave behind only 5.0 µL of the initial solution (so as not to disturb the pellet). The NP pellet was then resuspended into a total volume of 500 µL of SBB. This solution was stored in the dark at 4 ˚C.

A3. Preparation of the AgNP-HBCL-Ab conjugate

Unless stated otherwise, all incubation steps were performed at RT at 600 rpm. To start, 5.0 µL of 6.7 µM Abs were incubated with 5.0 µL of 50.0 mM sodium meta-periodate ($NaIO_4$) for 30 min in the dark to oxidize the polysaccharide chains on the fragment crystallizable (FC) region of the Ab. The oxidation reaction was quenched with 125 µL of PBS. The oxidized Abs were then incubated with 5.0 µL of 5.0 mM of the heterobifunctional cross-linker (HBCL) solution for 2 h. The HBCL was first dissolved in dimethyl sulfoxide (DMSO) and then diluted in deionized (DI) water prior to being used. The modified Ab solution was transferred to an Amicon ultra 0.5 mL centrifugal filter (10 K) and was centrifuged for 25 min at 4 ˚C at 14,000 g. The HBCL-

modified Abs were then incubated with 500 µL of the AgNP solution (4.9 x 10^{11} AgNPs/mL) for 1 h. In this step, the microcentrifuge tubes were pre-blocked with superblock blocking buffer (SBB) to prevent non-specific binding of Abs and AgNPs on the walls of the tubes. These tubes were covered with aluminum foil to protect the AgNPs from light. Following incubation, 50.0 µL of 10.0 µM mPEG-SH were added and incubated for another 20 min. Finally, three centrifugation (25 min, 4 °C, 16,600 g) steps were performed to remove unbound material, followed by resuspension into 500 µL SBB.[180,106]

A4. Preparation of the MµB-Ab conjugate

First, 50.0 µL of 1.0 µm-diameter streptavidin-coated magnetic beads (MµB) were placed into a 0.6 mL PCR tube and washed by magnetic separation. The washing was carried out as follows: the tube was held up to the magnet so that the MµBs collected on the side of the tube (~30.0 s), and then the supernatant was removed. The MµBs were resuspended in 100 µL of PBS, vortexed, and gently centrifuged to pull the solution back into the bottom of the tube. The tube was then held up to the magnet again, and the supernatant was

removed. This was repeated four times. The MμBs were resuspended in 20.0 μL of PBS, and then 30.0 μL of 4.7 μM of the biotinylated 15C4 Ab were added. The tube was incubated at RT for 30 min on the tube revolver at 40 rpm. Finally, the MμBs were gently centrifuged back into the bottom of the tube and washed as previously described using SBB.[184] The final MμB-Ab conjugate was then resuspended in a final volume of 50.0 μL of SBB.

Protocol A5. Synthesis of AgNCs

The AgNCs were synthesized using a slightly modified version of a previously reported method.[224,221] Briefly, 5.0 mL of 100% EG in a 50 mL round-bottom flask were heated to 150 °C using an oil bath, and then 60.0 μL NaSH (3.0 mM in EG) were added. After 2 min, 0.50 mL HCl (3.0 mM in EG) and 1.25 mL polyvinylpyrrolidone (20.0 mg/mL in EG) were added. After another 2 min, 0.40 mL CF_3COOAg (282 mM in EG) was added. The reaction was stopped after 30 min by cooling the flask in an ice bath. The products were washed with acetone and DI water using centrifugation at 12,000 g, dispersed in water, and finally stored at 4 °C.

References

(1) Thvenot, D. R.; Toth, K.; Durst, R. A.; Wilson, G. S. Electrochemical Biosensors: Recommended Definitions and Classification (Technical Report). *Pure Appl. Chem.* **1999**, *71*, 2333–2348.

(2) Chin, C. D.; Linder, V.; Sia, S. K. Commercialization of Microfluidic Point-of-Care Diagnostic Devices. *Lab Chip* **2012**, *12*, 2118–2134.

(3) Yager, P.; Edwards, T.; Fu, E.; Helton, K.; Nelson, K.; Tam, M. R.; Weigl, B. H. Microfluidic Diagnostic Technologies for Global Public Health. *Nature* **2006**, *442*, 412–418.

(4) Gubala, V.; Harris, L. F.; Ricco, A. J.; Tan, M. X.; Williams, D. E. Point of Care Diagnostics: Status and Future. *Anal. Chem.* **2012**, *84*, 487–515.

(5) Gervais, L.; De Rooij, N.; Delamarche, E. Microfluidic Chips for Point-of-Care Immunodiagnostics. *Adv. Mater.* **2011**, *23*, H151–H176.

(6) Cunningham, J. C.; DeGregory, P. R.; Crooks, R. M. New Functionalities for Paper-Based Sensors Lead to Simplified User Operation, Lower Limits of Detection, and New Applications. *Annu. Rev. Anal. Chem.* **2016**, *9*,

183–202.

(7) Yetisen, A. K.; Akram, M. S.; Lowe, C. R. Paper-Based Microfluidic Point-of-Care Diagnostic Devices. *Lab Chip* **2013**, *13*, 2210–2251.

(8) Tüdos, A. J.; Besselink, G. A. J.; Schasfoort, R. B. M. Trends in Miniaturized Total Analysis Systems for Point-of-Care Testing in Clinical Chemistry. *Lab Chip* **2001**, *1*, 83–95.

(9) Yager, P.; Domingo, G. J.; Gerdes, J. Point-of-Care Diagnostics for Global Health. *Annu. Rev. Biomed. Eng.* **2008**, *10*, 107–144.

(10) Walgama, C.; Nguyen, M. P.; Boatner, L. M.; Richards, I.; Crooks, R. M. Hybrid Paper and 3D-Printed Microfluidic Device for Electrochemical Detection of Ag Nanoparticle Labels. *Lab Chip* **2020**, *20*, 1648–1657.

(11) Karami, P.; Khoshsafar, H.; Johari-Ahar, M.; Arduini, F.; Afkhami, A.; Bagheri, H. Colorimetric Immunosensor for Determination of Prostate Specific Antigen Using Surface Plasmon Resonance Band of Colloidal Triangular Shape Gold Nanoparticles. *Spectrochim. Acta - Part A Mol. Biomol. Spectrosc.* **2019**, *222*, 117218.

(12) Song, K.; Nimse, S. B.; Sonawane, M. D. Ultra-Sensitive NT-ProBNP Quantification for Early Detection of Risk Factors Leading to Heart Failure. *Sensors* **2017**, *17*, 2116.

(13) Li, H.; Yin, X.; Sun, D.; Xia, K.; Kang, C.; Chu, S.; Zhang, P.; Wang, H.; Qiu, Y. Detection of NT-pro BNP Using Fluorescent Protein Modified by Streptavidin as a Label in Immunochromatographic Assay. *Sens. Bio-Sensing Res.* **2016**, *11*, 1–7.

(14) Shi, L.; Li, X.; Zhu, W.; Wang, Y.; Du, B.; Cao, W.; Wei, Q.; Pang, X. Sandwich-Type Electrochemiluminescence Sensor for Detection of NT-ProBNP by Using High Efficiency Quench Strategy of Fe 3 O 4 @PDA toward Ru(Bpy) 32+ Coordinated with Silver Oxalate. *ACS Sensors* **2017**, *2*, 1774–1778.

(15) Zhang, H.; Han, Z.; Wang, X.; Li, F.; Cui, H.; Yang, D.; Bian, Z. Sensitive Immunosensor for N-Terminal pro-Brain Natriuretic Peptide Based on N-(Aminobutyl)-N-(Ethylisoluminol)-Functionalized Gold Nanodots/Multiwalled Carbon Nanotube Electrochemiluminescence Nanointerface. *ACS Appl. Mater. Interfaces* **2015**, 7, 7599–7604.

(16) Liu, Y.; Wang, H.; Xiong, C.; Chai, Y.; Yuan, R. An Ultrasensitive Electrochemiluminescence Immunosensor for NT-ProBNP Based on Self-Catalyzed Luminescence Emitter Coupled with PdCu@carbon Nanohorn Hybrid. *Biosens. Bioelectron.* **2017**, *87*, 779–785.

(17) Prontera, C.; Emdin, M.; Zucchelli, G. C.; Ripoli, A.; Passino, C.; Clerico, A. Analytical Performance and Diagnostic Accuracy of a Fully-Automated Electrochemiluminescent Assay for the N-Terminal Fragment of the pro-Peptide of Brain Natriuretic Peptide in Patients with Cardiomyopathy: Comparison with Immunoradiometric Assay Methods . *Clin. Chem. Lab. Med.* **2004**, *42*, 37–44.

(18) You, M.; Lin, M.; Gong, Y.; Wang, S.; Li, A.; Ji, L.; Zhao, H.; Ling, K.; Wen, T.; Huang, Y.; *et al.* Household Fluorescent Lateral Flow Strip Platform for Sensitive and Quantitative Prognosis of Heart Failure Using Dual-Color Upconversion Nanoparticles. *ACS Nano* **2017**, *11*, 6261–6270.

(19) Heller, A.; Feldman, B. Electrochemical Glucose Sensors and Their Applications in Diabetes Management. *Chem. Rev.* **2008**, *108*, 2482–2505.

(20) Ng, V. L.; Kraemer, R.; Hogan, C.; Eckman, D.; Siobal, M. The Rise and Fall of I-STAT Point-of-Care Blood Gas Testing in an Acute Care Hospital. *Am. J. Clin. Pathol.* **2000**, *114*, 128–138.

(21) Malhotra, B. D.; Chaubey, A. Biosensors for Clinical Diagnostics Industry. *Sensors Actuat. B Chem.* **2003**, *91*, 117–127.

(22) Erickson, K. A.; Wilding, P. Evaluation of a Novel Point-of-Care System, the i-STAT Portable Clinical Analyzer. *Clin. Chem.* **1993**, *39*, 283–287.

(23) Sarangadharan, I.; Wang, S. L.; Sukesan, R.; Chen, P. C.; Dai, T. Y.; Pulikkathodi, A. K.; Hsu, C. P.; Chiang, H. H. K.; Liu, L. Y. M.; Wang, Y. L. Single Drop Whole Blood Diagnostics: Portable Biomedical Sensor for Cardiac Troponin I Detection. *Anal. Chem.* **2018**, *90*, 2867–2874.

(24) Sinawang, P. D.; Harpaz, D.; Fajs, L.; Seong Seet, R. C.; Yoong Tok, A. I.; Marks, R. S. Electrochemical Impedimetric Detection of Stroke Biomarker NT-ProBNP Using Disposable Screen-Printed Gold Electrodes. *EuroBiotech J.* **2017**, *1*, 165–176.

(25) Wu, J.; Dong, M.; Zhang, C.; Wang, Y.; Xie, M.;

Chen, Y. Magnetic Lateral Flow Strip for the Detection of Cocaine in Urine by Naked Eyes and Smart Phone Camera. *Sensors* **2017**, *17*, 1286.

(26) Oncescu, V.; O'Dell, D.; Erickson, D. Smartphone Based Health Accessory for Colorimetric Detection of Biomarkers in Sweat and Saliva. *Lab Chip* **2013**, *13*, 3232–3238.

(27) Rehman, S. A.; Khurshid, Z.; Niazi, F. H.; Naseem, M.; Waddani, H. Al; Sahibzada, H. A.; Khan, R. S. Role of Salivary Biomarkers in Detection of Cardiovascular Diseases (CVD). *Proteomes* **2017**, *5*, 4–9.

(28) Chekin, F.; Vasilescu, A.; Jijie, R.; Singh, S. K.; Kurungot, S.; Iancu, M.; Badea, G.; Boukherroub, R.; Szunerits, S. Sensitive Electrochemical Detection of Cardiac Troponin I in Serum and Saliva by Nitrogen-Doped Porous Reduced Graphene Oxide Electrode. *Sensors Actuat. B Chem.* **2018**, *262*, 180–187.

(29) Song, Y.; Min, J.; Yu, Y.; Wang, H.; Yang, Y.; Zhang, H.; Gao, W. Wireless Battery-Free Wearable Sweat Sensor Powered by Human Motion. *Sci. Adv.* **2020**, *6*, 1–11.

(30) Wang, Z.; Gui, M.; Asif, M.; Yu, Y.; Dong, S.;

Wang, H.; Wang, W.; Wang, F.; Xiao, F.; Liu, H. A Facile Modular Approach to the 2D Oriented Assembly MOF Electrode for Non-Enzymatic Sweat Biosensors. *Nanoscale* **2018**, *10*, 6629–6638.

(31) Deng, M.; Li, M.; Li, F.; Mao, X.; Li, Q.; Shen, J.; Fan, C.; Zuo, X. Programming Accessibility of DNA Monolayers for Degradation-Free Whole-Blood Biosensors. *ACS Mater. Lett.* **2019**, *1*, 671–676.

(32) Magner, E. Detection of Ferricyanide as a Probe for the Effect of Hematocrit in Whole Blood Biosensors. *Analyst* **2001**, *126*, 861–865.

(33) Murawala, P.; Phadnis, S. M.; Bhonde, R. R.; Prasad, B. L. V. In Situ Synthesis of Water Dispersible Bovine Serum Albumin Capped Gold and Silver Nanoparticles and Their Cytocompatibility Studies. *Colloids Surf. B* **2009**, *73*, 224–228.

(34) Binaymotlagh, R.; Hadadzadeh, H.; Farrokhpour, H.; Haghighi, F. H.; Abyar, F.; Mirahmadi-Zare, S. Z. In Situ Generation of the Gold Nanoparticles-Bovine Serum Albumin (AuNPs-BSA) Bioconjugated System Using Pulsed-Laser Ablation (PLA). *Mater. Chem. Phys.* **2016**, *177*, 360–370.

(35) Chen, P.; McCreery, R. L. Control of Electron Transfer Kinetics at Glassy Carbon Electrodes by Specific Surface Modification. *Anal. Chem.* **1996**, *68*, 3958–3965.

(36) Doneux, T.; De Ghellinck, A.; Triffaux, E.; Brouette, N.; Sferrazza, M.; Buess-Herman, C. Electron Transfer Across an Antifouling Mercapto-Hepta(Ethylene Glycol) Self-Assembled Monolayer. *J. Phys. Chem. C* **2016**, *120*, 15915–15922.

(37) Wide, L.; Gemzell, C. A. An Immunological Pregnancy Test. *Acta Endrocrinol.* **1960**, *35*, 261–267.

(38) Yoo, E. H.; Lee, S. Y. Glucose Biosensors: An Overview of Use in Clinical Practice. *Sensors* **2010**, *10*, 4558–4576.

(39) Csöregi, E.; Schmidtke, D. W.; Heller, A. Design and Optimization of a Selective Subcutaneously Implantable Glucose Electrode Based on "Wired" Glucose Oxidase. *Anal. Chem.* **1995**, *67*, 1240–1244.

(40) Martinez, A. W.; Phillips, S. T.; Whitesides, G. M.; Carrilho, E. Diagnostics for the Developing World: Microfluidic Paper-Based Analytical Devices. *Anal. Chem.* **2010**, *82*, 3–10.

(41) Labib, M.; Sargent, E. H.; Kelley, S. O. Electrochemical Methods for the Analysis of Clinically Relevant Biomolecules. *Chem. Rev.* **2016**, *116*, 9001–9090.

(42) Conroy, P. J.; Hearty, S.; Leonard, P.; O'Kennedy, R. J. Antibody Production, Design and Use for Biosensor-Based Applications. *Semin. Cell Dev. Biol.* **2009**, *20*, 10–26.

(43) Fan, C.; Plaxco, K. W.; Heeger, A. J. Electrochemical Interrogation of Conformational Changes as a Reagentless Method for the Sequence-Specific Detection of DNA. *Proc. Natl. Acad. Sci. U. S. A.* **2003**, *100*, 9134–9137.

(44) Lubin, A. A.; Lai, R. Y.; Baker, B. R.; Heeger, A. J.; Plaxco, K. W. Sequence-Specific, Electronic Detection of Oligonucleotides in Blood, Soil, and Foodstuffs with the Reagentless, Reusable E-DNA Sensor. *Anal. Chem.* **2006**, *78*, 5671–5677.

(45) Yang, W.; Lai, R. Y. Comparison of the Stem-Loop and Linear Probe-Based Electrochemical DNA Sensors by Alternating Current Voltammetry and Cyclic Voltammetry. *Langmuir* **2011**, *27*, 14669–14677.

(46) Wu, Y.; Lai, R. Y. Development of a "Signal-on"

Electrochemical DNA Sensor with an Oligo-Thymine Spacer for Point Mutation Detection. *Chem. Commun.* **2013**, *49*, 3422–3424.

(47) Yang, W.; Gerasimov, J. Y.; Lai, R. Y. Folding-Based Electrochemical DNA Sensor Fabricated on a Gold-Plated Screen-Printed Carbon Electrode. *Chem. Commun.* **2009**, 2902–2904.

(48) Tuerk, C.; Gold, L. Systematic Evolution of Ligands by Exponential Enrichment: RNA Ligands to Bacteriophage T4 DNA Polymerase. *Science (80-.).* **1990**, *249*, 505–510.

(49) Ellington, A. D.; Szostak, J. W. In Vitro Selection of RNA Molecules That Bind Specific Ligands. *Nature* **1990**, *346*, 818–822.

(50) Zhao, S.; Yang, W.; Lai, R. Y. A Folding-Based Electrochemical Aptasensor for Detection of Vascular Endothelial Growth Factor in Human Whole Blood. *Biosens. Bioelectron.* **2011**, *26*, 2442–2447.

(51) Baker, B. R.; Lai, R. Y.; Wood, M. S.; Doctor, E. H.; Heeger, A. J.; Plaxco, K. W. An Electronic, Aptamer-Based Small-Molecule Sensor for the Rapid, Label-Free Detection of Cocaine in Adulterated Samples

and Biological Fluids. *J. Am. Chem. Soc.* **2006**, *128*, 3138–3139.

(52) Lai, R. Y.; Plaxco, K. W.; Heeger, A. J. Aptamer-Based Electrochemical Detection of Picomolar Platelet-Derived Growth Factor Directly in Blood Serum. *Anal. Chem.* **2007**, *79*, 229–233.

(53) Utgaard, J.; Frengen, J.; Stigbrand, T.; Ullen, A.; Schmit, R.; Lindom, T. Analyte and Label Binding Assay Read by Flow Cytometry. *Clin. Chem.* **1996**, *42*, 1702–1708.

(54) Dequaire, M.; Degrand, C.; Limoges, B. An Electrochemical Metalloimmunoassay Based on a Colloidal Gold Label. *Anal. Chem.* **2000**, *72*, 5521–5528.

(55) Mohammed, M. I.; Desmulliez, M. P. Y. Lab-on-a-Chip Based Immunosensor Principles and Technologies for the Detection of Cardiac Biomarkers: A Review. *Lab Chip* **2011**, *11*, 569–595.

(56) Dequaire, M.; Degrand, C.; Limoges, B. An Electrochemical Metalloimmunoassay Based on a Colloidal Gold Label. *Anal. Chem.* **2000**, *72*, 5521–5528.

(57) DeGregory, P. R.; Tsai, Y. J.; Scida, K.; Richards, I.; Crooks, R. M. Quantitative

Electrochemical Metalloimmunoassay for TFF3 in Urine Using a Paper Analytical Device. *Analyst* **2016**, *141*, 1734–1744.

(58) Cunningham, J. C.; Scida, K.; Kogan, M. R.; Wang, B.; Ellington, A. D.; Crooks, R. M. Paper Diagnostic Device for Quantitative Electrochemical Detection of Ricin at Picomolar Levels. *Lab Chip* **2015**, *15*, 3707–3715.

(59) DeGregory, P. R.; Tapia, J.; Wong, T.; Villa, J.; Richards, I.; Crooks, R. M. Managing Heart Failure at Home with Point-of-Care Diagnostics. *IEEE J. Transl. Eng. Heal. Med.* **2017**, *5*, 1–6.

(60) Malekzad, H.; Sahandi Zangabad, P.; Mirshekari, H.; Karimi, M.; Hamblin, M. R. Noble Metal Nanoparticles in Biosensors: Recent Studies and Applications. *Nanotechnol. Rev.* **2017**, *6*, 301–329.

(61) Scida, K.; Cunningham, J. C.; Renault, C.; Richards, I.; Crooks, R. M. Simple, Sensitive, and Quantitative Electrochemical Detection Method for Paper Analytical Devices. *Anal. Chem.* **2014**, *86*, 6501–6507.

(62) Hermanson, G. T. *Bioconjugate Techniques*; Audet, J.; Preap, M., Eds.; 3rd ed.; New York, 2013.

(63) Eggins, B. R. *Chemical Sensors and Biosensors*; John Wiley & Sons, Inc.: New York, 2002.

(64) Ronkainen, N. J.; Halsall, H. B.; Heineman, W. R. Electrochemical Biosensors. *Chem. Soc. Rev.* **2010**, *39*, 1747–1763.

(65) Bard, A. J.; Faulkner, L. R. *Electrochemical Methods: Fundamentals and Applications*; Harris, D.; Swain, E.; Robey, C.; Aiello, E., Eds.; 2nd ed.; John Wiley & Sons, Inc.: Hoboken, 2001.

(66) Cunningham, J. C.; Kogan, M. R.; Tsai, Y. J.; Luo, L.; Richards, I.; Crooks, R. M. Paper-Based Sensor for Electrochemical Detection of Silver Nanoparticle Labels by Galvanic Exchange. *ACS Sensors* **2016**, *1*, 40–47.

(67) Nie, Z.; Deiss, F.; Liu, X.; Akbulut, O.; Whitesides, G. M. Integration of Paper-Based Microfluidic Devices with Commercial Electrochemical Readers. *Lab Chip* **2010**, *10*, 3163.

(68) Nie, Z.; Nijhuis, C. A.; Gong, J.; Chen, X.; Kumachev, A.; Martinez, A. W.; Narovlyansky, M.; Whitesides, G. M. Electrochemical Sensing in Paper-Based Microfluidic Devices. *Lab Chip* **2010**, *10*, 477–483.

(69) Jiang, X.; Fan, Z. H. Fabrication and Operation of Paper-Based Analytical Devices. *Annu. Rev. Anal. Chem.* **2016**, *9*, 203–222.

(70) Mentele, M. M.; Cunningham, J.; Koehler, K.; Volckens, J.; Henry, C. S. Microfluidic Paper-Based Analytical Device for Particulate Metals. *Anal. Chem.* **2012**, *84*, 4474–4480.

(71) Authier, L.; Grossiord, C.; Brossier, P.; Limoges, B. Gold Nanoparticle-Based Quantitative Electrochemical Detection of Amplified Human Cytomegalovirus DNA Using Disposable Microband Electrodes. *Anal. Chem.* **2001**, *73*, 4450–4456.

(72) Brankovic, S. R.; Wang, J. X.; Adžić, R. R. Metal Monolayer Deposition by Replacement of Metal Adlayers on Electrode Surfaces. *Surf. Sci.* **2001**, *474*, L173–L179.

(73) Xia, X.; Wang, Y.; Ruditskiy, A.; Xia, Y. 25th Anniversary Article: Galvanic Replacement: A Simple and Versatile Route to Hollow Nanostructures with Tunable and Well-Controlled Properties. *Adv. Mater.* **2013**, *25*, 6313–6332.

(74) Anderson, B. D.; Tracy, J. B. Nanoparticle Conversion Chemistry: Kirkendall Effect, Galvanic

Exchange, and Anion Exchange. *Nanoscale* **2014**, *6*, 12195–12216.

(75) Guo, D. J.; Ding, Y. Porous Nanostructured Metals for Electrocatalysis. *Electroanalysis* **2012**, *24*, 2035–2043.

(76) Papaderakis, A.; Mintsouli, I.; Georgieva, J.; Sotiropoulos, S. Electrocatalysts Prepared by Galvanic Replacement. *Catalysts* **2017**, *7*, 80.

(77) Zhang, J.; Mo, Y.; Vukmirovic, M. B.; Klie, R.; Sasaki, K.; Adzic, R. R. Platinum Monolayer Electrocatalysts for O2 Reduction: Pt Monolayer on Pd(111) and on Carbon-Supported Pd Nanoparticles. *J. Phys. Chem. B* **2004**, *108*, 10955–10964.

(78) Sasaki, K.; Adzic, R. R. Monolayer-Level Ru- and NbO2-Supported Platinum Electrocatalysts for Methanol Oxidation. *J. Electrochem. Soc.* **2008**, *155*, B180–B186.

(79) Skrabalak, S. E.; Au, L.; Li, X.; Xia, Y. Facile Synthesis of Ag Nanocubes and Au Nanocages. *Nat. Protoc.* **2007**, *2*, 2182–2190.

(80) Skrabalak, S. E.; Chen, J.; Sun, Y.; Lu, X.; Au, L.; Cobley, C. M.; Xia, Y. Gold Nanocages: Synthesis, Properties, and Applications. *Acc. Chem. Res.* **2008**, *41*,

1587–1595.

(81) Sun, Y.; Mayers, B. T.; Xia, Y. Template-Engaged Replacement Reaction: A One Step Approach to the Large Scale Synthesis of Metal Nanostructures with Hollow Interiors. *Nano Lett* **2002**, *2*, 481–485.

(82) Au, L.; Lu, X.; Xia, Y. A Comparative Study of Galvanic Replacement Reactions Involving Ag Nanocubes and AuCl2– or AuCl4–**. *Adv. Mater.* **2008**, *20*, 2517–2522.

(83) Zhao, M.; Crooks, R. M. Intradendrimer Exchange of Metal Nanoparticles. *Chem. Mater.* **1999**, *11*, 3379–3385.

(84) Chen, J.; Mclellan, J. M.; Siekkinen, A.; Xiong, Y.; Li, Z. Facile Synthesis of Gold - Silver Nanocages with Controllable Pores on the Surface. *J. Am. Chem. Soc.* **2006**, *128*, 14776–14777.

(85) Zhang, Q.; Lee, J. Y.; Yang, J.; Boothroyd, C.; Zhang, J. Size and Composition Tunable Ag–Au Alloy Nanoparticles by Replacement Reactions. *Nanotechnology* **2007**, *18*, 245605.

(86) Zhang, Q.; Xie, J.; Lee, J. Y.; Zhang, J.; Boothroyd, C. Synthesis of Ag@AgAu Metal Core/Alloy

Shell Bimetallic Nanoparticles with Tunable Shell Compositions by a Galvanic Replacement Reaction. *Small* **2008**, *4*, 1067–1071.

(87) Park, T.-H.; Lee, H.; Lee, J.; Jang, D.-J. Morphology Evolution of Ag/Au Nanocomposites via Temperature-Controlled Galvanic Exchange to Enhance Catalytic Activity. *RSC Adv.* **2017**, *7*, 7718–7724.

(88) Sun, Y.; Wang, Y. Monitoring of Galvanic Replacement Reaction between Silver Nanowires and HAuCl4 by in Situ Transmission X-Ray Microscopy. *Nano Lett.* **2011**, *11*, 4386–4392.

(89) Lu, X.; Tuan, H. Y.; Chen, J.; Li, Z. Y.; Korgel, B. A.; Xia, Y. Mechanistic Studies on the Galvanic Replacement Reaction between Multiply Twinned Particles of Ag and HAuCl4 in an Organic Medium. *J. Am. Chem. Soc.* **2007**, *129*, 1733–1742.

(90) Lu, X.; Au, L.; McLellan, J.; Li, Z. Y.; Marquez, M.; Xia, Y. Fabrication of Cubic Nanocages and Nanoframes by Dealloying Au/Ag Alloy Nanoboxes with an Aqueous Etchant Based on Fe(NO 3) 3 or NH 4OH. *Nano Lett.* **2007**, *7*, 1764–1769.

(91) Smith, J. G.; Zhang, X.; Jain, P. K. Galvanic

Reactions at the Single-Nanoparticle Level: Tuning Between Mechanistic Extremes. *J. Mater. Chem. A* **2017**, *5*, 11940–11948.

(92) Cunningham, J. C.; Brenes, N. J.; Crooks, R. M. Paper Electrochemical Device for Detection of DNA and Thrombin by Target-Induced Conformational Switching. *Anal. Chem.* **2014**, *86*, 6166–6170.

(93) Hezard, T.; Fajerwerg, K.; Evrard, D.; Collire, V.; Behra, P.; Gros, P. Gold Nanoparticles Electrodeposited on Glassy Carbon Using Cyclic Voltammetry: Application to Hg(II) Trace Analysis. *J. Electroanal. Chem.* **2012**, *664*, 46–52.

(94) Zhang, Xu; Servos, Mark; Liu, J. Instantaneous and Quantative Functionalization of Gold Nanoparticles with Thiolated DNA Using a PH-Assited and Surfactant-Free Route. *J. Power Sources* **2012**, *134*, 7266–7269.

(95) Li, X.; Scida, K.; Crooks, R. M. Detection of Hepatitis B Virus DNA with a Paper Electrochemical Sensor. *Anal. Chem.* **2015**, *87*, 9009–9015.

(96) Weber, P. C.; Ohlendorf, D. H.; Wendoloski, J. J.; Salemme, F. R. Structural Origins of High-Affinity Biotin Binding to Streptavidin. *Science* **1989**, *243*, 85–

88.

(97) González, E.; Arbiol, J.; Puntes, V. F. Carving at the Nanoscale: Sequential Galvanic Exchange and Kirkendall Growth at Room Temperature. *Science* **2011**, *334*, 1377–1380.

(98) Au, L.; Zheng, D.; Zhou, F.; Li, Z. Y.; Li, X.; Xia, Y.; Study, Q.; Effect, P.; Gold, I.; Targeted, N.; *et al.* A Quantitative Study on the Photothermal Effect of Immuno Gold Nanocages Targeted to Breast Cancer. *ACS Nano* **2008**, *2*, 1645–1652.

(99) Chen, J.; Wiley, B.; Li, Z. Y.; Campbell, D.; Saeki, F.; Cang, H.; Au, L.; Lee, J.; Li, X.; Xia, Y. Gold Nanocages: Engineering Their Structure for Biomedical Applications. *Adv. Mater.* **2005**, *17*, 2255–2261.

(100) Yang, Y.; Liu, J.; Fu, Z.-W.; Qin, D. Galvanic Replacement-Free Deposition of Au on Ag for Core–Shell Nanocubes with Enhanced Chemical Stability and SERS Activity. *J. Am. Chem. Soc.* **2014**, *136*, 8153–8156.

(101) Rioux, D.; Meunier, M. Seeded Growth Synthesis of Composition and Size-Controlled Gold-Silver Alloy Nanoparticles. *J. Phys. Chem. C* **2015**, *119*, 13160–13168.

(102) Harris, D. C. *Quantitative Chemical Analysis*; 8th ed.; Freeman, W. H., 2011.

(103) Zhang, Y.; Sun, Y.; Liu, Z.; Xu, F.; Cui, K.; Shi, Y.; Wen, Z.; Li, Z. Au Nanocages for Highly Sensitive and Selective Detection of H2O2. *J. Electroanal. Chem.* **2011**, *656*, 23–28.

(104) Hermanson, G. T. *Bioconjugate Techniques*; Audet, J.; Preap, M., Eds.; Academic Press, 2013.

(105) Sivaram, A. J.; Wardiana, A.; Howard, C. B.; Mahler, S. M.; Thurecht, K. J. Recent Advances in the Generation of Antibody–Nanomaterial Conjugates. *Adv. Healthc. Mater.* **2018**, *7*, 1–25.

(106) Kumar, S.; Aaron, J.; Sokolov, K. Directional Conjugation of Antibodies to Nanoparticles for Synthesis of Multiplexed Optical Contrast Agents with Both Delivery and Targeting Moieties. *Nat. Protoc.* **2008**, *3*, 314–320.

(107) Joshi, P. P.; Yoon, S. J.; Hardin, W. G.; Emelianov, S.; Sokolov, K. V. Conjugation of Antibodies to Gold Nanorods through Fc Portion: Synthesis and Molecular Specific Imaging. *Bioconjugate Chem.* **2013**, *24*, 878–888.

(108) Love, J. C.; Estroff, L. A.; Kriebel, J. K.; Nuzzo, R. G.; Whitesides, G. M. Self-Assembled Monolayers of Thiolates on Metals as a Form of Nanotechnology. *Chem. Rev.* **2005**, *105*, 1103–1169.

(109) Porcaro, F.; Marini, C.; Venditti, I.; Fratoddi, I.; Carlini, L.; Simonelli, L.; Olszewski, W.; Meneghini, C.; Luisetto, I.; Battocchio, C.; *et al.* Synthesis and Structural Characterization of Silver Nanoparticles Stabilized with 3-Mercapto-1-Propansulfonate and 1-Thioglucose Mixed Thiols for Antibacterial Applications. *Materials (Basel).* **2016**, *9*, 1028.

(110) Battocchio, C.; Meneghini, C.; Fratoddi, I.; Venditti, I.; Russo, M. V.; Aquilanti, G.; Maurizio, C.; Bondino, F.; Matassa, R.; Rossi, M.; *et al.* Silver Nanoparticles Stabilized with Thiols: A Close Look at the Local Chemistry and Chemical Structure. *J. Phys. Chem.* **2012**, *116*, 19571–19578.

(111) Stewart, A.; Zheng, S.; McCourt, M. R.; Bell, S. E. J. Controlling Assembly of Mixed Thiol Monolayers on Silver Nanoparticles to Tune Their Surface Properties. *ACS Nano* **2012**, *6*, 3718–3726.

(112) Trilling, A. K.; Beekwilder, J.; Zuilhof, H. Antibody Orientation on Biosensor Surfaces: A Minireview. *Analyst* **2013**, *138*, 1619–1627.

(113) Basu Neogi, P.; Gryczynski, Z.; Choi, T. Y.; Neogi, A.; Calander, N.; Kim, M.; Lee, K. M.; Luchowski, R.; Kim, B. Silver Nanostructure Sensing Platform for Maximum-Contrast Fluorescence Cell Imaging. *J. Biomed. Opt.* **2011**, *16*, 056008.

(114) Goldman, Y. E.; Cooperman, B. S.; Mandecki, W.; Smilansky, Z.; Kaur, J.; Chen, C.; Stevens, B.; Bharill, S.; Gryczynski, Z.; Gryczynski, I. Enhancement of Single-Molecule Fluorescence Signals by Colloidal Silver Nanoparticles in Studies of Protein Translation. *ACS Nano* **2010**, *5*, 399–407.

(115) Tripathi, K.; Driskell, J. D. Quantifying Bound and Active Antibodies Conjugated to Gold Nanoparticles: A Comprehensive and Robust Approach to Evaluate Immobilization Chemistry. *ACS Omega* **2018**, *3*, 8253–8259.

(116) Wiseman, M. E.; Frank, C. W. Antibody Adsorption and Orientation on Hydrophobic Surfaces. *Langmuir* **2012**, *28*, 1765–1774.

(117) Ruiz, G.; Tripathi, K.; Okyem, S.; Driskell, J.

D. PH Impacts the Orientation of Antibody Adsorbed onto Gold Nanoparticles. *Bioconjugate Chem.* **2019**, *30*, 1182–1191.

(118) Hu, T.; Chen, C.; Huang, G.; Yang, X. Antibody Modified-Silver Nanoparticles for Colorimetric Immuno Sensing of Aβ(1-40/1-42) Based on the Interaction between β-Amyloid and Cu2+. *Sensors Actuators B Chem.* **2016**, *234*, 63–69.

(119) Rekha, C. R.; Nayar, V. U.; Gopchandran, K. G. Synthesis of Highly Stable Silver Nanorods and Their Application as SERS Substrates. *J. Sci. Adv. Mater. Devices* **2018**, *3*, 196–205.

(120) Oraevsky, A. A. "Contrast Agents for Optoacoustic Imaging: Design and Biomedical Applications." *Photoacoustics* **2015**, *3*, 1–2.

(121) Arruebo, M.; Valladares, M.; González-Fernández, Á. Antibody-Conjugated Nanoparticles for Biomedical Applications. *J. Nanomater.* **2009**, *2009*, 1–24.

(122) Sokolov, K.; Follen, M.; Aaron, J.; Pavlova, I.; Malpica, A.; Lotan, R.; Richards-Kortum, R. Real-Time Vital Optical Imaging of Precancer Using Anti-Epidermal Growth Factor Receptor Antibodies Conjugated to Gold

Nanoparticles. *Cancer Res.* **2003**, *63*, 1999–2004.

(123) Szymanski, M. S.; Porter, R. A. Preparation and Quality Control of Silver Nanoparticle-Antibody Conjugate for Use in Electrochemical Immunoassays. *J. Immunol. Methods* **2013**, *387*, 262–269.

(124) Buijs, J.; Lichtenbelt, J. W. T.; Norde, W.; Lyklema, J. Adsorption of Monoclonal IgGs and Their F(Ab')2 Fragments onto Polymeric Surfaces. *Colloids Surfaces B Biointerfaces* **1995**, *5*, 11–23.

(125) Weisbecker, S.; Merritt, V.; Weisbecker, C. S.; Merritt, M. V; Whitesidesx, G. M. Molecular of Aliphatic Thiols on Gold Golloids. *Langmuir* **1996**, *12*, 3763–3772.

(126) Canaria, C. A.; Maloney, J. R.; Yu, C. J.; Smith, J. O.; Fraser, S. E.; Lansford, R. Formation of Biotinylated Alkylthiolate Self-Assembled Monolayers on Gold. *Nanotechnology* **2005**, *2*, 321–324.

(127) Kogan, M. R.; Pollok, N. E.; Crooks, R. M. Detection of Silver Nanoparticles by Electrochemically Activated Galvanic Exchange. *Langmuir* **2018**, *34*, 15719–15726.

(128) Cheng, X.; Liu, M.; Zhang, A.; Hu, S.; Song, C.;

Zhang, G.; Guo, X. Size-Controlled Silver Nanoparticles Stabilized on Thiol-Functionalized MIL-53(Al) Frameworks. *Nanoscale* **2015**, 7, 9738–9745.

(129) Huang, T.; Nallathamby, P. D.; Gillet, D.; Xu, X. H. N. Design and Synthesis of Single-Nanoparticle Optical Biosensors for Imaging and Characterization of Single Receptor Molecules on Single Living Cells. *Anal. Chem.* **2007**, *79*, 7708–7718.

(130) Kaghu, R. V; Sarma, A.; Silverton, E. W.; Terryi, D. D. The Three-Dimensional Structure at 6 A Resolution Human Molecule. *Biol. Chem.* **1971**, *246*, 3753–3759.

(131) McCombs, J. R.; Owen, S. C. Antibody Drug Conjugates: Design and Selection of Linker, Payload and Conjugation Chemistry. *AAPS J.* **2015**, *17*, 339–351.

(132) Liddell, E. The Immunoassay Handbook: Theory and Applications of Ligand Binding, ELISA and Related Techniques. In; Wild, D. G.; John, R.; Sheehan, C.; Binder, S.; He, J., Eds.; Elsevier: Oxford, 2013.

(133) Chen, Y. T.; Medhi, R.; Nekrashevich, I.; Litvinov, D.; Xu, S.; Lee, T. R. Specific Detection of Proteins Using Exceptionally Responsive Magnetic Particles. *Anal. Chem.* **2018**, *90*, 6749–6756.

(134) Lin, P. C.; Chen, S. H.; Wang, K. Y.; Chen, M. L.; Adak, A. K.; Hwu, J. R. R.; Chen, Y. J.; Lin, C. C. Fabrication of Oriented Antibody-Conjugated Magnetic Nanoprobes and Their Immunoaffinity Application. *Anal. Chem.* **2009**, *81*, 8774–8782.

(135) Wu, X.; Li, Z.; Chen, X. X.; Fossey, J. S.; James, T. D.; Jiang, Y. B. Selective Sensing of Saccharides Using Simple Boronic Acids and Their Aggregates. *Chem. Soc. Rev.* **2013**, *42*, 8032–8048.

(136) Haiss, W.; Thanh, N. T. K.; Aveyard, J.; Fernig, D. G. Determination of Size and Concentration of Gold Nanoparticles from Extinction Spectra. *Anal. Chem.* **2008**, *80*, 6620–6625.

(137) Rahme, K.; Chen, L.; Hobbs, R. G.; Morris, M. A.; O'Driscoll, C.; Holmes, J. D. PEGylated Gold Nanoparticles: Polymer Quantification as a Function of PEG Lengths and Nanoparticle Dimensions. *RSC Adv.* **2013**, *3*, 6085–6094.

(138) Umadevi, M. Fluorescence Quenching by Plasmonic Silver Nanoparticles. In *Surface Plasmon Enhanced, Coupled and Controlled Fluorescence*; Geddes, C. D., Ed.; John Wiley & Sons, Inc., 2017; pp. 197–202.

(139) Kavitha, S. R.; Umadevi, M.; Vanelle, P.; Terme, T.; Khoumeri, O. Spectral Investigations on the Influence of Silver Nanoparticles on the Fluorescence Quenching of 1,4-Dimethoxy-2,3-Dibromomethylanthracene-9,10-Dione. *Eur. Phys. J. D* **2014**, *68*.

(140) Kavitha, S. R.; Umadevi, M.; Vanelle, P.; Terme, T.; Khoumeri, O. Spectral Investigations on the Fluorescence Quenching of 1,4-Dihydroxy-2,3-Dimethylanthracene-9,10-Dione by Plasmonic Silver Nanoparticles. *Plasmonics* **2014**, *9*, 443–450.

(141) Filbrun, S. L.; Driskell, J. D. A Fluorescence-Based Method to Directly Quantify Antibodies Immobilized on Gold Nanoparticles. *Analyst* **2016**, *141*, 3851–3857.

(142) Zhang, L.; Hu, D.; Salmain, M.; Liedberg, B.; Boujday, S. Direct Quantification of Surface Coverage of Antibody in IgG-Gold Nanoparticles Conjugates. *Talanta* **2019**, *204*, 875–881.

(143) Liu, S.; Horak, J.; Höldrich, M.; Lämmerhofer, M. Accurate and Reliable Quantification of the Protein Surface Coverage on Protein-Functionalized Nanoparticles. *Anal. Chim. Acta* **2017**, *989*, 29–37.

(144) Moulin, A. M.; Shea, S. J. O.; Welland, M. E. Microcantilever-Based Biosensors. *Ultramicroscopy* **1999**, *82*, 23–31.

(145) Saenger, A. K.; Rodriguez-Fraga, O.; Ler, R.; Ordonez-Llanos, J.; Jaffe, A. S.; Goetze, J. P.; Apple, F. S. Specificity of B-Type Natriuretic Peptide Assays: Cross-Reactivity with Different BNP, NT-ProBNP, and ProBNP Peptides. *Clin. Chem.* **2017**, *63*, 351–358.

(146) Seferian, K. R.; Tamm, N. N.; Semenov, A. G.; Mukharyamova, K. S.; Tolstaya, A. A.; Koshkina, E. V.; Kara, A. N.; Krasnoselsky, M. I.; Apple, F. S.; Esakova, T. V.; *et al.* The Brain Natriuretic Peptide (BNP) Precursor Is the Major Immunoreactive Form of BNP in Patients with Heart Failure. *Clin. Chem.* **2007**, *53*, 866–873.

(147) Seferian, K. R.; Tamm, N. N.; Semenov, A. G.; Tolstaya, A. A.; Koshkina, E. V.; Krasnoselsky, M. I.; Postnikov, A. B.; Serebryanaya, D. V.; Apple, F. S.; Murakami, M. M.; *et al.* Immunodetection of Glycosylated NT-ProBNP Circulating in Human Blood. *Clin. Chem.* **2008**, *54*, 866–873.

(148) Treuel, L.; Brandholt, S.; Maffre, P.; Wiegele,

S.; Shang, L.; Nienhaus, G. U. Impact of Protein Modification on the Protein Corona on Nanoparticles and Nanoparticle-Cell Interactions. *ACS Nano* **2014**, *8*, 503–513.

(149) Ruiz, G.; Ryan, N.; Rutschke, K.; Awotunde, O.; Driskell, J. D. Antibodies Irreversibly Adsorb to Gold Nanoparticles and Resist Displacement by Common Blood Proteins. *Langmuir* **2019**, *35*, 10601–10609.

(150) Sonawane, M. D.; Nimse, S. B.; Song, K. S.; Kim, T. Multiplex Detection of Cardiac Biomarkers. *Anal. Methods* **2017**, *9*, 3773–3776.

(151) Lutz, S.; Lopez-Calle, E.; Espindola, P.; Boehm, C.; Brueckner, T.; Spinke, J.; Marcinowski, M.; Keller, T.; Tgetgel, A.; Herbert, N.; *et al.* A Fully Integrated Microfluidic Platform for Highly Sensitive Analysis of Immunochemical Parameters. *Analyst* **2017**, *142*, 4206–4214.

(152) Li, Z.; Ausri, I. R.; Zilberman, Y.; Tang, X. (Shirley). Towards Label-Free, Wash-Free and Quantitative B-Type Natriuretic Peptide Detection for Heart Failure Diagnosis. *Nanoscale* **2019**, 18347–18357.

(153) Liang, W.; Li, Y.; Zhang, B.; Zhang, Z.; Chen,

A.; Qi, D.; Yi, W.; Hu, C. A Novel Microfluidic Immunoassay System Based on Electrochemical Immunosensors: An Application for the Detection of NT-ProBNP in Whole Blood. *Biosens. Bioelectron.* **2012**, *31*, 480–485.

(154) Roger, V. L. Epidemiology of Heart Failure. *Circ Res* **2013**, *113*, 646–659.

(155) Kuhn, M. A Big-Hearted Molecule. *Nature* **2015**, *519*, 416–417.

(156) Semenov, A. G.; Tamm, N. N.; Seferian, K. R.; Postnikov, A. B.; Karpova, N. S.; Serebryanaya, D. V.; Koshkina, E. V.; Krasnoselsky, M. I.; Katrukha, A. G. Processing of Pro-B-Type Natriuretic Peptide: Furin and Corin as Candidate Convertases. *Clin. Chem.* **2010**, *56*, 1166–1176.

(157) Levin, E. R.; Gardner, D. G.; Samson, W. K. Natriuretic Peptides. *N. Engl. J. Med.* **1998**, *339*, 321–328.

(158) Kim, H.-N.; Januzzi, J. L. Natriuretic Peptide Testing in Heart Failure. *Circulation* **2011**, *123*, 2015–2019.

(159) Zile, M. R.; Claggett, B. L.; Prescott, M. F.;

McMurray, J. J. V.; Packer, M.; Rouleau, J. L.; Swedberg, K.; Desai, A. S.; Gong, J.; Shi, V. C.; *et al.* Prognostic Implications of Changes in N-Terminal Pro-B-Type Natriuretic Peptide in Patients With Heart Failure. *J. Am. Coll. Cardiol.* **2016**, *68*, 2425–2436.

(160) Felker, G. M.; Ahmad, T.; Anstrom, K. J.; Adams, K. F.; Cooper, L. S.; Ezekowitz, J. A.; Fiuzat, M.; Houston-Miller, N.; Januzzi, J. L.; Leifer, E. S.; *et al.* Rationale and Design of the Guide-It Study: Guiding Evidence Based Therapy Usingbiomarker Intensified Treatment in Heart Failure. *JACC Hear. Fail.* **2014**, *2*, 458–465.

(161) Masson, S.; Latini, R.; Anand, I. S.; Vago, T.; Angelici, L.; Barlera, S.; Missov, E. D.; Clerico, A.; Tognoni, G.; Cohn, J. N. Direct Comparison of B-Type Natriuretic Peptide (BNP) and Amino-Terminal ProBNP in a Large Population of Patients with Chronic and Symptomatic Heart Failure: The Valsartan Heart Failure (Val-HeFT) Data. *Clin. Chem.* **2006**, *52*, 1528–1538.

(162) Januzzi, J. L.; Troughton, R. Serial Natriuretic Peptide Measurements Are Useful in Heart Failure Management. *Circulation* **2013**, *127*, 500–508.

(163) Yancy, C. W.; Jessup, M.; Bozkurt, B.; Butler, J.; Casey, D. E.; Drazner, M. H.; Fonarow, G. C.; Geraci, S. A.; Horwich, T.; Januzzi, J. L.; *et al.* 2013 ACCF/AHA Guideline for the Management of Heart Failure. *J. Am. Coll. Cardiol.* **2013**, *62*, e147–e239.

(164) Palazzuoli, A.; Gallotta, M.; Quatrini, I.; Nuti, R. Natriuretic Peptides (BNP and NT-ProBNP): Measurement and Relevance in Heart Failure. *Vasc. Health Risk Manag.* **2010**, *6*, 411–418.

(165) Richards, M.; Troughton, R. W. NT-ProBNP in Heart Failure: Therapy Decisions and Monitoring. *Eur. J. Heart Fail.* **2004**, *6*, 351–354.

(166) McCullough, P. A.; Kluger, A. Y. Interpreting the Wide Range of NT-ProBNP Concentrations in Clinical Decision Making. *J. Am. Coll. Cardiol.* **2018**, *71*, 1201–1203.

(167) Wu, A. H. B.; Smith, A.; Wieczorek, S.; Mather, J. F.; Duncan, B.; White, C. M.; McGill, C.; Katten, D.; Heller, G. Biological Variation for N-Terminal pro- and B-Type Natriuretic Peptides and Implications for Therapeutic Monitoring of Patients with Congestive Heart Failure. *Am. J. Cardiol.* **2003**, *92*, 628–631.

(168) Don-Wauchope, A. C.; McKelvie, R. S. Evidence Based Application of BNP/NT-ProBNP Testing in Heart Failure. *Clin. Biochem.* **2015**, *48*, 236–246.

(169) Sud, M.; Yu, B.; Wijeysundera, H. C.; Austin, P. C.; Ko, D. T.; Braga, J.; Cram, P.; Spertus, J. A.; Domanski, M.; Lee, D. S. Associations Between Short or Long Length of Stay and 30-Day Readmission and Mortality in Hospitalized Patients With Heart Failure. *JACC Hear. Fail.* **2017**, *5*, 578–588.

(170) Jourdain, P.; Jondeau, G.; Funck, F.; Gueffet, P.; Le Helloco, A.; Donal, E.; Aupetit, J. F.; Aumont, M. C.; Galinier, M.; Eicher, J. C.; *et al.* Plasma Brain Natriuretic Peptide-Guided Therapy to Improve Outcome in Heart Failure. The STARS-BNP Multicenter Study. *J. Am. Coll. Cardiol.* **2007**, *49*, 1733–1739.

(171) Mainville, C. A.; Clark, G. H.; Esty, K. J.; Foster, W. M.; Hanscom, J. L.; Hebert, K. J.; Lyons, H. R. Analytical Validation of an Immunoassay for the Quantification of N-Terminal pro–B-Type Natriuretic Peptide in Feline Blood. *J. Vet. Diagnostic Investig.* **2015**, *27*, 414–421.

(172) Song, K. S.; Nimse, S. B.; Sonawane, M. D.;

Warkad, S. D.; Kim, T. Ultra-Sensitive NT-ProBNP Quantification for Early Detection of Risk Factors Leading to Heart Failure. *Sensors* **2017**, *17*, 2116.

(173) Lee, G.-B.; Sinhamahapatra, A.; Gopinnathan, P.; Chung, Y.-D.; Shiesh, S.-C. Simultaneous Detection of Multiple NT-ProBNP Clinical Samples Utilizing an Aptamer-Based Sandwich Assay on an Integrated Microfluidic System. *Lab Chip* **2019**, *19*, 1676–1685.

(174) Sinha, A.; Gopinathan, P.; Chung, Y.-D.; Shiesh, S.-C.; Lee, G.-B. Simultaneous Detection of Multiple NT-ProBNP Clinical Samples Utilizing an Aptamer-Based Sandwich Assay on an Integrated Microfluidic System. *Lab Chip* **2019**, *19*, 1676–1685.

(175) Grubisha, D. S.; Lipert, R. J.; Park, H. Y.; Driskell, J.; Porter, M. D. Femtomolar Detection of Prostate-Specific Antigen: An Immunoassay Based on Surface-Enhanced Raman Scattering and Immunogold Labels. *Anal. Chem.* **2003**, *75*, 5936–5943.

(176) Mandl, A.; Filbrun, S. L.; Driskell, J. D. Asymmetrically Functionalized Antibody-Gold Nanoparticle Conjugates to Form Stable Antigen-Assembled Dimers. *Bioconjugate Chem.* **2017**, *28*, 38–42.

(177) Anfossi, L.; Di Nardo, F.; Russo, A.; Cavalera, S.; Giovannoli, C.; Spano, G.; Baumgartner, S.; Lauter, K.; Baggiani, C. Silver and Gold Nanoparticles as Multi-Chromatic Lateral Flow Assay Probes for the Detection of Food Allergens. *Anal. Bioanal. Chem.* **2019**, *411*, 1905–1913.

(178) Yeh, C. H.; Chen, W. T.; Lin, H. P.; Chang, T. C.; Lin, Y. C. Development of an Immunoassay Based on Impedance Measurements Utilizing an Antibody-Nanosilver Probe, Silver Enhancement, and Electro-Microchip. *Sensors Actuators, B Chem.* **2009**, *139*, 387–393.

(179) Siriwardana, K.; Wang, A.; Vangala, K.; Fitzkee, N.; Zhang, D. Probing the Effects of Cysteine Residues on Protein Adsorption onto Gold Nanoparticles Using Wild-Type and Mutated GB3 Proteins. *Langmuir* **2013**, *29*, 10990–10996.

(180) Pollok, N. E.; Rabin, C.; Smith, L.; Crooks, R. M. Orientation-Controlled Bioconjugation of Antibodies to Silver Nanoparticles. *Bioconjugate Chem.* **2019**, *30*, 3078–3086.

(181) Laboratories, B. LYNX Rapid Antibody Conjugation Kit Protocol, 2013, 2–3.

(182) Schellenberger, U.; O'Rear, J.; Guzzetta, A.; Jue, R. A.; Protter, A. A.; Stephen Pollitt, N. The Precursor to B-Type Natriuretic Peptide Is an O-Linked Glycoprotein. *Arch. Biochem. Biophys.* **2006**, *451*, 160–166.

(183) Røsjø, H.; Dahl, M. B.; Jørgensen, M.; Røysland, R.; Brynildsen, J.; Cataliotti, A.; Christensen, G.; Høiseth, A. D.; Hagve, T. A.; Omland, T. Influence of Glycosylation on Diagnostic and Prognostic Accuracy of N-Terminal pro-B-Type Natriuretic Peptide in Acute Dyspnea: Data from the Akershus Cardiac Examination 2 Study. *Clin. Chem.* **2015**, *61*, 1087–1097.

(184) Thermofisher. *Dynabeads MyOne Streptavidin T1 Protocol*; 2016.

(185) Esteban Fernández de Ávila, B.; Escamilla Gómez, V.; Campuzano, S.; Pedrero, M.; Pingarrón, J. M. Disposable Amperometric Magnetoimmunosensor for the Sensitive Detection of the Cardiac Biomarker Amino-Terminal pro-B-Type Natriuretic Peptide in Human Serum. *Anal. Chim. Acta* **2013**, *784*, 18–24.

(186) Matei, I.; Buta, C. M.; Turcu, I. M.; Culita, D.; Munteanu, C.; Ionita, G. Formation and Stabilization of

Gold Nanoparticles in Bovine Serum Albumin Solution. *Molecules* **2019**, *24*, 3395.

(187) Gebregeorgis, A.; Bhan, C.; Wilson, O.; Raghavan, D. Characterization of Silver/Bovine Serum Albumin (Ag/BSA) Nanoparticles Structure: Morphological, Compositional, and Interaction Studies. *J. Colloid Interface Sci.* **2013**, *389*, 31–41.

(188) Stankovich, M. T.; Bard, A. J. The Electrochemistry of Proteins and Related Substances Part III. Bovine Serum Albumin. *J. Electroanal. Chem.* **1978**, *86*, 189–199.

(189) Krebs, H. A. Chemical Composition of Blood Plasma and Serum. *Annu. Rev. Biochem.* **1950**, *19*, 409–430.

(190) Havel, R. J.; Eder, H. A.; Bragdon, J. H. The Distribution and Chemical Composition of Ultracentrifugally Separated Lipoproteins in Human Serum. *J. Clin. Invest.* **1955**, *34*, 1345–1353.

(191) Pollok, N. E.; Rabin, C.; Walgama, C. T.; Smith, L.; Richards, I.; Crooks, R. M. Electrochemical Detection of NT-ProBNP Using a Metalloimmunoassay on a Paper Electrode Platform. *ACS Sensors* **2020**, *5*, 853–860.

(192) Liu, C.; Leng, W.; Vikesland, P. J. Controlled

Evaluation of the Impacts of Surface Coatings on Silver Nanoparticle Dissolution Rates. *Environ. Sci. Technol.* **2018**, *52*, 2726–2734.

(193) Hernández-Santos, D.; González-García, M. B.; García, A. C. Metal-Nanoparticles Based Electroanalysis. *Electroanalysis* **2002**, *14*, 1225–1235.

(194) Laboratories, B. LYNX Rapid plus Biotin (Type 2) Antibody Conjugation Kit Protocol, 2011, 2–4.

(195) Raditya, A. N.; O'Hare, D. Review—Electrochemical Sensor Biofouling in Environmental Sensor Networks: Characterisation, Remediation and Lessons from Biomedical Devices. *J. Electrochem. Soc.* **2020**, *167*, 127503.

(196) Wisniewski, N.; Reichert, M. Methods for Reducing Biosensor Membrane Biofouling. *Colloids Surf. B* **2000**, *18*, 197–219.

(197) Das, J.; Kelley, S. O. Protein Detection Using Arrayed Microsensor Chips: Tuning Sensor Footprint to Achieve Ultrasensitive Readout of CA-125 in Serum and Whole Blood. *Anal. Chem.* **2011**, *83*, 1167–1172.

(198) Álvarez-Martos, I.; Møller, A.; Ferapontova, E. E. Dopamine Binding and Analysis in Undiluted Human

Serum and Blood by the RNA-Aptamer Electrode. *ACS Chem. Neurosci.* **2019**, *10*, 1706–1715.

(199) Nemr, C. R.; Smith, S. J.; Liu, W.; Mepham, A. H.; Mohamadi, R. M.; Labib, M.; Kelley, S. O. Nanoparticle-Mediated Capture and Electrochemical Detection of Methicillin-Resistant Staphylococcus Aureus. *Anal. Chem.* **2019**, *91*, 2847–2853.

(200) Rowe, A. A.; Chuh, K. N.; Lubin, A. A.; Miller, E. A.; Cook, B.; Hollis, D.; Plaxco, K. W. Electrochemical Biosensors Employing an Internal Electrode Attachment Site and Achieving Reversible, High Gain Detection of Specific Nucleic Acid Sequences. *Anal. Chem.* **2011**, *83*, 9462–9466.

(201) Ostermeyer, A. K.; Kostigen Mumuper, C.; Semprini, L.; Radniecki, T. Influence of Bovine Serum Albumin and Alginate on Silver Nanoparticle Dissolution and Toxicity to Nitrosomonas Europaea. *Environ. Sci. Technol.* **2013**, *47*, 14403–14410.

(202) Monga, A.; Pal, B. Morphological and Physicochemical Properties of Ag-Au Binary Nanocomposites Prepared Using Different Surfactant Capped Ag Nanoparticles. *RSC Adv.* **2015**, *5*, 39954–39963.

(203) Cai, H.; Zhu, N.; Jiang, Y.; He, P.; Fang, Y. Cu@Au Alloy Nanoparticle as Oligonucleotides Labels for Electrochemical Stripping Detection of DNA Hybridization. *Biosens. Bioelectron.* **2003**, *18*, 1311–1319.

(204) Oezaslan, M.; Hasché, F.; Strasser, P. PtCu 3 , PtCu and Pt 3 Cu Alloy Nanoparticle Electrocatalysts for Oxygen Reduction Reaction in Alkaline and Acidic Media . *J. Electrochem. Soc.* **2012**, *159*, B444–B454.

(205) Peretyazhko, T. S.; Zhang, Q.; Colvin, V. L. Size-Controlled Dissolution of Silver Nanoparticles at Neutral and Acidic PH Conditions: Kinetics and Size Changes. *Environ. Sci. Technol.* **2014**, *48*, 11954–11961.

(206) Hasan, S. A Review on Nanoparticles : Their Synthesis and Types. *Res. J. Recent Sci.* **2014**, *4*, 1–3.

(207) Ma, D.; Hugener, T. A.; Siegel, R. W.; Christerson, A.; Mårtensson, E.; Önneby, C.; Schadler, L. S. Influence of Nanoparticle Surface Modification on the Electrical Behaviour of Polyethylene Nanocomposites. *Nanotechnology* **2005**, *16*, 724–731.

(208) Hong, R.; Pan, T.; Qian, J.; Li, H. Synthesis and Surface Modification of ZnO Nanoparticles. *Chem. Eng.*

J. **2006**, *119*, 71–81.

(209) Bagwe, R. P.; Hilliard, L. R.; Tan, W. Surface Modification of Silica Nanoparticles to Reduce Aggregation and Nonspecific Binding. *Langmuir* **2006**, *22*, 4357–4362.

(210) Qin, X.; Liu, L.; Xu, A.; Wang, L.; Tan, Y.; Chen, C.; Xie, Q. Ultrasensitive Immunoassay of Proteins Based on Gold Label/Silver Staining, Galvanic Replacement Reaction Enlargement, and in Situ Microliter-Droplet Anodic Stripping Voltammetry. *J. Phys. Chem. C* **2016**, *120*, 2855–2865.

(211) Katz, E.; Willner, I.; Wang, J. Electroanalytical and Bioelectroanalytical Systems Based on Metal and Semiconductor Nanoparticles. *Electroanalysis* **2004**, *16*, 19–44.

(212) Hwang, P.; Guyda, H.; Friesen, H. A Radioimmunoassay for Human Prolactin. *Proc. Natl. Acad. Sci. U. S. A.* **1971**, *68*, 1902–1906.

(213) Kim, D.; Daniel, W. L.; Mirkin, C. A. Microarray-Based Multiplexed Scanometric Immunoassay for Protein Cancer Markers Using Gold Nanoparticle Probes. *Anal. Chem.* **2009**, *81*, 9183–9187.

(214) Liu, X.; Dai, Q.; Austin, L.; Coutts, J.; Knowles, G.; Zou, J.; Chen, H.; Huo, Q. A One-Step Homogeneous Immunoassay for Cancer Biomarker Detection Using Gold Nanoparticle Probes Coupled with Dynamic Light Scattering. *J. Am. Chem. Soc.* **2008**, *130*, 2780–2782.

(215) Hainfeld, J. E.; Furuya, F. R. A 1.4-Nm Gold Cluster Covalently Attached to Antibodies Improves Immunolabeling. *J. Histochem. Cytochem.* **1992**, *40*, 177–184.

(216) Cheng, L.; Zhu, G.; Liu, G.; Zhu, L. FDTD Simulation of the Optical Properties for Gold Nanoparticles. *Mater. Res. Express* **2020**, *7*, 125009.

(217) Simon, J.; Udayan, S.; Bindiya, E. S.; Bhat, S. G.; Nampoori, V. P. N.; Kailasnath, M. Optical Characterization and Tunable Antibacterial Properties of Gold Nanoparticles with Common Proteins. *Anal. Biochem.* **2021**, *612*, 113975.

(218) Boisselier, E.; Astruc, D. Gold Nanoparticles in Nanomedicine: Preparations, Imaging, Diagnostics, Therapies and Toxicity. *Chem. Soc. Rev.* **2009**, *38*, 1759–1782.

(219) González, E.; Arbiol, J.; Puntes, V. F. Carving at the Nanoscale : Sequential Galvanic Ecxchange and Kirkendall Growth at Room Temperautre. *Science (80-.).* **2014**, *1377*, 1377–1381.

(220) Wiley, B.; Sun, Y.; Chen, J.; Cang, H.; Li, Z. Y.; Li, X.; Xia, Y. Shape-Controlled Synthesis of Silver and Gold Nanostructures. *MRS Bull.* **2005**, *30*, 356–361.

(221) Peng, Y.; Rabin, C.; Walgama, C. T.; Pollok, N. E.; Smith, L.; Richards, I.; Crooks, R. M. Silver Nanocubes as Electrochemical Labels for Bioassays. *ACS Sensors* **2021**, *6*, 1111–1119.

(222) Tetin, S. Y.; Ruan, Q.; Saldana, S. C.; Pope, M. R.; Chen, Y.; Wu, H.; Pinkus, M. S.; Jiang, J.; Richardson, P. L. Interactions of Two Monoclonal Antibodies with BNP: High Resolution Epitope Mapping Using Fluorescence Correlation Spectroscopy. *Biochemistry* **2006**, *45*, 14155–14165.

(223) Sun, Y.; Mayers, B. T.; Xia, Y. Template-Engaged Replacement Reaction: A One-Step Approach to the Large-Scale Synthesis of Metal Nanostructures with Hollow Interiors. *Nano Lett.* **2002**, *2*, 481–485.

(224) Zhang, Q.; Li, W.; Wen, L. P.; Chen, J.; Xia, Y. Facile Synthesis of Ag Nanocubes of 30 to 70 Nm in Edge Length with CF 3COOAg as a Precursor. *Chem. – A Eur. J.* **2010**, *16*, 10234–10239.